NUMERICAL ANALYSIS OF LASER POWDER BED FUSED STENTS MADE OF 316L STAINLESS STEEL CONSIDERING PROCESS-RELATED GEOMETRIC IRREGULARITIES.

[„Numerische Analyse von lasergeschmolzenen Stents aus Edelstahl 316L unter Berücksichtigung prozessbedingter geometrischer Unregelmäßigkeiten“]

Dissertation
zur Erlangung des Doktorgrades
der Humanwissenschaften
(Dr. sc. hum.)

der Fakultät für Medizin
der Universität Regensburg
und
der Fakultät Maschinenbau
der Ostbayerischen Technischen Hochschule (OTH) Regensburg

vorgelegt von
Lisa Wiesent
aus Neustadt a.d. Waldaab

im Jahr
2022

NUMERICAL ANALYSIS OF LASER POWDER BED FUSED STENTS MADE OF 316L STAINLESS STEEL CONSIDERING PROCESS-RELATED GEOMETRIC IRREGULARITIES.

[„Numerische Analyse von lasergeschmolzenen Stents aus Edelstahl 316L unter Berücksichtigung prozessbedingter geometrischer Unregelmäßigkeiten “]

Dissertation
zur Erlangung des Doktorgrades
der Humanwissenschaften
(Dr. sc. hum.)

der Fakultät für Medizin
der Universität Regensburg
und
der Fakultät Maschinenbau
der Ostbayerischen Technischen Hochschule (OTH) Regensburg

vorgelegt von
Lisa Wiesent
aus Neustadt a.d. Waldnaab

im Jahr
2022

Betreuerin:	*Prof. Dr.-Ing. Aida Nonn*	OTH Regensburg, Fakultät Maschinenbau
1. Mentor:	*Prof. Dr. med. Christof Schmid*	Universität Regensburg, Fakultät Medizin
2. Mentorin:	*Prof. Dr. rer. nat. Karla Lehle*	Universität Regensburg, Fakultät Medizin

Tag der mündlichen Prüfung:

Preface

This doctoral thesis summarizes my research as a member of the Computational Mechanics and Materials Lab (CMMLab) at the Faculty of Mechanical Engineering of Ostbayerische Technische Hochschule (OTH) Regensburg. Parts of this doctoral thesis have been published in the following peer-reviewed research papers:

- **Chapter 4: Wiesent L**, Schultheiß U, Schmid C, Schratzenstaller T, Nonn A. Experimentally validated simulation of coronary stents considering different dogboning ratios and asymmetric stent positioning. PLoS ONE. 2019;14(10):1–25. 0224026.
- **Chapter 5: Wiesent L**, Schultheiß U, Lulla P, Nonn A, Noster U. Mechanical properties of small structures built by selective laser melting stainless steel AISI 316L (316L) stainless steel– a phenomenological approach to improve component design. Materialwissenschaft und Werkstofftechnik. 2020;51(12):1615–1629.
- **Chapter 6**: **Wiesent L**, Schultheiß U, Lulla P, Noster U, Schratzenstaller T, Schmid C, et al. Computational analysis of the effects of geometric irregularities and post-processing steps on the mechanical behavior of additively manufactured 316L stainless steel stents. PLOS ONE. 2020 dec;15(12):e0244463.

Moreover, the publication mentioned below, which is a follow-up study based on the results of this doctoral thesis, has also been published as a peer-reviewed research paper.

- **Wiesent L**, Spear A., Nonn A. Computational analysis of the effects of geometric irregularities on the interaction of an additively manufactured 316L stainless steel stent and a coronary artery. Journal of mechanical behavior of biomedical materials. J Mech Behav Biomed Mater. 2022 Jan;125:104878.

Lisa Wiesent
Regensburg, October 19, 2022

Kurzfassung

Die Wiederverengung eines Koronargefäßes nach Stentimplantation, die sogenannte In-stent-Restenose (ISR), stellt ein vorherrschendes Problem der Behandlung der Arteriosklerose dar. ISR wird u.a. durch Gefäßwandverletzungen während der Stentimplantation, durch Fehlplatzierung, Über- oder Unterdimensionierung des Stents sowie eine damit verbundene ungünstige Veränderung des natürlichen Blutflusses verursacht. Fortschritte in der additiven Fertigung (AM) von Metallen, insbesondere in der Laser Powder Bed Fusion (L-PBF), ermöglichen die Herstellung von filigranen Gitterstrukturen im Mikrometerbereich und damit potenziell auch von Koronarstents. Indem sie neue oder sogar patientenspezifische Stentdesigns ermöglichen, könnten L-PBF Stents die Konformität des implantierten Stents mit der Gefäßwand verbessern und so möglicherweise die ISR-Raten in Zukunft reduzieren.

Die Forschung auf dem Gebiet der L-PBF-Stents befindet sich noch im Anfangsstadium. Der Schwerpunkt bisheriger Studien liegt hauptsächlich auf der Analyse der Anforderungen an das Stentdesign und der grundlegenden Funktionalität von L-BF-Stents. Untersuchungen zur Bestimmung des spezifischen mechanischen Verhaltens der L-PBF Stents, aber auch zu deren numerischen Analysen fehlen bis dato. Aufgrund der vergleichbaren Topologie stellen L-PBF Stents prinzipiell Gitterstrukturen mit einer geringen strukturellen Dichte dar. Daher ist es naheliegend, Erkenntnisse auf dem Gebiet der L-PBF Gitterstrukturen auf L-PBF-Stents zu übertragen. L-PBF Gitterstrukturen sind von prozessbedingten geometrischen Unregelmäßigkeiten betroffen sind, die sowohl deren Morphologie als auch deren mechanischen Eigenschaften (negativ) beeinflussen. Für eine genaue (numerische) Bewertung von L-PBF Stents müssen, analog zu L-PBF Gitterstrukturen, zunächst deren mechanischen Eigenschaften bestimmt und der Einfluss von prozessbedingten geometrischen Irregularitäten analysiert bzw. in den numerischen Modellen berücksichtigt werden. Weiterhin können, die mechanischen und morphologischen Eigenschaften von filigranen L-PBF Stents durch Nachbearbeitungsschritte (Oberflächen-, Wärmebehandlung) beeinflusst werden. Derzeit werden L-PBF Gitterstrukturen jedoch hauptsächlich im Bauzustand untersucht.

Ziel dieser Dissertation ist es, die Auswirkungen von prozessbedingten Unregelmäßigkeiten und unterschiedlichen Nachtbearbeitungsschritten auf das mechanische Verhalten von L-PBF 316L Stents zu bestimmen sowie eine numerische Methodik für deren Bewertung zu entwickeln.

Im ersten Schritt wurden Finite Elemente Analysen (FEA) zur Vorhersage der Verformung und des Spannungszustands von konventionell hergestellten Stents während des Crimpens und der Expansion entwickelt und anhand umfangreicher experimenteller Daten validiert. Diese FEAs ermöglichten eine genaue Vorhersage des Expansionsverhaltens von zwei verschiedenen Stentdesigns mit unterschiedlichem Expansionsverhalten sowie unterschiedlicher Positionierung auf dem Ballonkatheter.

Im zweiten Schritt wurde das mechanische Verhalten von L-PBF 316L anhand einachsiger Zugversuche an Standard-Flachzugproben mit variabler Probendicke und Ausrichtungswinkel bestimmt. Für jede Probenkonfiguration wurden Proben im Bauzustand als auch nach Wärmebehandlung berücksichtigt. Im Bauzustand wurde neben den bereits aus der Literatur bekannten anisotropen mechanischen Eigenschaften von L-PBF 316L ein signifikanter Anstieg der Festigkeit mit zunehmender Probendicke beobachtet, der bei einer Probendicke von etwa t >1.5 mm stagnierte und somit einen Sättigungswert erreichte. Die durchgeführte Wärmebehandlung führte zu einer Homogenisierung und zu keiner Rekristallisation des Gefüges. So wurden die Meltpoolgrenzen und Substrukturen aufgelöst und die Eigenspannungen abgebaut, während die länglichen und orientierten Körner und damit die anisotrope Mikrostruktur erhalten blieben. Dementsprechend wiesen die L-PBF 316L Zugproben auch nach der Wärmebehandlung probendicken und -richtungsabhängigen mechanischen Eigenschaften auf. Für eine zuverlässige strukturmechanische Bewertung von L-PBF-Bauteilen müssen daher deren mechanische Eigenschaften anhand von Prüfkörpern ermittelt werden, die in Größe, Ausrichtungswinkel und Nachbehandlungszustand mit dem späteren L-PBF-Bauteil vergleichbar sind.

Im letzten Schritt wurde eine Methode zur Bestimmung der mechanischen Eigenschaften von L-PBF-Stents entwickelt und das Expansionsverhalten von L-PBF-Stents unter Berücksichtigung prozessbedingter geometrischer Unregelmäßigkeiten in verschiedenen Nachbearbeitungszuständen mittels FEA bewertet. Die Herstellung von L-PBF Miniatur-Zugproben mit vergleichbarem Querschnitt wie Stentstreben sowie deren experimentelle Prüfung ist schwer zu realisieren und zudem sehr fehleranfällig. Daher wurde ein kombinierter experimentell-numerischer Ansatz für die inverse Bestimmung der mechanischen Eigenschaften von L-PBF 316L Stents entwickelt, welcher auf der exerimentellen Durchführung und FEA der uniaxialen Kompression von L-PBF Stents basierte. Die Stentmodelle innerhalb der FEA wurden aus Computertomographie (CT) Scans realer L-PBF Stents rekonstruiert. Auf diese Weise wurden die prozessbedingten geometrischen Irregularitäten detailliert abgebildet, wodurch die Vorhersage der Struktur-Eigenschafts-Beziehung ermöglicht wurde. So konnte erstmals das makroskopische mechanische Verhalten von L-PBF 316L Stents ermittelt und anschließend numerisch in einem Materialmodell abgebildet werden. Die morphologische Analyse der L-PBF Stents zeigte deutliche Abweichungen zwischen den tatsächlichen L-PBF Stents und dessen CAD-Modell auf (z.B., Oberflächenrauigkeit, Strebenwelligkeit, vergrößerte und inhomogene Strebendurchmesser, innere Defekte).

Die numerische Expansionsanalyse der L-PBF-Stentmodelle zeigte, dass L-PBF-Stents erst nach einer Oberflächen- und Wärmebehandlung ein vergleichbares Expansionsverhalten wie konventionell hergestellte Stents aufweisen. Die Analyse der Verformungs- und Spannungszustände zeigte, dass die L-PBF Stent sowohl im Bauzustand als auch nach einer Oberflächen- und Wärmebehandlung z.T. kritische lokale Spannungs-/Dehnungskonzentrationen aufweisen, insbesondere in den Bereichen mit ausgeprägten geometrischen Unregelmäßigkeiten.

Verbesserungen des L-PBF Verfahrens, der Nachbearbeitungsschritte und des Stentdesigns sind daher unerlässlich, um prozessbedingte geometrische Unregelmäßigkeiten und deren festigkeitsmindernde Auswirkungen zu minimieren und somit die strukturelle Sicherheit von L-PBF Stents zu gewährleisten. Ein möglicher Verbesserungsansatz ist die Herstellung der Stents auf speziellen μ-L-PBF Anlagen, die explizit für die Herstellung von filigranen Strukturen optimiert wurden. Auf diese Weise könnte bereits im Bauzustand eine höhere geometrische Genauigkeit und eine geringe Oberflächenrauigkeit erreicht und die anschließend notwendige Oberflächenbehandlung auf ein Minimum reduziert werden. Darüber hinaus sind Studien zur Ermüdungsfestigkeit, zum Schädigungsverhalten, zur Interaktion des Stents mit dem Blutgefäß und zur Analyse der Biokompatibilität von L-PBF 316L Stents unerlässlich. Um numerische Modelle effektiv für die Entwicklung von L-PBF Stents zu nutzen, sollte auch das Potenzial synthetischer L-PBF Stentmodelle untersucht werden, um die numerische Bewertung neuer Stent-Designs vor ihrer tatsächlichen Herstellung zu ermöglichen. Die synthetischen Stentmodelle stellen eine statistikbasierte Modifikation des ursprünglichen Stent-CAD-Modells dar (z.B. lokale Variationen des Strebenquerschnitts entlang der Strebenlänge). Auf diese Weise könnten die Auswirkungen von L-PBF bedingten geometrischen Unregelmäßigkeiten statistisch, und somit ohne explizite Rekonstruktion aus CT-Scans abgebildet werden.

Die Entwicklung von L-PBF Stents ist ein sehr komplexes interdisziplinäres Vorhaben in den Bereichen Fertigungstechnologie, Materialwissenschaft, Designentwicklung und numerischer Simulation. Um L-PBF als zuverlässige Alternative zur konventionellen Stentherstellung zu etablieren, ist weitere Forschung in diesen Bereichen unerlässlich. Durch die Bereitstellung einer Methode zur Bestimmung der mechanischen Eigenschaften von L-PBF Stents sowie deren numerische Analyse trägt diese Dissertation zur Weiterentwicklung von L-PBF 316L Stents bei und definiert notwendige Forschungsaspekte für zukünftige Arbeiten.

Abstract

Re-narrowing of a coronary vessel after stent implantation, known as in-stent restenosis (ISR), is a predominant problem in the treatment of atherosclerosis. ISR is caused, e.g., by vessel wall injury during stent implantation, malpositioning, over- or undersizing of the stent, and associated adverse alteration of natural blood flow. Advances in metal additive manufacturing, particularly in laser powder bed fusion (L-PBF), are enabling the generation of micro-scale L-PBF lattice structures and thus potentially coronary stents. By enabling new or even patient-specific stent designs, L-PBF stents could improve the conformity of the implanted stent and the vessel wall, thus potentially reducing ISR rates in the future.

Research in the field of L-PBF stents is still in its early stages. Previous studies have mainly focused on the analysis of stent design requirements and basic functionality of L-BF stents. Studies regarding the determination of the specific mechanical behavior of L-PBF stents but also regarding their numerical analysis are currently not available. Due to their similar topology, L-PBF stents resemble L-PBF lattice structures with a low structural density. Therefore, it is reasonable to transfer the findings in the field of L-PBF lattice structures to L-PBF stents. L-PBF lattice structures exhibit process-related geometric irregularities that (negatively) affect their morphology and their mechanical behavior. Therefore, for an accurate (numerical) evaluation of L-PBF lattice structures and thus of L-PBF stents, their mechanical behavior must be determined first, and the influence of the process-related geometric irregularities must be analyzed or considered within the numerical models. Furthermore, the mechanical and morphological behavior of filigree L-PBF stents can be altered by post-processing steps (surface, heat treatment). However, studies on L-PBF lattice structures are mainly limited to as-built structures.

Therefore, the aim of this doctoral thesis is to determine the effects of L-PBF process-related geometric irregularities and different post-processing conditions on the mechanical behavior of L-PBF 316L stents, as well as to develop a numerical methodology for their numerical evaluation.

In a first step, a finite element analysis (FEA) for the prediction of stent deformation during crimping and expansion was developed and validated using extensive experimental data from conventionally manufactured stents. These models accurately predicted the expansion behavior

of two different stent designs with different expansion behavior, as well as different positioning of the stent on the balloon catheter.

In the second step, the mechanical behavior of L-PBF 316L was determined using uniaxial tensile tests on standard flat tensile specimens with variable specimen thickness and orientation angle. For each specimen configuration, as-built and heat treated specimens were considered. In the as-built condition, besides the anisotropic mechanical properties of L-PBF 316L already known from the literature, a significant increase in strength with increasing specimen thickness was observed, which stagnated at a specimen thickness of t = 1.5 mm, thus reaching a saturation value. Heat treatment resulted in homogenization but no recrystallization of the microstructure. Thus, the melt pool boundaries and substructures were dissolved, and residual stresses were reduced, whereas the elongated and oriented grains and thus the anisotropic microstructure were preserved. Accordingly, the specimen thickness- and direction-dependent mechanical properties of L-PBF 316L were still observed after heat treatment. Thus, for a reliable structural mechanical evaluation of L-PBF parts, their mechanical properties must be determined using test specimens that are comparable in size, orientation angle, and post-treatment condition to the later L-PBF part.

In a final step, the mechanical behavior of L-PBF stents was determined and the expansion behavior of L-PBF stents under different post-processing conditions was evaluated by FEAs. The generation of L-PBF miniature tensile specimens of comparable cross section to stent struts and their experimental evaluation is challenging and highly error-prone. Therefore, a combined experimental-numerical approach was developed for the inverse determination of the mechanical behavior of L-PBF 316L stents based on experimental testing and FEA of uniaxial compression of L-PBF stents. The stent models were reconstructed from computed tomography (CT) scans of real L-PBF stents. In this way, process-related geometric irregularities were depicted enabling an accurate prediction of the stent structure-property relationship. Thus, the macroscopic mechanical behavior of L-PBF 316L stents could be determined for the first time and subsequently described numerically by a material model. Morphological analysis of the L-PBF stents further revealed significant discrepancies between the actual L-PBF stents and its computed aided design (CAD) model due to process-related geometric irregularities (surface roughness, strut waviness, enlarged and inhomogeneous strut diameters, internal defects). Numerical expansion analysis of the L-PBF stent models showed that L-PBF stents can exhibit comparable expansion behavior to conventional stents only after surface and heat treatment. However, subsequent analysis of deformation and stress states showed that L-PBF stents, both in the as-built condition and after surface and heat treatment, may exhibit critical local stress/strain concentrations, especially in the areas of pronounced geometric irregularities.

Improvements in the L-PBF process, post-processing steps, and stent design are therefore essential to minimize process-related geometric irregularities and thus their strength-reducing

effects, ultimately ensuring the structural safety of L-PBF stents. One possible improvement approach is to manufacture the stents on special μ-L-PBF systems that have explicitly been optimized to produce filigree structures. In this way, a higher geometric accuracy and low surface roughness could already be achieved in the as-built condition of L-PBF stents, and the subsequent required surface treatment could be reduced to a minimum. Furthermore, the fatigue strength, the damage behavior, the interaction of the stent with the blood vessel as well as the biocompatibility of L-PBF 316L stents should be investigated. To effectively use numerical models for the development of L-PBF stents, the potential of synthetic L-PBF stent models should also be investigated. The synthetic stent models represent a statistics-based modification of the original stent CAD model (e.g., local variations of strut cross section along strut length). In this way, the effects of L-PBF process-related geometric irregularities could be represented statistically and thus without explicit reconstruction from CT scans.

The development of L-PBF stents is a very complex interdisciplinary task in the fields of manufacturing technology, material science, design development and numerical simulation. To establish L-PBF as a reliable alternative to conventional stent fabrication, further research in this area is essential. By providing a method to determine the mechanical properties of L-PBF stents as well as their numerical analysis, this doctoral thesis could contribute to the further development of L-PBF 316L stents, as well as define necessary research aspects for further work.

Glossary

List of Abbreviations

2D	two-dimensional
316L	stainless steel AISI 316L
3D	three-dimensional
AB	as-built
AM	additive manufacturing, additively manufactured
BD	build direction
BMS	bare metal stent
CAD	computer aided design
CFD	computational fluid dynamics
CNC	computer numerically controlled
CoCr	cobalt-chrome alloy L605
CP	crystal plasticity
CT	computed tomography
DB	dogboning
DES	drug eluting stent
EBSD	electron backscatter diffraction
EP-HT	electropolished and heat treated
FE	finite element
FEA	finite element analysis
FEM	finite element method
FeMnCS	Fe–30Mn–1C–0.02S alloy

FSI	fluid-structure interaction
HT	heat treated
ISR	in-stent restenosis
L-PBF	laser powder bed fusion, laser powder bed fused
OTH	Ostbayerische Technische Hochschule
PCI	percutaneous coronary intervention
RVE	representative volume element
SEM	scanning electron microscopy
SLM	selective laser melting, selectively laser melted
Ti-6Al-4V	titan alloy
Yb	Ytterbium

Arabic Symbols

A_0	initial cross section
A	crosssection
C_{ijkl}	tensor of elastic moduli
D	diameter
d	distance
c_p	heat capacity at constant pressure
E	Young's modulus, energy density
E_I	internal energy
E_{KE}	kinetic energy
F	force
f_y	yield function
G	shear modulus
g	plastic flow potential
h	hatch spacing

I	electric current, intensity
I	invariant
o	outer
J_2	second invariant of the deviatoric stress tensor
k	slimness ratio, i.e. ratio between initial gauge length and specimen cross section area
K	hardening coefficient, material constant
l	length
l_0	initial length, gauge length
n	hardening exponent
P	power
p	pressure
R	radius
R_a	arithmetic average roughness
R_m	tensile strength
$R_{p0.2}$	yield strength
S	section modulus
u_r	radial displacement
T	temperature
t	time, thickness
u	displacement
u_{rot}	rotating boundary condition
u_{trans}	translational boundary condition
v	velocity, deformation rate
V	voltage
W	strain energy function
w	width

Greek Symbols

α	angle
Δ	difference/increment
δ_{ij}	Kronecker delta
$\sigma_{e,Hill}$	Hill stress
ε	strain
ε^{el}	elastic strain
ε_f	elongation at break
ε^{pl}	plastic strain

$\bar{\varepsilon}^{pl}$	equivalent plastic strain
$d\varepsilon_{ij}^{pl}$	plastic strain
$\dot{\bar{\varepsilon}}^{pl}$	plastic strain rate
ε_t	true strain
ε_u	uniform elongation
γ	shear, angular displacement of a material point
λ	adsorptivity
μ	coefficients of friction
ν	Poisson's ratio
ρ	density
s_{ij}	deviatoric stress tensor
σ	stress
σ_e	equivalent stress
σ_h	hydrostatic stress
σ_t	true stress
$\sigma_{e,vM}$	von Mises stress
σ_{ij}	stress tensor
σ_{UTS}	ultimate tensile strength
σ_y	yield stress
τ	shear stress
Θ	shear stress

Contents

1 Introduction

1.1 Coronary heart disease and current challenges of stenting

Chronic ischemic heart disease, also known as coronary artery disease, is the most common cause of death in Germany (2018: 76 273 deaths) [1]. Coronary artery disease is characterized by the narrowing (stenosis) or occlusion of the coronary arteries due to fat and calcium deposits, the so-called plaques. Coronary arteries provide the heart with oxygen and nutrients enriched blood. Since the coronary arteries are terminal arteries, the stenosis of these arteries leads to a local undersupply or destruction of a section of the heart muscle (heart attack). In about one third of cases, coronary artery disease is treated with percutaneous coronary intervention (PCI) in combination with the implantation of a stent, a filigree cylindrical, metallic lattice structures [2]. During PCI, a stent crimped onto a balloon catheter is inserted minimally invasively through a small incision in the arm/ groin to the narrowed coronary artery (figure 1.1a). Thereupon, the balloon is inflated to expand the stent and to restore the vascular lumen (figure 1.1b). The balloon catheter is then removed, leaving the stent permanently in the vessel to keep it open (figure 1.1c).

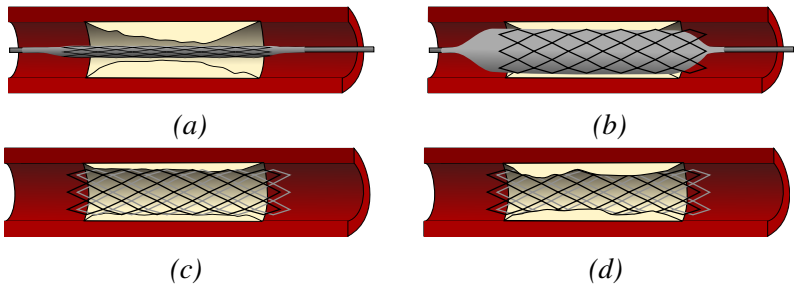

Figure 1.1: Schematic illustration of the stenting procedure and the occurrence of in-stent restenosis. (a) Stent crimped onto a balloon catheter within a stenosed artery. (b) Stent expansion by inflating the balloon, thus compressing the plaque, and restoring the arterial lumen. (c) Restored lumen after stent implantation. (d) Recurrence of stenosis at the stented artery (in-stent restenosis).

The re-narrowing of the artery after PCI and stenting (figure 1.1d), the so-called in-stent restenosis (ISR), remains a predominant clinical problem [3]. ISR is attributed to an acute inflammatory reaction of the arterial wall with subsequent neointimal hyperplasia due to arterial damage

during PCI, insufficient stent-artery compliance, or unfavorable changes in hemodynamics after PCI [3–9]. Arterial damage is partly related to the transient, commonly concave expansion characteristics of the balloon-stent system, referred to as the dogboning (DB) ratio (figure 1.2, 1.3a). Thereby, stent expansion is initially pronounced at the stent ends, causing local arterial damage due to the rapid outward movement of the stent struts and or due to longitudinal stretching of the artery as stent expansion proceeds. Mathematically, the DB ratio is expressed as

$$DB = \frac{D_{end} - D_{central}}{D_{end}} \tag{1.1}$$

with D_{end} being the stent diameter at the proximal/ distal stent end and $D_{central}$ the stent diameter at the central stent part during stent deployment (figure 1.2). Of most interest is the maximum DB ratio during stent expansion, i.e. the greatest deviation between the diameter of the stent ends and the stent center.

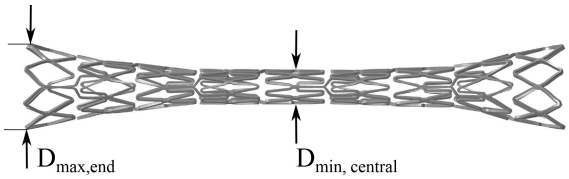

Figure 1.2: Schematic illustration of the dogboning ratio, adapted from Wiesent et al. [10].

Besides the stent expansion characteristics, the expanded stent diameter (i.e. stent over-/undersizing), stent length, number of stents, overlap of multiple stents and morphology/ curvature of the artery were identified as predictive factors for ISR as these either cause high mechanical stresses/injuries at the vessel wall and/ or unfavorable alter the natural hemodynamics [6, 8, 11–14]. Consequently, complex lesions, such as small, long, tapered, curved or branching arteries, pose a particular challenge for PCI and are associated with low clinical success [3] (figure 1.3).

The development of drug eluting stents (DESs) has reduced the ISR risk for uncomplicated lesions to less than 10 %[1] [3, 15, 16]. However, over the long term ($>$ 5 years), DESs and uncoated BMSs still exhibit comparable number of deaths and nonfatal spontaneous myocardial infarctions [17, 18]. This is attributed to the fact that DESs, like BMSs, have a residual risk of ISR due to mechanical stress on the vessel wall during stent implantation [19]. A further drawback of DESs is their lower cost-effectiveness compared with BMSs [19]. Therefore, to enhance the clinical outcome of PCI/stenting, studies have called for improvements in stent coatings as well as stent materials, stent designs, and implantation strategies to minimize the stent-induced arterial stresses and to preserve the natural hemodynamics within the arteries [4, 20, 21].

[1] ISR rate bare metal stents (BMSs): 16 - 32 %

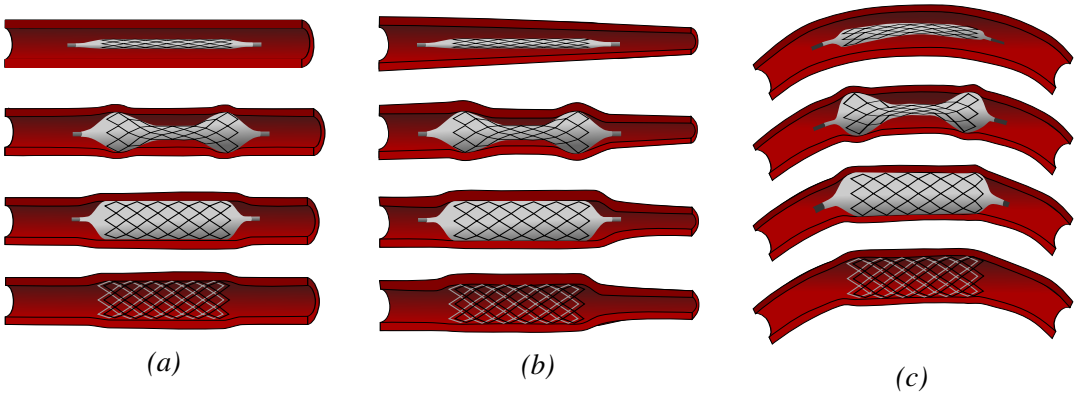

Figure 1.3: Predictors in-stent restenosis. (a) Stent expansion within a straight artery highlighting the pronounced dogboning ratio. (b) Stent expansion within a tapered artery highlighting local stent oversizing. (c) Stent expansion within a curved vessel highlighting the straightening effect.

1.2 Potential and challenges in the field of L-PBF stents

Customized stents could overcome some of the remaining challenges of ISR by improving the stent-artery conformity, thus reducing arterial damage and alterations in natural blood flow. Metallic coronary stents are commonly made of materials with high ductility, corrosion resistance and biocompatibility, such as 316L, cobalt-chrome alloy L605 (CoCr), tantalum, nitinol or titanium [22, 23]. Conventional balloon-expandable metallic stents are commonly laser cut from a metal tube. The basic shape is thus determined by the tube, making customized adjustment hardly possible.

In recent year, advances in additive manufacturing (AM), in particular in laser powder bed fusion (L-PBF), enable the production of metallic lattice structures in the micrometer range and thus, in principle, cardiovascular stents [24–27]. L-PBF, commonly also known as selective laser melting (SLM), is a powder bed-based AM process in which the part is built up layer-by-layer by local melting of raw material powder with a laser. Like all AM processes, L-PBF offers great potential regarding the ability to create complex near net-shape parts without the constraints of traditional manufacturing methods. Thus, the part design can be optimized or customized according to functional requirements, e.g., lightweight parts with increased stiffness or medical implants [28, 29]. In this way, the limitations of conventional stent manufacturing could be overcome and new designs, e.g., expansion-optimized, bifurcated, tapered, curved, or even customized stents based on angiographic data, could be realized.

L-PBF is currently a major focus of research for biomedical applications. Current challenges mainly relate to achieving the best possible geometric and dimensional tolerances, reducing surface waviness, creating filigree structures, achieving high densities, and reducing oxide impurities [30]. Since all these factors apply to L-PBF stents, it is obvious that there is a great

need for research in this area. Research in the field of L-PBF stents, is still at an early stage. So far, the main focus has been on the general manufacturability, post-processing and selective functionality of the L-PBF stents [26, 27, 31, 32]. In 2017, Demir et al. [26] succeeded in producing the first metallic stents via L-PBF of CoCr. In 2020, the principal functionality of L-PBF stents made of CoCr as well as of a novel biodegradable FeMnCS alloy was demonstrated by balloon expansion analysis [31, 32]. Although 316L is one of the most widely used materials for conventional stents [22, 23], in depth studies on L-PBF 316L stents are hardly available so far. Since the strut diameter of cardiovascular stents ($D_{strut} \approx 60$ - 150 μm) is comparable to the laser spot diameter of industrial L-PBF machines, the manufacturing of stents via L-PBF is very challenging [31]. Although previous studies have demonstrated the basic feasibility of L-PBF coronary stents, there are still some limitations, especially in terms of their mechanical evaluation [31, 32].

Due to the similar topology, knowledge gained in the field of L-PBF lattice structures can be transferred to L-PBF stents. Similar to L-PBF lattice structures, L-PBF stents exhibited geometric irregularities (e.g. strut waviness, pores, increased strut diameter) and deviations in the mechanical properties of the L-PBF stent material compared to its wrought material [25, 31, 33–37]. For L-PBF lattice structures, the deviations in mechanical properties, i.e. the decrease in mechanical properties compared to large-sized specimens, are due to the size effect and the associated changes in microstructure, process-related geometric irregularities, surface roughness and defects [25, 33]. In this context, the size effect refers to the change in mechanical properties with decreasing structure size, which occurs mainly at small structure sizes. Thus, with decreasing strut size, L-PBF process-related changes in microstructure, an increase in surface roughness and pores, and an increase in geometric irregularities/deviations from the intended geometry were observed, resulting in an overall decrease in the mechanical properties of small size L-PBF struts. Considering the general knowledge in the field of L-PBF metals, it is also expected that the mechanical properties of L-PBF stents can be modified by post-processing steps such as surface or heat treatment; e.g. an increase in ductility by adequate heat treatment, or the compensation of the process-related geometric irregularities by adequate surface treatment [31, 38–40]. In summary, L-PBF stents have the potential to overcome some remaining challenges of stenting and ISR. However, L-PBF process-related geometric irregularities and post-processing steps are expected to have an impact on the morphology, the mechanical behavior but also on the interaction of the L-PBF stent with the arterial wall during implantation. So far, in-depth investigations on the impact of L-PBF process-related irregularities on the mechanical behavior of stents are hardly available.

In a mere experimental framework, it is very difficult and time consuming to consider single effects in isolation, or to develop/ optimize stent designs according to the specific requirements of the L-PBF process. Computational methods can be used to extend the knowledge gained from

experimental data and to consider individual phenomena in isolation. Thus, within numerical models different 'what if?' scenarios considering various material states, geometries and loading conditions can be evaluated and virtually tested before the stents are manufactured. In recent years, numerical models have been established for the analysis and optimization of conventionally manufactured stents [4, 10, 20, 41–44]. However, to date, no numerical analyses of the mechanical behavior of L-PBF stents are available so far. Even though the use of topological optimization tools to improve the expansion behavior of L-PBF stents is recommended [31], no studies have been performed to investigate the transferability of numerical methods established for conventionally manufactured stents to L-PBF stents.

Combined experimental and numerical studies on L-PBF lattice structure indicate that process-related geometric irregularities have a distinct influence on the mechanical properties on filigree L-PBF structures, leading to differences between the numerical prediction based on the as-designed geometry and the experimentally determined mechanical response of the actual L-PBF structure [25, 34–37, 45]. In addition, due to the small structural size of L-PBF stents, the stents are further expected to be affected by the size effect causing further deviations between the material behavior of bulk material specimens and the stent material. Thus, conventional stent development/optimization approaches based on idealized models and bulk material properties are likely not suitable for L-PBF stents and will have to be adapted to consider the influence of process-related irregularities on the mechanical behavior of L-PBF stents.

1.3 Aim of this thesis

Considering the above overview, the aim of this doctoral thesis is to analyze the impact of process-related geometric irregularities, the size effect, and post-processing steps on the mechanical response of L-PBF 316L stents using a combined experimental and computational framework. Thus, a validated computational method for predicting the mechanical behavior of stents during implementation was developed first. Thereupon, the mechanical properties of L-PBF 316L tensile specimens with varying specimen thickness were determined in both the as-built and heat treated condition. Since the mechanical properties of standard tensile specimens were found to be hardly transferable to L-PBF stents, a combined numerical-experimental method was established to determine the mechanical behavior of L-PBF stents. Finally, a numerical method based on finite element analysis (FEA) was developed to predict the behavior of L-PBF stents during implementation that accounts for process-related geometric irregularities. The results and findings obtained in this work can serve as a basis for the development of methods to reliably characterize the mechanical properties and behavior of L-PBF stents, and thus for the development of new stent designs/optimization.

2 State of the art and literature review

In this chapter, the theoretical fundamentals as well a review of the relevant literature for the subsequent computational analysis of L-PBF stents is provided. In chapter 2.1, some fundamentals of continuum mechanics are provided, which form the basis for the later computational stent analysis. Since size effects are expected due to the small structural size of the stents, their various manifestations will be addressed in chapter 2.2. In this context, a brief overview of multiscale modeling of plasticity is also given. Even though the numerical analyses within this doctoral thesis are limited to continuum mechanics/macroscale approaches, this overview is intended to provide a better understanding for the later comprehensive discussion of this work. Chapter 2.3 provides a brief literature review of the L-PBF process and the associated geometric irregularities, microstructure, and mechanical properties of L-PBF 316L. Finally, an overview of the state of the art and the limitation of numerical stent analysis is provided in chapter 2.4.

2.1 Fundamentals of continuum mechanics

In this chapter, a characteristic stress-strain diagram for 316L and the associated determination of characteristic material parameters from uniaxial tensile tests are presented. Thereupon, some basics of continuum mechanics are described. For more details it is referred to Ref. [46].

2.1.1 Characteristic stress-strain diagrams of stainless steel 316L

The elastic-plastic deformation behavior of steels is commonly described by stress-strain curves derived from uniaxial tensile tests on round or flat tensile specimens. These are loaded at a constant deformation speed v while measuring the change in length Δl and the required force F. By normalizing with the initial specimen cross section A_0 and the initial measurement length l_0, the engineering stress σ and strain ε are obtained:

$$\sigma = \frac{F}{A_0} \tag{2.1}$$

$$\varepsilon = \frac{\Delta l}{l_0}. \tag{2.2}$$

Characteristic material parameters can be determined from the engineering stress-strain diagram. A stress-strain diagram representative of 316L with continuous yielding is shown in figure 2.1a. The linear elastic region, is characterized by Hook's law

$$\sigma = E \cdot \varepsilon \tag{2.3}$$

with the Young's modulus E. The transition between elastic and plastic behavior is characterized by the yield stress σ_y. For continuous yielding, this point is commonly approximated by the $R_{p0.2}$ value, which corresponds to the stress value at a plastic strain of ε = 0.002 after unloading. The maximum stress value within the engineering stress-strain curve is defined as the ultimate tensile strength σ_{UTS}, also known as R_m. The associated strain value is referred to as the uniform elongation value ε_u, which corresponds to the strain value at the ultimate tensile strength adjusted for the elastic component. The ultimate tensile stress σ_{UTS} further marks the transition point between strain hardening and the onset of necking. During necking, a significant reduction of the local cross section occurs, resulting in global softening despite increasing stress within the neck before the specimen finally breaks. The permanent deformation of the specimen up to fracture is described by the elongation at break ε_f.

Since the engineering stress-strain curve refers to the initial cross section A_0, it is not suitable to describe the local stress and strain states. Therefore, it is necessary to determine the true stress σ_t and the true strain ε_t from the engineering stress and strain:

$$\sigma_t = \frac{F}{A} = \sigma\,(1+\varepsilon)\,, \tag{2.4}$$

with the force F and the current current specimen cross section A.

$$\varepsilon_t = ln\frac{l+\Delta l}{l} = ln(1+\varepsilon), \tag{2.5}$$

with the change in length Δl and the current specimen length l.

The course of a typical engineering stress-strain curve with the corresponding true stress-strain curve is shown in figure 2.1b.

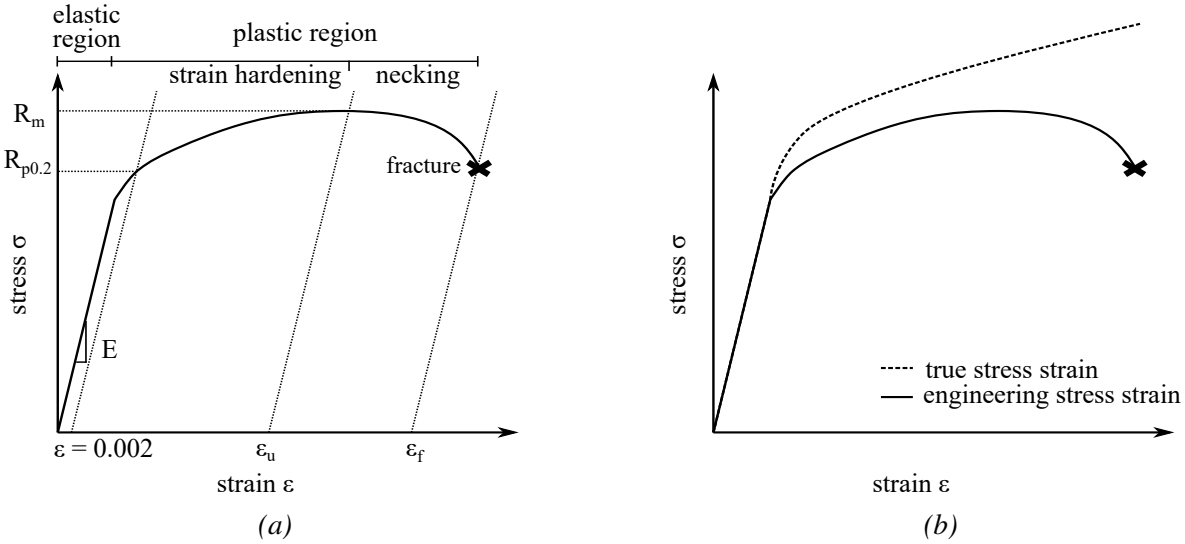

Figure 2.1: Stress-strain curves with continuous yielding. (a) Engineering stress-strain curve. (b) Comparison of the engineering stress-strain curve and true stress-strain curve.

2.1.2 Stress and strain tensor

Stress tensor

The load condition of an arbitrary material point can be described by the *Cauchy stress tensor* σ_{ij}

$$\sigma_{ij} = \begin{bmatrix} \sigma_{11} & \sigma_{12} & \sigma_{13} \\ \sigma_{21} & \sigma_{22} & \sigma_{23} \\ \sigma_{31} & \sigma_{32} & \sigma_{33} \end{bmatrix} = \begin{bmatrix} \sigma_{11} & \tau_{12} & \tau_{13} \\ \tau_{21} & \sigma_{22} & \tau_{23} \\ \tau_{31} & \tau_{32} & \sigma_{33} \end{bmatrix}, \tag{2.6}$$

with the normal stresses σ_{ii} and shear stress σ_{ii} or τ_{ij} (for $i \neq j$).

In classical continuum mechanics, it is further assumed that no momentum is transmitted at an infinitesimal material point, so the stress tensor is considered symmetric, with

$$\sigma_{ij} = \sigma_{ji} \tag{2.7}$$

thus, reducing the stress tensor to six independent components [46]. The distinct values of the stress tensor depend on the coordinate system. By determining the eigenvalues of the stress tensor, the stress tensor can be transformed into the principal stress system (equation 2.8). In the principal stress system, the shear stresses disappear and only the normal stress components, the so-called principal stresses $(\sigma_1, \sigma_2, \sigma_3)$, are present [46]:

$$\sigma_{ij} = \begin{bmatrix} \sigma_1 & 0 & 0 \\ 0 & \sigma_2 & 0 \\ 0 & 0 & \sigma_3 \end{bmatrix} \tag{2.8}$$

If the principal stresses are identical, a hydrostatic stress state ($\sigma_h = \sigma_1 = \sigma_2 = \sigma_3$) is present.

Besides the principal stresses, each stress tensor contains further invariant quantities, the so-called three basic invariants I of the stress tensor:

$$\begin{aligned} I_1 &= \sigma_{ii} \\ I_2 &= \frac{1}{2}(\sigma_{ii}\sigma_{jj} - \sigma_{ij}\sigma_{ji}) \\ I_3 &= det(\sigma_{ij}) \end{aligned} \tag{2.9}$$

Stress tensors are commonly divided into a hydrostatic stress tensor $\delta_{ij}\sigma_h$ and a deviatoric stress tensor s_{ij}:

$$s_{ij} = \sigma_{ij} - \delta_{ij}\sigma_h \tag{2.10}$$

with the Kronecker delta δ_{ij}. Using the first invariant of the stress tensor I_1 (equation 2.9), the hydrostatic stress σ_h is calculated as

$$\sigma_h = \frac{1}{3}I_1 = \frac{1}{3}(\sigma_{11} + \sigma_{22} + \sigma_{33}). \tag{2.11}$$

Strain tensor

Strain is defined as the relative displacement of an arbitrary material point within a deformed body. The strain condition of an arbitrary material point can be described by the strain tensor ε_{ij}:

$$\varepsilon_{ij} = \frac{1}{2}\left(\frac{\partial u_i}{\partial x_j} + \frac{\partial u_j}{\partial x_i}\right) = \begin{bmatrix} \varepsilon_{11} & \frac{1}{2}\gamma_{12} & \frac{1}{2}\gamma_{13} \\ \frac{1}{2}\gamma_{21} & \varepsilon_{22} & \frac{1}{2}\gamma_{23} \\ \frac{1}{2}\gamma_{31} & \frac{1}{2}\gamma_{32} & \varepsilon_{33} \end{bmatrix} = \begin{bmatrix} \varepsilon_{11} & \varepsilon_{12} & \varepsilon_{13} \\ \varepsilon_{21} & \varepsilon_{22} & \varepsilon_{23} \\ \varepsilon_{31} & \varepsilon_{32} & \varepsilon_{33} \end{bmatrix}. \tag{2.12}$$

The diagonal components of the strain tensor are the normal strains ε_{ii} describing the extensional strains along the respective coordinate axes. The off-diagonal components are half of the angular distortion/shear γ_{ij} (for $i \neq j$) of two deformed lines that were originally parallel to the axes indicated by the indices.

2.1.3 Models of linear elasticity

Linear elastic deformation is described by the general formulation of *Hook's law*:

$$\sigma_{ij} = C_{ijkl}\varepsilon_{kl}, \tag{2.13}$$

with the fourth-order stiffness tensor of elastic moduli C_{ijkl}. For an isotropic material, strain can be expressed using the generalized Hook's law as

$$\begin{aligned} \varepsilon_{11}^{el} &= \frac{1}{E}\left(\sigma_{11} - \nu\left(\sigma_{22}+\sigma_{33}\right)\right) \\ \varepsilon_{22}^{el} &= \frac{1}{E}\left(\sigma_{22} - \nu\left(\sigma_{11}+\sigma_{33}\right)\right) \\ \varepsilon_{33}^{el} &= \frac{1}{E}\left(\sigma_{33} - \nu\left(\sigma_{11}+\sigma_{22}\right)\right) \\ \varepsilon_{12}^{el} = \frac{1}{2G}\sigma_{12} \qquad \varepsilon_{13}^{el} &= \frac{1}{2G}\sigma_{13} \qquad\qquad \varepsilon_{23}^{el} = \frac{1}{2G}\sigma_{23}, \end{aligned} \tag{2.14}$$

with the Young's Modulus E, the Poisson ratio ν and the shear modulus $G = \frac{E}{2(1+\nu)}$ [46].

2.1.4 Models of plasticity

Plastic deformation of metals is caused by irreversible movement of atoms along a slip plane (dislocation) within a grain. This slip process is only initiated if a critical resolved shear stress τ_{crit} is exceeded, otherwise the deformation of the grain is elastic. For most perfect metallic materials, it was found that yielding is only induced by deviation from the hydrostatic stress state σ_h (equation 2.11) and thus only by the deviatoric stress tensor s_{ij} (equation 2.10) [46].

To describe the plastic deformation, the total deformation of a component is commonly composed into an elastic strain ε^{el} (i.e., reversible deformation after unloading) and the plastic strain part ε^{pl} (i.e., irreversible deformation after unloading). In incremental form, the strain state is given as

$$d\varepsilon_{ij} = d\varepsilon_{ij}^{e} + d\varepsilon_{ij}^{p}. \tag{2.15}$$

To describe the plastic deformation of metals, material models are commonly used containing a *yield criterion*, a *flow rule*, and a *hardening rule*.

Yield criterion

The yield criterion distinguishes whether a deformation state causes an elastic or plastic material response. Mathematically the yield criterion f_y is described as a function of an equivalent stress σ_e, which represents a multiaxial stress state, and the yield stress σ_y. The yield criterion states that plastic deformation occurs if the equivalent strength σ_e is equal to a defined yield stress σ_y, i.e., $f_y = 0$.

$$f_y(\sigma_{ij}) = \sigma_e(\sigma_{ij}) - \sigma_y = 0. \tag{2.16}$$

In three-dimensional (3D) space, this function spans a yield surface (figure 2.2a). If the stress state is within the yield surface ($f_y < 0$), the deformation is purely elastic. If, on the other hand, the stress state is on the yield surface ($f_y = 0$), plastic deformation initiates.

For ductile isotropic metals, the *von Mises* yield criterion $f_{y,vM}$ is commonly used which is based on the second invariant of the deviatoric stress tensor J_2:

$$f_{y,vM} = \sigma_{e,vM} - \sigma_y = 0 \quad \text{, with} \tag{2.17}$$

$$\begin{aligned} \sigma_{e,vM} &= \sqrt{3J_2} = \sqrt{\tfrac{2}{3} s_{ij} s_{ij}} \\ &= \sqrt{\tfrac{1}{2}\left[(\sigma_{11}-\sigma_{22})^2 + (\sigma_{22}-\sigma_{33})^2 + (\sigma_{33}-\sigma_{22})^2\right] + 3(\sigma_{12}^2 + \sigma_{23}^2 + \sigma_{31}^2)}. \end{aligned} \tag{2.18}$$

Due to their specific manufacturing processes, sheet materials as well as L-PBF materials exhibit different, i.e., anisotropic, deformation behavior depending on their loading directions. For ductile anisotropic metals, the *Hill'48* yield criterion $f_{y,Hill}$ (equation 2.19) is commonly used.

$$f_{y,Hill}(\sigma_{ij}) = \sigma_{e,Hill} - \sigma_y = 0 \quad \text{, with} \tag{2.19}$$

$$\sigma_{e,Hill} = \sqrt{F(\sigma_{22} - \sigma_{33})^2 + G(\sigma_{33} - \sigma_{11})^2 + H(\sigma_{11} - \sigma_{22})^2 + 2L\sigma_{23}^2 + 2M\sigma_{31}^2 + 2N\sigma_{12}^2} \tag{2.20}$$

The Hill'48 equivalent stress $\sigma_{e,Hill}$ represents an extension of the von Mises equivalent stress $\sigma_{e,vM}$ to consider plastic anisotropy along the three axis of the principal stress systems using six independent material constants F, G, H, L, M and N (equation 2.20). These material constants are obtained from material testing in different loading directions and calculated as

$$\begin{aligned} F &= \frac{1}{2}\left[-\frac{1}{R_{xx}^2} + \frac{1}{R_{yy}^2} + \frac{1}{R_{zz}^2}\right] & L &= \frac{3}{2}\frac{1}{R_{yz}^2} \\ G &= \frac{1}{2}\left[\frac{1}{R_{xx}^2} - \frac{1}{R_{yy}^2} + \frac{1}{R_{zz}^2}\right] & M &= \frac{3}{2}\frac{1}{R_{xz}^2} \\ H &= \frac{1}{2}\left[\frac{1}{R_{xx}^2} + \frac{1}{R_{yy}^2} - \frac{1}{R_{zz}^2}\right] & N &= \frac{3}{2}\frac{1}{R_{xy}^2} \end{aligned} \tag{2.21}$$

with the yield ratios R

$$R_{xx} = \frac{\sigma_{xx}^y}{\sigma_0}, \quad R_{yy} = \frac{\sigma_{yy}^y}{\sigma_0}, \quad R_{zz} = \frac{\sigma_{zz}^y}{\sigma_0}, \quad R_{xy} = \sqrt{3}\frac{\tau_{xy}^y}{\sigma_0}, \quad R_{yz} = \sqrt{3}\frac{\tau_{yz}^y}{\sigma_0}, \quad R_{xz} = \sqrt{3}\frac{\tau_{xz}^y}{\sigma_0} \tag{2.22}$$

that relate the yield stresses in different direction to a reference yield strength σ_0 [47]. If all yield ratios are equal to one, the Hill 48' equivalent stress is equal to the von Mises equivalent stress.

Flow rule

Once the yield criterion is met (i.e., $f_y = 0$), a flow rule is used to determine the plastic strain increment $d\varepsilon_{ij}^{pl}$ induced by the current stress state:

$$d\varepsilon_{ij}^{pl} = d\lambda \frac{\partial g(\sigma_{ij})}{\partial \sigma_{ij}}, \tag{2.23}$$

with $d\lambda > 0$ being a hardening parameter and $g(\sigma_{ij})$ the plastic flow potential. For ductile metals, the associated flow rule or normality rule is commonly applied. In this context, the plastic flow potential $g(\sigma_{ij})$ is equivalent to the yield criterion/potential $f_y(\sigma_{ij})$ so that the plastic strain increment vector $d\varepsilon_{ij}^{pl}$ is assumed to be normal to the yield surface. However, the associated flow rule may lead to discrepancies in the prediction of anisotropic yield and anisotropic strain behavior [48, 49]. Therefore, to better account for directional effects in plastic strain evaluation, non-associated flow rules were introduced in which the plastic flow potential $g(\sigma_{ij})$ is not equivalent to the yield potential $f_y(\sigma_{ij})$.

Hardening law

In stress-strain curves, a further increase in stress is usually observed after reaching the yield stress (figure 2.6b). This increase is associated with the impediment of dislocation movements by grain boundaries or the mutual obstruction of dislocations. However, this stress increase is not consistent with the yield criterion (equation 2.16), since this implies exceeding the defined yield surface. The previous defined yield criterion therefore represents an ideal-plastic material behavior with no further stress increase after reaching the yield stress, which does not occur in reality. In reality, the yield surface changes with plastic deformation (e.g., shape, size, location), enabling the increase in strength after reaching the yield point and thus the hardening of the material. To describe the strain hardening behavior within the yield function f_y (equation 2.16), the previous constant yield stress is replaced by a function of yield stress, which can be dependent on the equivalent plastic strain $\bar{\varepsilon}^{pl}$, equivalent plastic strain rate $\dot{\bar{\varepsilon}}^{pl}$, and temperature T:

$$\sigma_y(\bar{\varepsilon}^{pl}, \dot{\varepsilon}^{pl}, T). \tag{2.24}$$

An increase in temperature is associated with a softening of the material. Since no temperature effects are considered in this work, the influence of temperature is not further explained. The equivalent plastic strain $\bar{\varepsilon}^{pl}$ is defined as the integral of the equivalent plastic strain rate $\dot{\bar{\varepsilon}}^{pl}$

$$\bar{\varepsilon}^{pl} = \int_0^t \dot{\bar{\varepsilon}}^{pl} dt, \tag{2.25}$$

with the the equivalent plastic strain rate $\dot{\bar{\varepsilon}}^{pl}$ being

$$\dot{\bar{\varepsilon}}^{pl} = \sqrt{\frac{2}{3} \dot{\varepsilon_{ij}}^{pl} \dot{\varepsilon_{ij}}^{pl}}. \tag{2.26}$$

The two extreme cases of hardening are *kinematic* and *isotropic* hardening. In kinematic hardening, the yield surface is shifted in the direction of the stress by a kinematic back stress within the stress space (figure 2.2b). This results in anisotropic material behavior characterized by reduced yield stress upon load reversal after plastic deformation, referred to as the *Bauschinger effect* [46]. Since kinematic hardening is not considered in this work, it will not be discussed further. In isotropic hardening, the yield surface increases symmetrically about its origin in the stress space depending on the deformation history, i.e., the equivalent plastic strain $\bar{\varepsilon}^{pl}$ (figure 2.2c). The extent to which the size of the flow surface changes is defined by a *hardening law*. There are several empirical relationships that mathematically describe isotropic hardening based on experimental stress-strain curves. The most common strain hardening laws are listed below:

$$\sigma_{y,H} = K_H(\bar{\varepsilon}^{pl})^{n_H} \qquad \text{(Hollomon, [50])} \qquad (2.27)$$

$$\sigma_{y,L} = \sigma_{y0} + K_L(\bar{\varepsilon}^{pl})^{n_L} \qquad \text{(Ludwik, [51])} \qquad (2.28)$$

$$\sigma_{y,S} = K_S(\bar{\varepsilon}_0^{pl} + \bar{\varepsilon}^{pl})^{n_S} \qquad \text{(Swift, [52])} \qquad (2.29)$$

$$\sigma_{y,V} = \sigma_{ys,V} + (\sigma_{y0,V} - \sigma_{ys,V})e^{\frac{\bar{\varepsilon}^{pl}}{K_V}} \qquad \text{(Voce, [53, 54])} \qquad (2.30)$$

In the respective models, K corresponds to a material constant and n to the hardening coefficient, respectively. σ_{y0} corresponds to the initial yield stress, σ_{ys} to a saturation stress and $\bar{\varepsilon}_0^{pl}$ to an initial pre-strain, respectively.

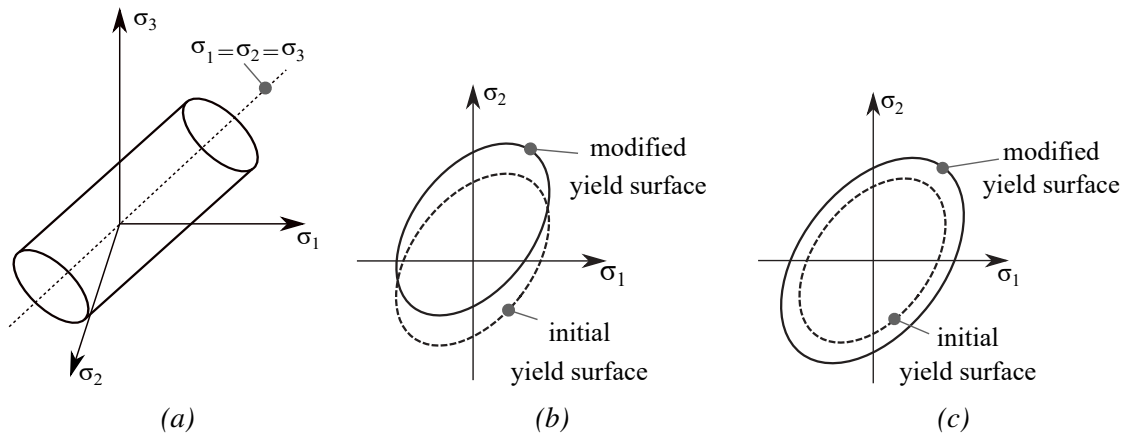

Figure 2.2: Schematic illustration of (a) the von Mises yield surface in 3D principal space and (b) the transition of the yield surface due to kinematic hardening in 2D principal space and (c) the extension of the yield surface due to isotropic hardening in 2D principal space.

2.2 Size effect and multiscale modeling of plasticity

For miniaturized parts, in which the dimensions of the structures are comparable to the size of the grains, it is likely that microstructural and surface effects will influence the mechanical behavior of the part. Microstructure is not explicitly modeled within the approaches of classical continuum mechanics. Thus, for a comprehensive analysis of the impact of microstructural features, higher-order micromechanical approaches, e.g. crystal plasticity (CP) models, are required. In this work, the influence of process-related geometric irregularities on the mechanical behavior of L-PBF stents is initially investigated based on continuum mechanics, thus neglecting the specific influence of the microstructure. Nevertheless, for a better understanding of the later discussion of the size effect, a brief overview of the different manifestations of the size effect in filigree metallic structures and approaches to their numerical representation using multiscale material modeling approaches is provided. For a more detailed description, it is referred to Refs. [55–57].

2.2.1 Size effect in metallic parts

The size effect can be categorized into the following categories: i) statistical size effects, ii) intrinsic size effects, iii) strain gradient effects and iv) surface constraint effects [55].

The statistical size effect occurs if the dimension of the structures is in a comparable range to the dimensions of the grains. The structures therefore only consist of a few grains across the load-bearing cross section. Thus, the mechanical behavior of the structure is strongly influenced by the mechanical properties of the individual grains since homogenization effects are hardly possible. The statistical size effect has been previously observed for conventionally manufactured 316L stent struts [58].

The intrinsic-size effect describes the influence of intrinsic length scales in the microstructure, such as Burger vector, grain sizes and widths. An example for the intrinsic size effect is the change in yield strength as a function of grain size due to dislocation accumulation at grain boundaries, described empirically by the Hall-Petch ratio[1].

The strain gradient size effect is associated with increasing strain gradients of miniaturized structures which must be accommodated by the curvature of the crystal lattice [55]. Thus, geometrically necessary dislocations are induced, which in return impend dislocation movement and thus increase the overall structural strength [55]. The surface constraint size effect is related to the ability of dislocations to slide through free surfaces. Depending on the surface condition,

[1] Hall Petch ratio: $\sigma_y = \sigma_0 + k_y/\sqrt{D_{grain}}$, with σ_y being the yield stress, σ_0 a material constant describing the stress at the onset of dislocation movement, k_y the strength coefficient, and D_{grain} the average grain diameter

dislocations are either unconstrained or constrained by some sort of surface boundary (e.g., hard coatings, oxide films), which in turn leads to either weakening or hardening of the structure [55]. The extent of surface constraint is restricted to a certain material volume. Thus, due to high surface-to-volume ratios this effect will become dominant for filigree structures.

2.2.2 Multiscale material modeling of plasticity

In the literature, various approaches for modeling material plasticity on different length and time scales exist (see figure 2.3). The continuum mechanical approach describes the material behavior at the macroscale. In this way, the material is homogenized, neglecting the impact of local variation in the microstructure. Thus, microstructural effects causing size effects or structural damage cannot be considered or analyzed. At the mesoscale, grain morphology and individual slip systems are explicitly modeled so that the distinct mechanical behavior of the material can be related to its microstructure. Mesoscale modeling of plasticity is based on the CP theory. In crystal plasticity (CP) modeling, the investigated part/material is represented by its microstructure, which consists of grains of various shapes and orientations. These are usually modeled using finite elements. Unless the dimensions of the investigated parts are comparable with the grain size, a representative volume element (RVE) is used for CP modeling. RVE are small volumes that statistically represent the microstructure of the part. These are either based on electron backscatter diffraction (EBSD) data or synthetically generated based on statistical methods. The material behavior of the individual grains within the RVE is considered based on CP theory. CP theory describes the deformation in a crystal lattice due to dislocation motions along crystallographic slip systems as a function of the shear stress acting on individual grains. By CP modeling, variations in mechanical properties can be attributed to microstructural features, such as crystallographic orientation or grain boundaries. For a detailed description of CP theory, its implementation within a FEA, as well as its application to the stent analysis, it is referred to Refs. [56, 57].

For the sake of completeness, modeling approaches based on the theory of dislocation dynamics, atomistics and molecular dynamics or quantum mechanics should also be mentioned here. However, since these approaches are rather reserved for fundamental research, they are not further described here. However, once the development of L-PBF stents is more advanced, these modeling approaches could be considered for studying stent fatigue behavior.

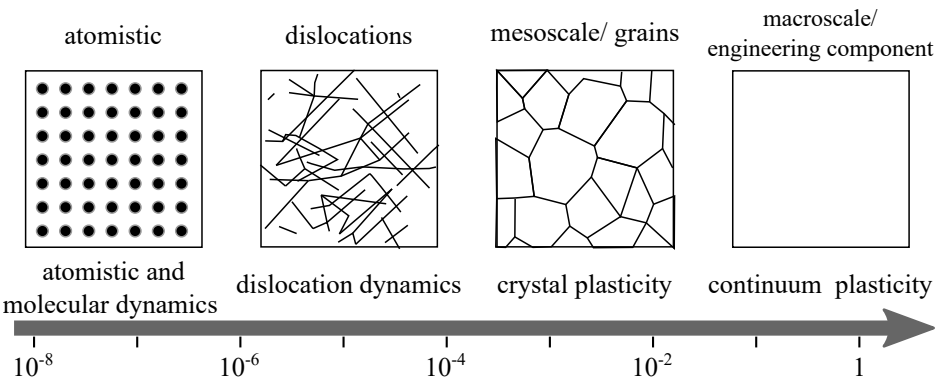

Figure 2.3: Overview of some common simulation methods for the analysis of mechanical material behavior of metals over various length scales.

2.3 Laser powder bed fusion

In this chapter, the L-PBF process is described and an overview of the associated microstructure and mechanical properties of L-PBF 316L is provided. For a more detailed review, please refer to Refs. [59–61]. Thereupon, the state of the art of L-PBF stents is presented. Since L-PBF stent research is at an early stage, this review is extended by a brief overview of relevant findings and challenges in the field of L-PBF lattice structures.

2.3.1 Process description

L-PBF is a powder-based AM process in which a part is build up layer-by-layer by completely melting of the powdered metals. During pre-processing, a 3D model of the intended part is generated (figure 2.4a) and virtually sliced into individual two-dimensional (2D) layers (figure 2.4b). Within the L-PBF process, the part is then built based on this layer model (figure 2.4c-d). Thereby, a thin layer of metal powder is applied to the build platform (figure 2.4c) and locally exposed and thus melted by the laser according to the intended geometry (figure 2.4d). As the melt solidifies, the individual melt tracks and the already solidified layer underneath are fused together. The most common scanning strategy is the contour-hatch strategy [62]. The contour is scanned with a contour scan, while the area bounded by the contour is filled with the hatch scan. After scanning the entire layer, the build platform is lowered (figure 2.4e), a new layer of powder is applied over the solidified part and selectively exposed and melted by the laser. This process is successively repeated until the part is completely created. Thereupon, the loose powder is removed from the build chamber and the part is separated from the build platform. After the actual build process, L-PBF parts are commonly subjected to post-processing steps, e.g., the removal of support structures and adhering powder particles, the smoothing of the part surface by surface treatment or the adjustment of the mechanical properties by heat treatment.

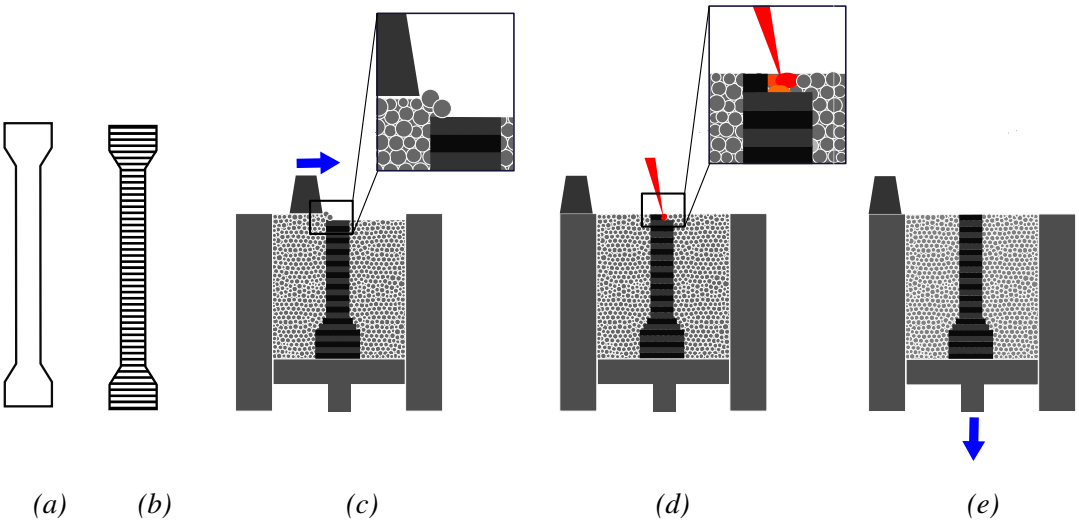

Figure 2.4: L-PBF process including the pre-processing and the actual manufacturing steps (b-d). (a) Intended L-PBF part. (b) Intended L-PBF part after virtual slicing. The lines indicate the later layers during the L-PBF build process. (c) Re-coating. (d) Local melting of the powder using the laser. (e) Lowering of the built platform. Steps (c-e) are repeated until the part is completely built.

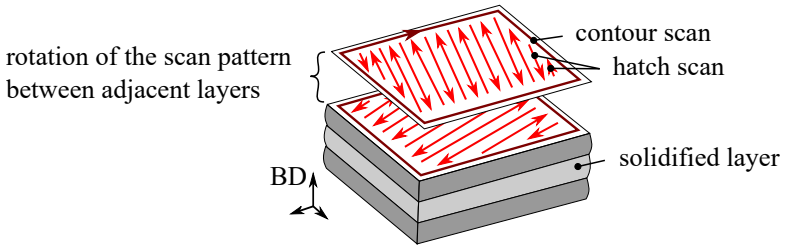

Figure 2.5: Contour-hatch strategy. The in-fill is scanned via the hatch scan (light red) and the edges of the parts via the contour scan (dark red). Furthermore, the rotation of the scanning pattern after each layer is illustrated.

2.3.2 Post-processing of L-PBF parts

In theory, L-PBF enables near-net-shape production. In most cases, however, post-processing steps are conducted following the actual L-PBF process, e.g. the removal of external support structures and surface and/or heat treatments. In the following a short overview of potential post-processing steps is provided.

Support structures are filigree structures which are used to connect the part to the build platform, to dissipate heat during the L-PBF process and to support overhanging surfaces [63]. After the build process, these structures are mechanically or (electro-)chemically removed from the part. For filigree specimens such as coronary stents, the use of support structures is hardly feasible since the diameters of the stent struts are in a comparable range to those of the support

structures making it almost impossible to remove the support structures without damaging the actual stents [27].

Surface and heat treatment, however, might be mandatory for L-PBF stents. Due to the layer-wise generation and the high temperature gradient between the solidified material and the powder bed, L-PBF parts exhibit high surface roughness. This is manifested by the so-called staircase effect in inclined part structures, as well as by adhering or partially melted powder particles at the part surface. The surface quality of the L-PBF parts can be improved by mechanical or electrochemical surface treatment. Due to the small structural size, surface treatment is only feasible to a certain extend without damaging the stents. For stents made of 316L, surface treatment by electropolishing is further mandatory to passivate the surface and thus ensure their biocompatibility [64].

Due to the complex thermal history during L-PBF process, the microstructure, and mechanical properties of L-PBF parts deviate from those of the conventionally manufactured counterpart. L-PBF parts are therefore commonly subjected to heat treatment to adjust their properties, e.g. by releasing residual stresses, increasing ductility or homogenizing the microstructure [65]. The influence of heat treatment on the microstructure and mechanical properties of L-PBF 316L is described in more detail in the subsequent chapter.

2.3.3 Microstructure and mechanical behavior of L-PBF 316L

As-built L-PBF 316L

Due to the layered build up and the complex thermal history during the L-PBF process, the microstructure of as-built L-PBF parts differs significantly from their cast or wrought counterparts. Thus, the microstructure is strongly influenced by the rapid solidification of the melt pools and the directional heat removal. In L-PBF parts, heat is mainly transferred along build direction (BD) as this represents the direction of the highest temperature gradient. The microstructure of L-PBF parts is thus characterized by periodic, overlapping melt pools and columnar, epitaxial grains along BD which further contain a fine cellular substructure [61, 65–70]. The fine cellular substructure (average cell size $D_{cell} \approx 530$ nm, [66]) combined with the elongated grains (with an average grain size of $D_{grain} \approx 29.5$ μm, [66]) results in a refined microstructure of the L-PBF parts compared to cast or wrought 316L (grain size $D_{grain} \approx 30$ - 60 μm) [60]. Apart from austenite, L-PBF 316L may contain a small amount of δ-ferrite, a strength enhancing second phase, due to rapid solidification [38, 70, 71]. Besides the strongly textured microstructure, internal porosity is an almost inevitable process-related defect of L-PBF parts commonly resulting from entrapped gases or lack of fusion [72]. The basic microstructure of as-built L-PBF 316L is illustrated in figure 2.6a.

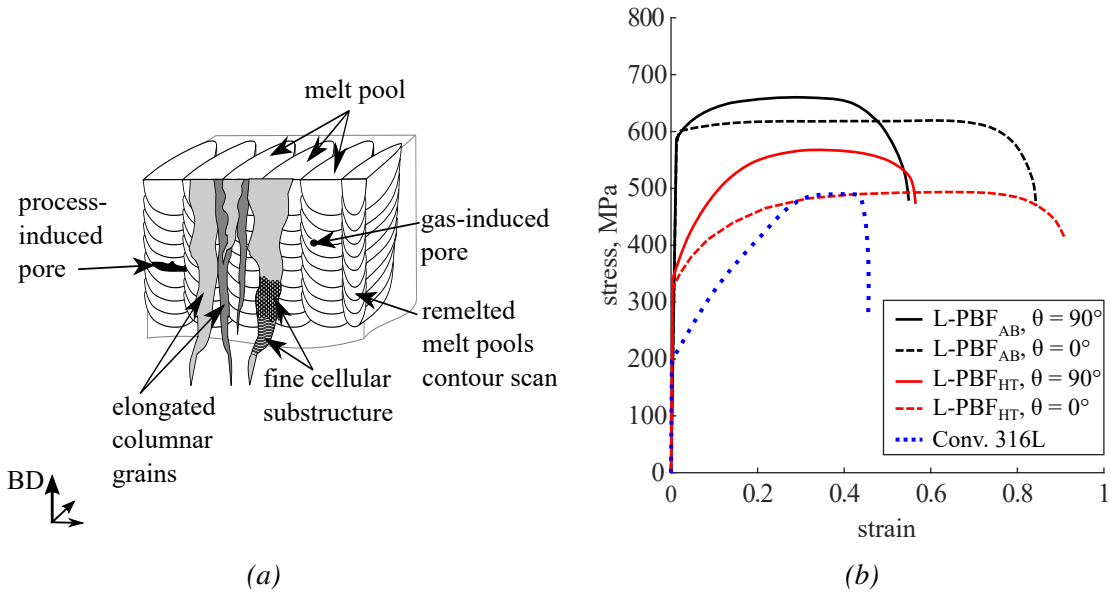

Figure 2.6: Microstructure and mechanical properties of L-PBF 316L. (a) Schematic illustration of the microstructure of as-built L-PBF 316L, adapted from Wiesent et al. [10]. (b) Comparison of stress-strain curves of as-built (AB) and heat treated (HT) L-PBF 316L tensile specimens with specimen orientation angles Θ of 0° and 90° (adapted from Shamsujjoha et al. [61]) with the stress strain curve of a conventionally manufactured 316L tensile specimen (adapted from Gorsse et al. [60]). The specimen orientation angle Θ is referred to as the angle between longitudinal tensile specimen axis to build direction.

The mechanical properties of as-built L-PBF 316L are commonly characterized by higher yield strength, higher tensile strength, lower ductility, and lower strain hardening behavior compared to conventionally processed 316L. In literature, yield strength of L-PBF 316L tensile specimens of $\sigma_y \approx 400$ - 600 MPa and ultimate tensile strength of $\sigma_{UTS} \approx 500$ - 800 MPa have been reported [61, 68, 69, 73, 74]. Conventionally processed 316L in return exhibits values of $\sigma_y \approx 170$ - 200 MPa and $\sigma_{UTS} \approx 415$ - 485 MPa [75], respectively. The increased strength of L-PBF 316L is attributed to its refined grain structure, high dislocation densities, and residual stresses [8, 60, 76, 77]. Therefore, as per the Hall-Petch ratio a refined microstructure and thus a reduction in average grain size causes an increase in the yield strength of L-PBF parts. High dislocation densities and residual stresses arise from the spatial temperature gradient as well as thermal expansion and contraction of the material during rapid heating and cooling during the L-PBF process. For L-PBF 316L dislocation densities of $\rho_d \approx 10^{15}$ m/m^3 were reported which are in a comparable range of the dislocation densities observed in highly deformed metals [60, 61]. These high dislocation densities cause a saturation with respect to strain hardening thus further promote the increase in strength inherent of L-PBF material in the as-built condition [8, 60, 76, 77]. The elongation at break of L-PBF parts was found to have a large variance, which is commonly related to L-PBF process-related defects such as pores, lack of

fusion, surface roughness or notches [68, 73, 78].

Due to the strongly textured microstructure, as-built L-PBF parts exhibit anisotropic mechanical properties depending on the specimen orientation angle to BD [59, 60, 68, 73, 74]. In the following, the specimen orientation angle Θ is always referred to as the angle of the longitudinal specimen axis to BD. For the analysis of the anisotropic material behavior, studies commonly focus on the differences between the mechanical properties of specimen orientation angles of $\Theta = 0°$ (longitudinal specimen axis parallel to BD) and $\Theta = 90°$ (longitudinal specimen axis perpendicular to BD) [68, 78, 79]. L-PBF tensile specimens with a specimen orientation angle of $\Theta = 90°$ were found to exhibit an increased yield strength compared to specimen with an orientation angle of $\Theta = 0°$. This phenomenon is initially associated with the grain orientation/size (i.e., the Hall-Petch ratio) with respect to loading direction (figure 2.7) [60]. At a specimen orientation angle of $\Theta = 90°$, the columnar grains and thus the finest grain dimension are perpendicular to the loading direction, resulting in increased strength according to the Hall-Petch ratio (figure 2.6b, solid lines). At a specimen orientation angle of $\Theta = 0°$, the columnar grains are parallel and thus the coarsest grain dimension is perpendicular to the loading direction resulting in decreased strength (figure 2.6b, dashed lines) [60]. Moreover, anisotropy is further associated with the orientation of defects, in particular lack of fusion defects, with respect to loading direction [60]. Thus, it is assumed that the opening of defects parallel to the loading direction (e.g., lack of fusion defects of specimens with an orientation angle of $\Theta = 90°$, figure 2.7c) occurs at a relatively high stress level, while defects perpendicular to the loading direction (e.g., lack of fusion defects of specimens with an orientation angle of $\Theta = 0°$,figure 2.7b) occur at a relatively low stress level.

Comprehensive studies which consider a higher number of specimen orientation angles are currently limited. Among other, Hitzler et al. [73] and Tosola et al. [74] investigated tensile specimens with specimen orientation angles of $\Theta = 0$, 15°, 45°, 75° and 90° and $\Theta = 0°$, 30°, 45° and 90°, respectively. These studies also observed the trend of increasing specimen strength from a specimen orientation angle of $\Theta = 0°$ to $\Theta = 90°$. However, the maximum strength value was observed at a specimen orientation angle of $\Theta = 45°$. Gorsse et al. [60], on the other hand, found an increase in strength from a specimen orientation angle of $\Theta = 0°$ through specimen orientation angle of $\Theta = 45°$ to a maximum strength value at a specimen orientation angle of $\Theta = 90°$. Due to this inconsistency, more studies are required to obtain a more profound knowledge regarding the impact of specimen orientation on the mechanical properties of L-PBF parts. Furthermore, Chen et al. [80] observed a tension-compression asymmetry with the yield strength from uniaxial compression being ≈ 10 % higher than the yield strength from uniaxial tensile tests. At this point, one must emphasize that the mechanical behavior of L-PBF materials is strongly dependent on the selected L-PBF process parameters. An absolute quantitative comparison of the findings of different studies is therefore only possible to a limited extent. To derive general trends, more

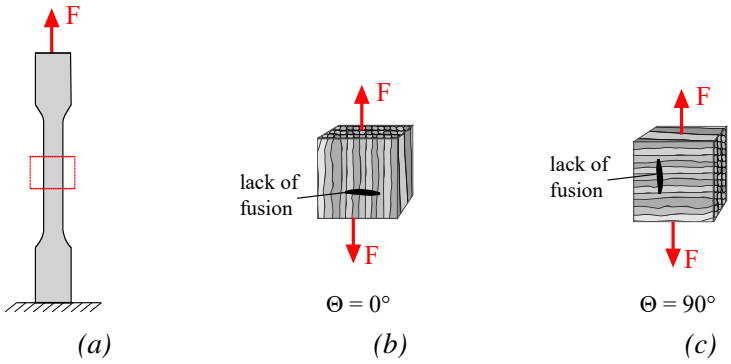

Figure 2.7: Schematic illustration of the orientation of microstructure and lack of fusion defects of L-PBF tensile specimens with respect to loading direction during uniaxial tensile tests. (a) Loading condition of a tensile specimen which is subjected to a force F in the uniaxial tensile test. (b) Loading condition of a L-PBF tensile specimens with an orientation angle of $\Theta = 0°$ with the columnar grains and thus the finest grain dimension parallel to the loading direction while the lack of fusion defect is perpendicular to loading direction. (b) Loading condition of a L-PBF tensile specimens with an orientation angle of $\Theta = 90°$ with the columnar grains and thus the finest grain dimension perpendicular to the loading direction while the lack of fusion is parallel to loading direction. Θ is referred to as the angle between longitudinal tensile specimen axis to build direction.

extensive studies with different specimens and process parameters are therefore necessary.

To date, knowledge regarding the impact of specimen thickness is still limited as most of the studies were conducted on bulk material specimens with a thickness of $t > 1$ mm. However, since the specimen size affects the thermal history during L-PBF and thus the associated microstructure of the L-PBF part, size-dependent mechanical properties of L-PBF parts are expected.

Heat treated L-PBF 316L

Following the actual manufacturing process, L-PBF parts are commonly subjected to heat treatment aiming at e.g., relieving residual stresses, homogenizing or recrystallizing the microstructure. Heat treatment of L-PBF 316L at temperature of $T = 700$ °C was found to primarily reduce the dislocation density and residual stresses and to slightly increase the cellular substructure, while not altering the remaining microstructure [66, 81, 82]. From a temperature of $T = 900$ °C, the dissolution of melt pool boundaries and the cellular substructures was observed and found to completely vanish at a heat treatment temperature of $T = 1050$ °C [40, 66, 81, 83]. Heat treatment at a temperature of $T = 1050$ °C was further found to reduce/dissolve δ-ferrite leading to a reduction of strength of the L-PBF specimen [38]. From a heat treatment temperature of $T = 1200$ °C, a change in grain size and shape and recrystallization was reported. Thus, the grain size was found to increase, e.g., from an average grain size $D_{grain} \approx 29.5$ μm to $D_{grain} \approx 54$ μm and the overall microstructure was found to become more homogeneous [40, 66, 83]. Thus, heat treated L-PBF 316L was found to exhibit increasingly isotropic properties and higher

ductility, becoming more similar to the wrought 316L specimens [83]. Furthermore, the tension-compression asymmetry of L-PBF was found to be nearly resolved after heat treatment a temperature of T = 1200 °C [80].

2.3.4 Current status and challenges in L-PBF stents/ lattice structures

L-PBF stents

Research in the field of L-PBF metallic coronary stents is still at an early stage. The first study on L-PBF stents was published in 2017 by Demir et al. [26] which proved the basic feasibility of generating L-PBF CoCr stents. Thereupon, design guidelines for L-PBF stents were derived by the same research group [27]. These guidelines define the requirements for a stent design to be built without support structures via L-PBF. These guidelines arise from the fact that the diameters of the struts of coronary stents are of comparable dimensions/diameters to current L-PBF support structures. Therefore, it is almost impossible to remove the support structures from the stent without damaging it. Therefore, only self-supporting stent designs are possible according to the current state of the art. The theoretically very high degrees of design freedom of the L-PBF can thus only be exploited to a limited extent in coronary stents due to the small structure size.

Recently, two independent studies have demonstrated the basic functionality of L-PBF stents made of CoCr [31] and a new Fe–30Mn–1C–0.02S alloy (FeMnCS) [32] alloy during balloon-stent expansion. However, quantitative analysis of the mechanical behavior of the L-PBF stents were only investigated to a limited extent in these studies. Hufenbach et al. [32] performed tensile tests on round L-PBF FeMnCS bulk tensile specimens with a diameter of D = 3.0 mm, providing information on the behavior of the bulk material rather than the behavior of the stent. Finazzi et al. [31], on the other hand, performed tensile testing on miniaturized L-PBF CoCr tensile specimens in the as-built condition. In the measurement area, these specimens had a quadratic cross section with a thickness of $t \approx 90/120$ μm (analogous to the stent struts) and a length of l = 6.0 mm. The specimen shoulder, however, had a width of w = 3.0 mm. Even though the cross sections of these miniature tensile specimens were comparable to the later stent struts, the transferability of the mechanical properties thus determined to L-PBF stents must be critically evaluated and verified. In this context, the effect of the deviating slenderness ratio of the miniature specimens and the later stent struts, i.e., the ratio of specimen diameter to specimen length, which is associated with a decrease in ultimate strain as the slenderness ratio increases, should be evaluated [84]. In addition, the thermal profile of the miniature tensile specimens is expected to be different from that of the stent material because of the proportionally massive specimen shoulders.

Besides the challenges in determining the mechanical properties of the L-PBF stent material,

Finazzi et al. [31] further observed process-related geometric irregularities, e.g., strut waviness, irregular strut cross sections, and an increase in the as-built diameter compared with the intended strut diameter of up to 60 % for the L-PBF CoCr stents. Although these irregularities could partially be compensated by surface treatment, they represent a major challenge not only in terms of manufacturing efficiency but also in terms of structural safety. As mentioned earlier, research on L-PBF stents is still quite nascent and limited to number of studies of mainly two research groups [26, 27, 31, 32]. Thus, in-depth investigations on the distinct influence of process-related geometric irregularities and post-processing steps (surface and heat treatment) on the mechanical properties of L-PBF stents are hardly available. Furthermore, no numerical investigations of L-PBF stents have been conducted so far, and thus the transferability of methods established in the field of conventional stents to L-PBF stents has not yet been demonstrated. However, these studies and numerical models are essential to ensure the safety of L-PBF stents and to ensure efficient development and optimization of L-PBF stent designs.

L-PBF lattice structures and process-related geometric irregularities

L-PBF stents can be considered as L-PBF lattice structures with a low relative density[2] ρ^*. Due to the similar topology and structure size, the findings from L-PBF lattice structures should be transferred to L-PBF stents, especially since the process-related geometric irregularities observed in L-PBF CoCr stents were also found in L-PBF lattice structures, e.g. strut waviness, surface roughness and deviations in the strut diameters and shapes [25, 34–37]. Unlike L-PBF stents, findings are already available for L-PBF 316L lattice structures. In the following a brief overview of these L-PBF process-related geometric irregularities is provided.

In L-PBF lattice structures, the filigree struts are predominantly composed of single stacked melt pools (figure 2.8a). The resulting sphere pile-like defects lead to the observed strut waviness, especially if the exact positioning of the laser over the previous melt pool is not guaranteed [29, 85, 86]. The high surface roughness is caused by (partially melted) powder particles adhering to the strut surface due to the high thermal diffusion caused by the high temperature gradient between the solidified and the powder material [28, 29]. The extent of the surface roughness was further found to be dependent on the strut inclination [85, 87]. This is associated with the various thermal history of the structures and lower thermal conductivity of the powder compared to the bulk material. For vertical struts, heat is mainly dissipated through the solidified strut (figure 2.8a, red arrows). For inclined struts, however, heat is further dissipated through the sintered powder causing heat accumulation and over-melting on the downward facing strut surface, the formation of spatter, as well as an increased adhesion of powder particles on the strut surface and thus an increase in surface roughness (figure 2.8b, red arrows) [85, 87]. The

[2]For lattice structures, the relative density is defined as the ratio of the measured lattice density ρ to the density of the solid material ρ_s, i.e., $\rho^* = \frac{\rho}{\rho_s}$

increased strut thicknesses in L-PBF lattice structures are associated with the increased melt pool diameter compared to the laser spot [88, 89].

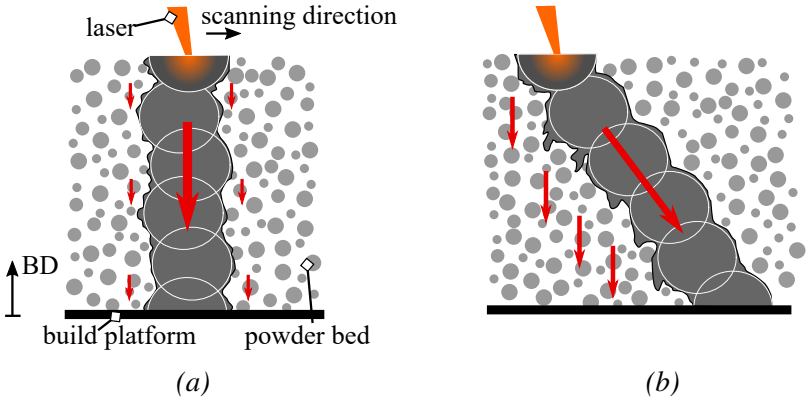

Figure 2.8: Heat flux during laser powder bed fusion for vertical and inclined struts and the associated process-related geometric irregularities, redrawn and modified from Ref. [85]. (a) For vertical struts, heat is mainly dissipated via the solidified struts with only a few partial melted powder particles adhering to the strut surface. (b) For inclined struts, heat is dissipated via the powder and the strut resulting in spatter and increased amount of partially melted powder at the downward-facing strut. The sphere pile-like defects are indicated by the white dotted spheres. The intensity and direction of the heat flux is indicated by the size and orientation of the red arrows. build direction (BD) is indicated by the black arrow.

Mechanical analysis of L-PBF lattice structures is mainly performed by compression tests between two plates, which provide insights into the macroscopic compression behavior of the structures. In combined experimental and numerical studies it was found that the process-related geometric irregularities have a significant effect on the mechanical behavior of L-PBF lattice structures, causing discrepancies between the numerical prediction based on the as-designed geometry and the experimentally determined mechanical response of L-PBF structures [25, 34–37]. Thus, for an accurate prediction of the process-structure-property relationship of L-PBF lattice structures, the process-related geometric regularities are commonly incorporated within the numerical models by the explicit reconstruction from, e.g., X-ray computed tomography (CT) of the L-PBF lattice structures or by statistical considerations [25, 34–36]. Previous studies on L-PBF 316L lattice structures further found, that the mechanical behavior of single L-PBF struts strongly deviate from the material behavior obtained from bulk L-PBF 316L tensile specimens. Thus, a reduction in strength of L-PBF 316L struts (D_{strut} = 200 μm) by 25 % compared to L-PBF 316L bulk material was observed [25].

The analysis of process-related irregularities and the associated mechanical behavior of lattice structures is currently limited to investigations on as-built L-PBF lattice structures. Further research is therefore required to investigate the influence of post-processing steps such as surface and/or heat treatment, which may be mandatory for L-PBF stents due to their requirements for

high ductility and biocompatibility.

2.4 Numerical analysis of cardiovascular stents

The mere experimental analysis or optimization of the mechanical behavior of stents is very resource and time consuming. Therefore, computational models were established to reduce or even replace experimental stent/material tests or ethically controversial animal experiments. Within these models, different 'what if?'-scenarios, e.g., variations in the material, geometry or loading condition, can be analyzed without producing the stent. Computational stent analysis can be divided into three categories: i) Structural mechanical analysis, e.g. the analysis of the stresses and strains within the stent/arterial wall, is based on the finite element method (FEM) [20, 42, 90, 91]. ii) Fluid dynamic analyses, e.g. alteration in hemodynamics or wall shear stress following stent implantation, are based on the computational fluid dynamics (CFD) [42, 90, 92, 93]. iii) The combination of these methods, the so-called fluid-structure interaction (FSI)-analysis, concerns the investigation of the mutual influence of the structure (stent) and the surrounding flow (blood flow) [94–96]. This work focuses on the structural mechanical analysis of stents using FEA. In the following an overview of the current state of the art of stent FEAs is provided.

2.4.1 Finite element analysis of stent expansion

In the literature various FEAs of stents exit including investigations into stent flexibility [13, 43, 97–99], compression [100, 101] and longitudinal resistance [97]. The main focus, however, is on stent expansion analysis [20, 41, 91, 97, 102–107]. Thereby, the complexity and thus the accuracy of the stent expansion FEAs varies, ranging from investigations on single planar unit cells (e.g., a stent diamond) [91] to detailed analysis of the balloon-stent expansion behavior within a reconstructed patient-specific artery [42]. In general, stent expansion analysis can be divided into *free* and *confined* analysis. In the FEA of free stent expansion, stent expansion is analyzed without considering external resistance, i.e., neglecting the surrounding tissue/arterial wall. This allows the stress states and expansion behavior of the stent to be efficiently investigated, enabling resource-efficient identification of necessary design changes or comparison of different stents/materials. Confined stent expansion analysis, also known as stent-artery interaction analysis, analyzes stent expansion by explicitly modeling the surrounding tissue and considering external resistance. In this way, stent-induced arterial stress can be evaluated, and the potential ISR risk of different stent designs can be assessed under different external boundary conditions (e.g., curved, tapered, patient-specific arteries) without performing ethically questionable animal experiments.

Stent model

The morphology of conventionally manufactured stents (laser-cut or coiled stents) is almost identical to that of the intended computer aided design (CAD) stent model. Therefore, it is common practice to derive the stent finite element (FE) model from the intended stent CAD model. Most metallic balloon-expandable stent models consider stents made of 316L [20, 107] or CoCr [57, 94, 97]. The inelastic material behavior of balloon-expandable stents is commonly described using a von Mises plasticity model with isotropic hardening. Thus, the stent material is considered homogeneous. Only a few studies consider higher-order micromechanical approaches based on CP theory that explicitly model grain structures of the respective stent material to identify local stress and strain fields within the microstructure [57, 108, 109]. These CP studies focus on the impact of the size effect on stent deformation [109] or the effect of microstructure on the stent fatigue behavior [57, 108]. Since these CP models are very computationally intensive, they are limited to the analysis of individual loaded strut segments or stent unit cells and are commonly not used for the analysis of the macroscopic expansion behavior of the stent.

Models of free stent expansion

There are mainly three approaches for modeling stent expansion: i) *load-controlled*, ii) *displacement-controlled* and iii) *balloon-stent* expansion (figure 2.9). These approaches are used in both free and confined stent analysis. A brief overview of these approaches and their limitations is provided below.

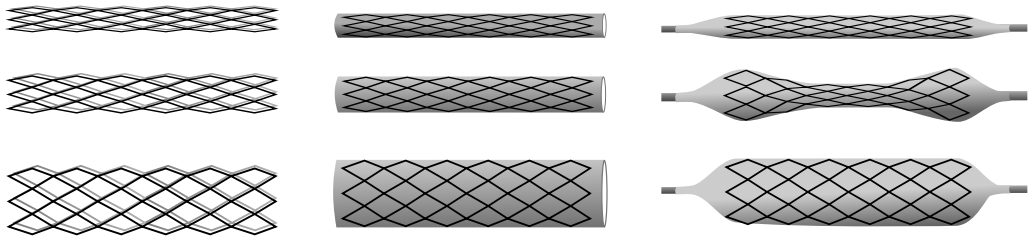

Figure 2.9: Approaches for numerical stent expansion analysis. (a) Load-controlled stent expansion by applying a homogeneous pressure to the inner surface of the stent. (b) Displacement controlled expansion by expanding a semi-rigid cylinder. (c) Balloon-stent expansion by explicitly modeling the balloon and applying a homogeneous pressure to the inner balloon surface.

The load-controlled expansion approach is based on the assumption that the balloon is negligible due its low stiffness compared to the stent [20, 41, 91, 102–104, 110]. Therefore, stent expansion is achieved by directly applying a homogeneous pressure at the internal surface of the stent (figure 2.9a). Since the load-controlled stent expansion approach does not require the consideration of extensive contact conditions, this approach is particularly computational efficient. However, comparative studies have shown that this approach might lead to a rather unrealistic (partly barrel-shaped) expanded stent shapes [20, 102].

In the displacement-controlled expansion approach, a rigid/deformable cylinder is used as an expansion device by increasing its diameter within a radial coordinate system (figure 2.9b) [20, 97, 102, 105, 106, 111]. Comparative studies have shown that this is a computationally efficient method for evaluating the final expanded stent shape and associated stresses [20, 97, 102]. However, since the basic shape of the stent is indirectly determined by the cylinder, the transient stent expansion, i.e., the evolution of the DB ratio, cannot be depicted with the displacement-controlled expansion approach.

In the balloon-stent expansion approach, the balloon is explicitly modeled, and stent expansion is indirectly achieved by applying a pressure to the inner balloon surface (figure 2.9c). In initial studies, the balloon was approximated as an elastic/hyperelastic cylinder without modeling the balloon folding pattern [102, 112–114]. Although these simulations depicted the evolution of the DB ratio in the initial phase of stent expansion, significant deviations from the experimental data were observed in the further course of stent expansion [112]. Moreover, a deviation of the predicted foreshortening behavior of the stent from experimental data was observed [114]. In 2008, de Beule et al. [20] succeeded in simulating stent expansion based on a folded non-tapered balloon model based on CT-data for the first time. By comparing the balloon stent expansion simulation results with the load- and displacement-controlled stent expansion results, they concluded that the transient stent expansion behavior can only be predicted by explicitly modeling the balloon folding pattern [20]. In a later comprehensive study on stent crimping and expansion, Bukala et al. [41] found that, in addition to the balloon folding pattern, residual stresses caused by crimping the stent onto the balloon catheters have a decisive influence on the expansion behavior of the stents and must therefore be considered in the numerical analysis. In a most recent study, Geith et al. [107] presented a comprehensive study involving the balloon folding process, stent crimping and subsequent balloon-stent expansion. In contrast to previous studies that approximated the balloon material as linearly elastic, they described the inelastic material behavior of the semi-compliant balloon material more realistically using a von Mises plasticity model with isotropic hardening.

In summary, there are various approaches for simulating the stent expansion, which vary greatly in their complexity and computational efficiency. For the analysis of the transient stent expansion behavior, the modeling of the balloon folding pattern including the preliminary crimping was found to be essential [20, 41]. For a mere stress analysis,, however, a simplified and thus computationally more efficient stent expansion approach, such as the displacement-controlled approach, could be considered. Therefore, to efficiently use computational models for the development/optimization of stents, the respective expansion approach should be chosen according to the engineering maxim '*Not as accurate as possible, but as accurate as necessary*'.

The main limitation of current stent FEAs is their limited experimental validation, as well as idealized character of the stent expansion simulation. Current existing validation approaches

are mainly limited to qualitative validation. Thereby, the focus is on the visual prediction of the DB ratio, without its quantitative evaluation, e.g., the actual evolution/shape of the DB ratio, the elastic recovery (recoil) or the shortening of the stent after expansion. In the following, a short overview of the existing quantitative validation is given. De Beule et al. [20] performed a quantitative validation by comparing the predicted development of the central stent diameter with the manufacturer's compliance chart representing the relationship between central stent diameter and the inflation pressure. Validation of further expansion characteristics (e.g., DB ratio) was only qualitatively performed by visual comparison of the predicted expansion pattern with images of expansion tests of similar stent from the literature. Bukala et al. [41] quantitatively validated their stent crimping model by comparing the predicted reaction forces of the crimping jaws with experimental data. Thereby, the numerical predictions were in good agreement with the experimental data in the initial phase of crimping (elastic deformation) but underestimated the reaction forces in the further course of crimping (plastic deformation). Most recently, Geith et al. [107] performed a qualitative validation of balloon folding by a visual comparison of balloon folding from μ-CT scans, as well as a visual validation of the numerical predicted stent expansion behavior with high-speed camera images of experimentally expanded stents. As indicated before, apart from the limited validation of the numerical stent models, the idealized character of this models represents a further limitation. So far, only stents with typical expansion behavior, i.e., pronounced DB ratio or ideal central positioning of the stent on the balloon catheter, were considered. However, only by considering more comprehensive stent expansion scenarios in combination with experimental validation the universal applicability and validity of the computational stent models can be ensured.

Models of stent-artery interaction

To analyze stent-artery interaction, the models of free stent expansion are extended to include an arterial model as well as associated contact conditions. The implemented artery models range from simple cylindrical to reconstructed patient-specific models [9, 42, 115, 116]. Furthermore, the consideration of artery wall properties varies from homogenized material properties for the entire artery to the assignment of layer-specific material properties (figure 2.10) [115, 116]. The mechanical behavior of the arterial wall or a single arterial layer is commonly described by an isotropic hyperelastic constitutive model, such as the reduced form of the generalized *Mooney-Rivlin model*, describing the strain energy function W as

$$W = a_{10}(I_1-3)+a_{01}(I_2-3)+(I_2-3)+a_{20}(I_1-3)^2+a_{11}(I_1-3)(I_2-3)+a_{02}(I_2-3)^2 \tag{2.31}$$

with a_{ij} being the hyperelastic constants and I_1, I_2, I_3 the strain invariants [115]. The material constants are determined from experimental tests, including uniaxial and biaxial tensile tests on human arteries or single arterial layer, respectively [115, 117].

Based on FEAs of stent-artery interaction, the impact of distinct stent design parameters on the stent induced arterial stresses can be evaluated. In addition, patient-specific arterial reconstruction can be used to evaluate various stent treatment options before treating the patient.

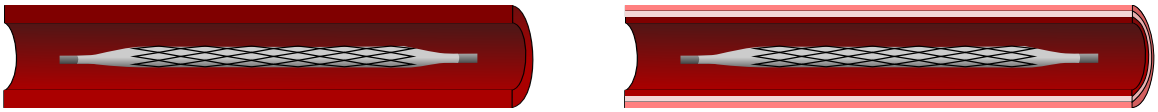

(a) *(b)*

Figure 2.10: Schematic illustration of arterial wall models. (a) Single-layer arterial model in which the material properties of the arterial wall are homogenized by a hyper-elastic constitutive model with a single set of material constants. (b) Three-layer arterial model in which the material properties of the different arterial wall layers (from inside to outside: Tunica intima, media, and adventitia) are each considered by a hyper-elastic constitutive model with an individual set of material constants.

2.5 Summary

Based on the literature review, the following conclusion can be drawn:

- Advances in L-PBF enable the generation of filigree L-PBF lattice structures and thus, in principle, coronary stents. L-PBF stents could enable new or even patient-specific stent designs and thus increase the long-term clinical success of stent implantation. Currently, there are only a few studies on L-PBF stents which mainly focus on their basic feasibility and functionality. Comprehensive experimental or numerical analyses of L-PBF stents are not available so far. However, such analyses are essential to investigate the structural integrity of the L-PBF stents.

- Various approaches for the FEA of stent expansion exist. Within these approaches, the stent model is commonly derived from a CAD model while the stent material behavior is approximated by continuum mechanics approaches, such as the von Mises plasticity model. A major limitation of current stent FEAs is the lack of comprehensive validation and their idealized nature. Therefore, it is necessary to validate these simulation approaches using extensive scenarios, e.g., by considering stents with atypical expansion behavior or decentralized positioning on the balloon catheter, to justify their broad applicability, e.g., for novel L-PBF stent designs.

- L-PBF is associated with a complex thermal history leading to a inhomogeneous microstructure, high strength, low ductility, and anisotropic material behavior in L-PBF materials. Subsequent heat treatment can influence the microstructure and mechanical behavior, e.g. by dissolving to residual stresses, homogenization, or recrystallization. So

far, mechanical investigations have been performed mainly on large-sized as-built L-PBF specimens and should be extended to analyze the effects of different specimen thicknesses, specimen orientation angles, and heat treatments. Moreover, further methods for the characterize of the L-PBF stent material behavior, e.g., within a combined experimental and numerical framework, should be considered.

- L-PBF lattice structures/ stents are affected by process-related geometric irregularities, which cause deviations between the actual and the intended L-PBF structure. Combined experimental and numerical investigations have shown that these geometric irregularities significantly influence both the morphology and the mechanical behavior of the L-PBF lattices structures. It is therefore likely that numerical methods established for conventionally manufactured stents have limited applicability to the analysis of L-PBF stents. To date, studies on the influence of process-related irregularities on the mechanical behavior of L-PBF lattice structures, are limited to the as-built condition. However, for L-PBF stents, post-processing steps, such as heat or surface treatment, may be mandatory to meet the high mechanical and biological requirements of the stent application. Therefore, besides the influence of process-related irregularities, the influence of post-processing steps on the mechanical behavior of L-PBF stents must be determined and a method for the numerical analysis of L-PBF stents must be derived.

3 Outline of this study

This doctoral thesis aims at the numerical analysis of L-PBF 316L stents considering process-related geometric irregularities and different post-processing conditions. In a first step, a numerical model was developed and validated based on conventionally manufactured stents. Thereupon, the mechanical behavior of L-PBF tensile specimens was experimentally determined focusing on the analysis of the impact of specimen thickness, orientation angle and heat treatment. However, it was found that the mechanical properties of tensile specimens could not be transferred to filigree L-PBF stents due to the size effect. Therefore, in a subsequent study, the macroscopic mechanical properties of L-PBF stents were determined using a combined experimental and numerical analysis of the uniaxial compression of L-PBF 316L stent between two plates. Subsequently, FEA of L-PBF stents expansion was conducted considering different L-PBF stents post-processing conditions.

The work performed as part of the doctoral thesis resulted in three peer-reviewed research papers, which form the foundation of chapter 4, 5 and 6. Within the scope of this doctoral thesis, the content of these papers were slightly revised and partially supplemented. The structure of this doctoral thesis is shown in Figure 3.1.

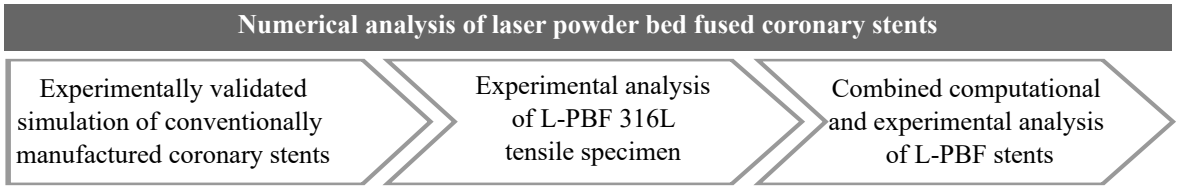

Figure 3.1: Structure of this doctoral thesis.

In **chapter 4**, numerical models for stent expansion analysis are presented and validated against experimental data. The stent models were based on two conventionally manufactured stent designs, which are representative of both typical and atypical stent expansion behavior. For the numerical stent expansion analysis, a detailed balloon-stent expansion approach including the preceding balloon folding and stent crimping as well as a displacement-controlled stent expansion approach were investigated. To prove the universal applicability of the stent FEAs, different stent expansion scenarios (two stent designs, two stent positioning with respect to the balloon catheter) were investigated and subsequently validated by experimental data.

In **chapter 5**, the experimental analysis of the mechanical behavior and microstructure of L-PBF 316L is presented focusing on the influence of specimen thickness, specimen orientation angle and homogenization heat treatment on the mechanical behavior of L-PBF tensile specimens.

In **chapter 6**, a method for the numerical analysis of the L-PBF stents is presented. Initially, the process-related geometric irregularities were analyzed using scanning electron microscopy (SEM) images and CT scans of L-PBF stents. Thereupon, the mechanical behavior of the L-PBF stent in the as-built and heat treated condition was determined within a combined experimental and numerical framework based on the macroscopic mechanical behavior of the L-PBF stent under compression. To exclude the influence of process-related irregularities on the mechanical behavior of the stents, the L-PBF stent models were reconstructed from CT data of actual L-PBF stents. The derived flow curves were subsequently implemented within the FEAs of L-PBF stent expansion based on the validated models from chapter 4. In addition to the reconstructed L-PBF stent models in the as-built condition and heat treated condition, a reconstructed L-PBF stent model of an electropolished and heat-treated L-PBF stent was considered. Furthermore, a stent model based on the intended stent CAD model was analyzed to determine the deviation of the mechanical response of the actual L-PBF stents from the intended stent.

Finally, one must emphasize that this work is based on some preliminary internal work and fruitful cooperation. This concerns, among other things, the generation of the L-PBF specimens and L-PBF stents, the stent designs, and the post-processing of the L-PBF stents. All L-PBF specimens and L-PBF stents were provided by the FIT AG[1]. Therefore, an already established L-PBF process parameter set was used and remained fixed for comparability reasons. The investigated stent designs are adopted from previous work by the Medical Devices Lab at OTH Regensburg under the direction of Prof. Dr.-Ing. Schratzenstaller. The definition of the required parameters for post-processing of the stents, i.e., heat treatment, electropolishing, was determined in the Material Science and Surface Analytics Lab at the OTH Regensburg under the direction of Prof. Dr.-Ing. Noster. The post-processed stents were kindly provided for the analyses within the scope of this work.

[1] FIT AG, Lupburg, Germany

4 Experimentally validated simulation of conventional manufactured stents

Various computational studies on computational stent analysis using FEA are found in literature [20, 41, 91, 97, 102–107]. These were established to reduce or even replace experimental stent/material tests or ethically controversial animal experiments and thus to enable efficient stent development and optimization. However, the inadequate or missing validation remains a significant limitation of these stent FEAs.

In this chapter, an experimentally validated FEA of free stent implementation is presented including the simulation of balloon folding, stent crimping onto the balloon catheter, and balloon-stent expansion. To ensure its the broad applicability, two stent designs with different expansion characteristics were considered within the FEA: i) stent$_{hom}$ with homogeneous stiffness along the stent length and ii) stent$_{het}$ with heterogeneous stiffness along the stent length. In addition to the common central positioning of the stent on the balloon catheter, decentralized positioning of the stent was further considered. A major focus was on the experimental validation of the simulations. Therefore, the predicted crimped and expanded stent shapes, the balloon folding pattern as well as the transient stent expansion behaviors were validated against experimental data. Furthermore, a comparison of the balloon-stent expansion approach with the displacement-controlled expansion approach was conducted. The displacement-controlled expansion approach is a simplified and computationally efficient method for stent analysis. Its validation and comparison with the balloon-stent expansion approach aimed to identify specific research objectives (e.g., efficient stress analysis of the expanded stent) for which the use of this simplified approach is appropriate, balancing accuracy and computational efficiency whenever possible.

In this chapter, the focus is on the FEA of conventionally manufactured 316L stents, which allows their experimental validation using established manufacturing and stent testing procedures. Once validated, this FEA may be used or further adapted for subsequent analysis of L-PBF stents (chapter 6). The content of this chapter was published in Wiesent et al. [10] and was only slightly adapted and supplemented in the context of this work.

4.1 Stent design

The two investigated stents were based on the prototype stent design ESPRIT V1[1] (figure 4.1a). The stents are composed of nine rings, each connected by two flexible connectors. The rings themselves consist of eight rhombuses. The struts have a thickness of t_{strut} = 120 μm. The two investigated stent designs only differ in terms of the local design of the strut widths. Stent$_{hom}$ exhibits homogeneous strut widths of w_{strut} 80 μm (figure 4.1b). Stent$_{het}$ has heterogeneous strut widths of w_{strut} = 108 μm at the outermost rings (red), strut widths of w_{strut} = 95 μm at the penultimate rings (blue) and strut widths of w_{strut} = 83 μm at the remaining rings (black) (figure 4.1c). Thus, the geometrical induced stiffness of stent$_{het}$ increases from the stent center to the stent ends, which is intended to cause an atypical expansion behavior of stent$_{het}$, i.e. without the development of an pronounced DB ratio.

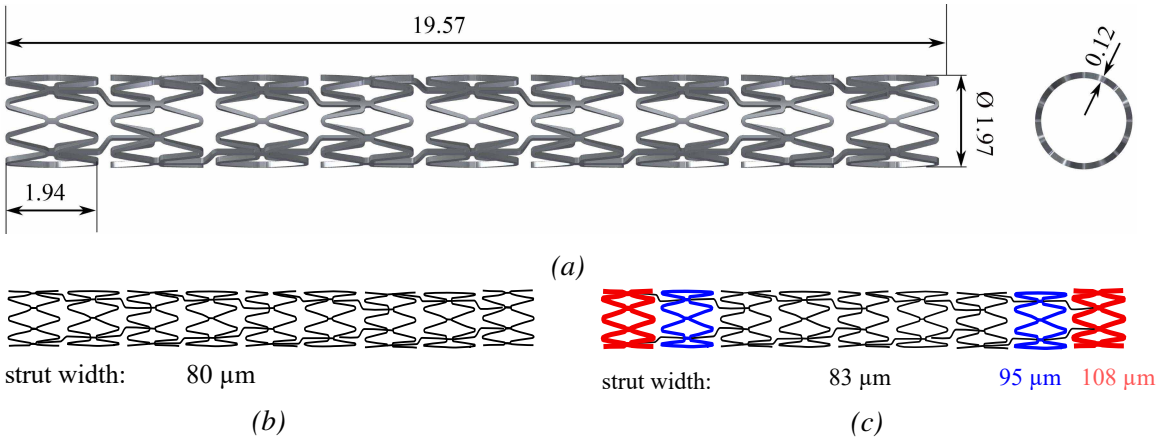

Figure 4.1: Investigated stent designs. (a) CAD model of the investigated stent designs including its basic dimensions given in mm. (b) Schematic illustration of stent$_{hom}$ with the homogeneous strut widths. (c) Schematic illustration of stent$_{het}$ exhibiting heterogeneous strut widths.

4.2 Computational framework

For numerical stent expansion analysis, two stent expansion approaches were considered: i) balloon-stent expansion and ii) displacement-controlled expansion. The balloon-stent expansion approach is intended to depict the transient stent expansion as close to reality as possible. The displacement-controlled expansion approach, is intended to offer a more computational

[1]The prototype stent ESPRIT V1 design and its modifications were taken from previous internal work of the Medical Devices Laboratory of the OTH Regensburg.

efficient way for evaluating the stress states of the stent during expansion. Prior to the actual expansion simulations, preliminary simulation steps, such as balloon folding and/or stent crimping, were required. These enable the consideration of pre-deformations and thus residual stresses in the stent or balloon, which in return improve the accuracy of the numerical predictions.

For the FEAs, the FE solver Abaqus/Explicit 2017[2] was used. Care has been taken to ensure that the ratio of kinetic to internal energy is kept below a critical value of $E_{KE}/E_I < 5$ - 10 % during most of the process. In this way the influence of inertial effects is negligible and the requirements for quasi-static simulation are fulfilled [47].

4.2.1 Simulation of balloon folding

The investigated balloon geometry was adopted from the Baroonda stent delivery system[3]. The basic dimension of the balloon and the catheter shaft are provided in figure 4.2. The balloon membrane consists of Grilamid L25. The elastic properties of the balloon were described by a Young's modulus of E = 1000 MPa and a Poisson ratio of ν = 0.1. The inelastic constitutive response of the balloon material was described by a von Mises plasticity model with isotropic hardening. Therefore, a flow curve was extracted from uniaxial tensile test data provided by the balloon manufacturer up to uniform elongation and extrapolated using Hollomon's power law equation (equation 2.27: $\sigma_{y,H} = K_H(\bar{\varepsilon}^{pl})^{n_H}$). Thus, the plastic material behavior of Grilamid L25 was described by a yield strength of σ_y = 30 MPa and the determined Hollomon parameters of K_H = 61.2 MPa and n_H = 0.12. The balloon was meshed by 170405 4-node quadrilateral M3D4 and 478 3-node triangle membrane elements M3D3 with an average element size of 0.037 mm (figure 4.3a). The catheter shaft was modeled as a rigid cylinder.

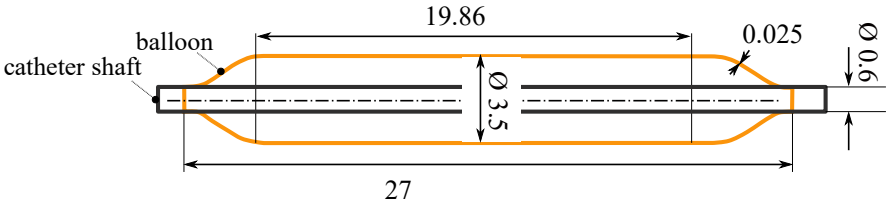

Figure 4.2: Basic dimensions of the semi-compliant Baroonda angioplasty balloon. All the dimensions are given in mm.

The balloon folding device[4] was implemented by means of the contact surfaces of the jaws, considering three folding (figure 4.3a) and ten pleating jaws (figure 4.3b). The jaws were modeled as rigid analytical surfaces. Reference points were defined at the pivot points of the jaws and connected to the respective jaws via a rigid body constraint (figure 4.4). Thus, the application of

[2] Abaqus (Dassault Systèmes, Vélizy-Villacoublay, France)
[3] Baroonda stent delivery system (SDS, 08BO-3520A, Bavaria Medizin Technologie GmbH, Wessling, Germany)
[4] Balloon folding device (MSI Machine Solution Flagstaff, US)

a rotating boundary condition u_{rot} at the reference point initiated the rotation of the respective jaw. For the balloon folding simulation, the balloon and the catheter were co-axially aligned at the center of the folding and pleating jaws (figure 4.3a). During the folding simulation, the balloon was fixed at the proximal end, while displacement in the axial direction was allowed at the distal end to enable balloon elongation. The rigid catheter was fixed to ensure kinematic constraint during the balloon folding simulation.

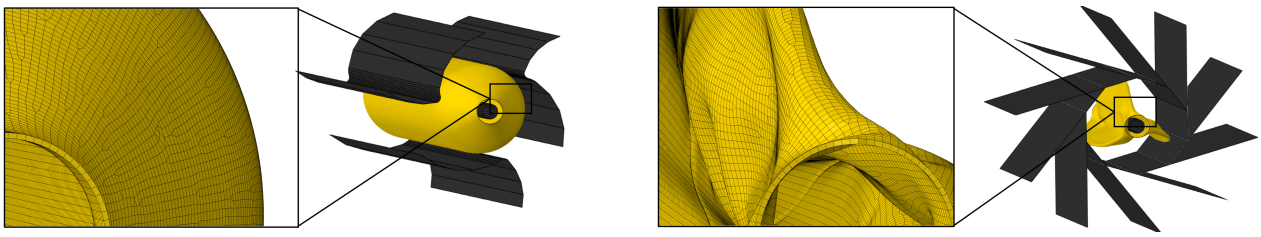

(a) (b)

Figure 4.3: Model set-up of the balloon folding process with magnified view of the mesh, adapted from Wiesent et al. [10]. (a) Initial balloon inside the folding jaws. (b) Folded balloon inside the pleating jaws.

Balloon folding was achieved in two steps. In the first step, the three folds were generated by applying a rotating boundary condition of u_{rot} = -4.58° at the reference points of the three folding jaws. Thereupon, a pressure of p = -0.1 MPa was applied to the inner surface of the balloon to create a vacuum inside the balloon before the folding jaws were retracted by the reversion of the previous applied rotating boundary condition (figure 4.4a). In the second step, the three folds were warped around the catheter shaft by applying a rotating boundary condition of u_{rot} = 1.1° at the reference points of the ten pleating jaws (figure 4.4b). Thereupon, the pleating jaws were retracted by reversion of the previous applied rotating boundary condition and the applied pressure at the inner surface of the balloon was removed. Contact between the jaws and the balloon, as well as balloon self-contact was invoked using the general contact algorithm (penalty method) within Abaqus/Explicit considering a friction coefficient of μ = 0.2.

4.2.2 Simulation of stent crimping

For the FEA of stent crimping, the CAD model of the investigated stent was imported into Abaqus and meshed with eight node linear brick elements with reduced integration and hourglass control (ABAQUS element type C3D8R). A mesh convergence study was performed, which showed that adequate results can be obtained with an element size of 0.03 mm within a reasonable computation time.

The stents consist of 316L. The elastic properties of the stent were described by a Young's modulus of E = 193 GPa and a Poisson ratio of ν = 0.3. The inelastic constitutive response of

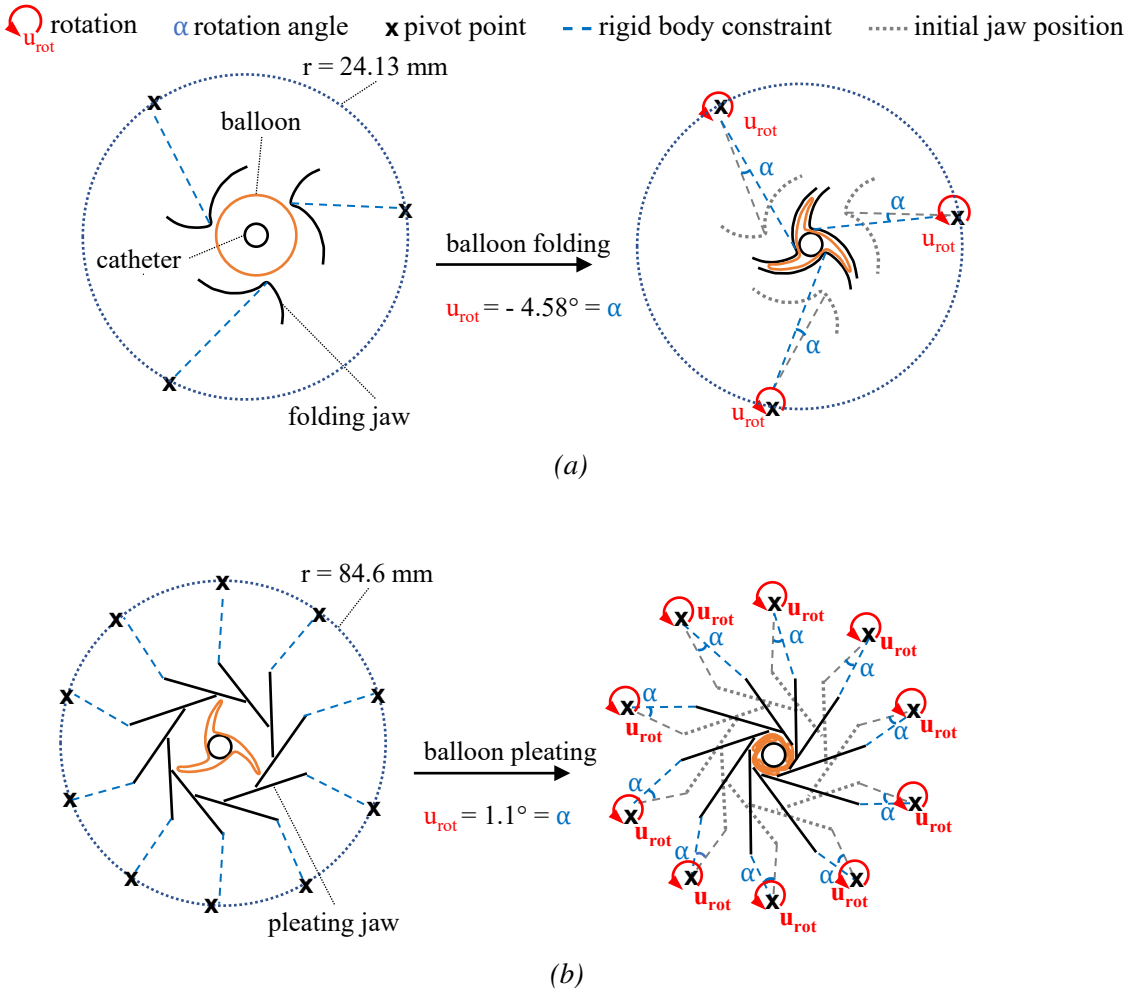

*Figure 4.4: Boundary condition during the balloon folding simulation, adapted from Wiesent et al. [10]. (a) Balloon folding by rotating the folding jaws by u_{rot} around their pivot point **x**, thus rotating the jaws by an angle α and generating three balloon folds. (b) Balloon pleating by rotating the pleating jaws by u_{rot} around their pivot point **x**, thus rotating the jaws by an angle α and warping the balloon folds around the catheter shaft.*

the 316L stents was described by a von Mises plasticity model with isotropic hardening. The plastic material properties of the 316L stents were determined from uniaxial tensile tests on tubes with a wall thickness of t = 120 μm, from which the later stents were cut. A flow curve was extracted from the uniaxial tensile test data up to uniform elongation and extrapolated using Hollomon's power law (equation 2.27: $\sigma_{y,H} = K_H(\bar{\varepsilon}^{pl})^{n_H}$). The plastic behavior of the stent was described by a yield strength of σ_y = 328 MPa and the determined Hollomon parameters of K_H = 1440 MPa and n_H = 0.39.

The folded balloon geometry and catheter shaft were imported from the previous balloon folding simulation, and co-axially aligned within the stent (figure 4.5). The crimping device was implemented based on the contact surfaces of the twelve crimping jaws. The crimping jaws

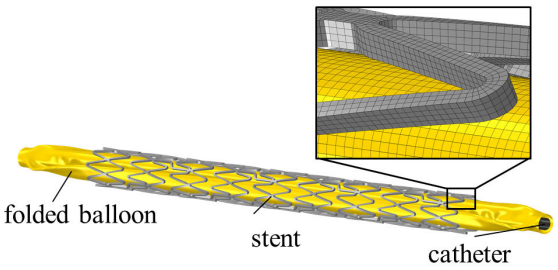

Figure 4.5: Stent placed over the balloon catheter with magnified view of mesh, adapted from Wiesent et al. [10].

were modeled as analytical surfaces. Reference points were defined at the pivot points of the crimping jaws and connected to the respective jaws via a rigid body constraint (figure 4.6). Thus, the application of a rotating boundary condition u_{rot} at the reference point initiates the rotation of the respective crimping jaw. For the crimping simulation, the balloon-stent catheter system was co-axially aligned within the crimping iris. Stent crimping was achieved by applying a rotating boundary condition of $u_{rot} = 0.464°$ at the reference points of the twelve crimping jaws, thus reducing the crimping iris to an inner diameter of $D = 1.17$ mm figure 4.6. Thereupon, the crimping jaws were retracted by the reversion of the previous applied rotating boundary condition ($u_{rot} =$ -0.464°) and the stent reached its final diameter after recoil.

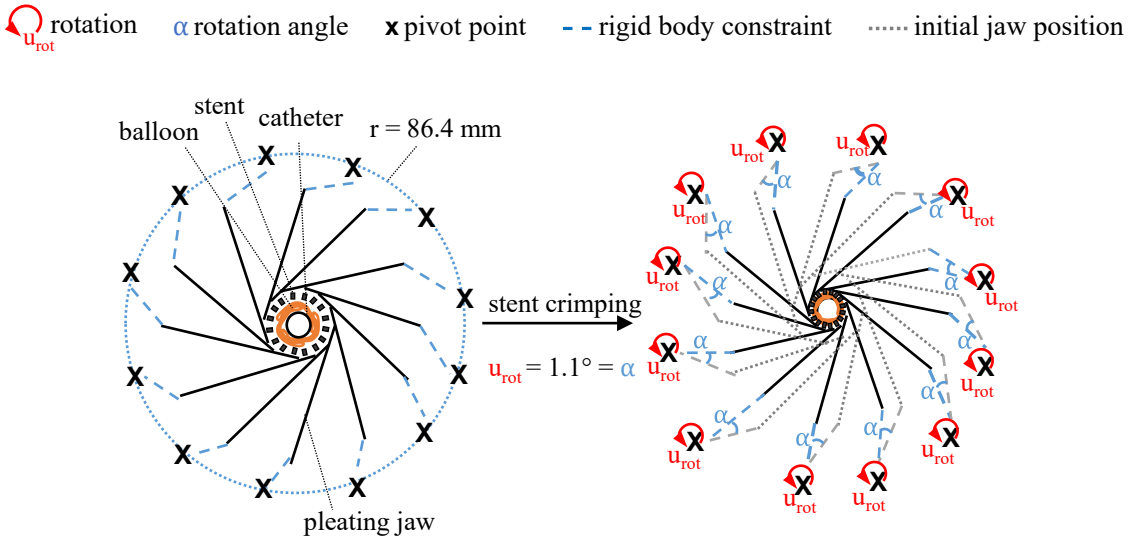

*Figure 4.6: Boundary condition during the stent crimping simulation by rotating the crimping jaws by u_{rot} around their pivot point **x**, thus rotating the jaws by an angle α and reducing the diameter of the stent, adapted from Wiesent et al. [10].*

Similar to the balloon folding simulation, the entire catheter was fixed and the balloon was fixed at the proximal end, while displacement in the axial direction was allowed at the distal end to enable balloon elongation. The rigid catheter was fixed to ensure kinematic constraint during the balloon folding simulation. Contact was invoked using the general contact algorithm (penalty method) within Abaqus/Explicit considering a friction coefficient of $\mu = 0.1$ (contact

pairings: crimping jaw-stent, stent self-contact) and μ = 0.2 (contact pairings: balloon-stent, balloon-catheter, balloon self-contact), respectively.

4.2.3 Simulation of stent expansion

Simulation of balloon-stent expansion

For the FEA of balloon-stent expansion, the stent crimped onto the balloon catheter, including the existing strain and stress states, was taken from the previous simulations. For the actual stent expansion analysis, a linearly increasing pressure up to p = 0.75 MPa was applied to the inner surface of the balloon. Once the final expansion diameter was reached, this pressure was reduced to a value of p = -0.1 MPa. In this way, the balloon was deflated to depict the elastic stent recoil. The boundary conditions at the balloon ends, as well as at the catheter shaft, remained identical to those of the balloon folding and stent crimping.

Simulation of displacement-controlled stent expansion

In the FEA of displacement-controlled stent expansion, stent expansion was achieved via a semi-rigid expansion cylinder. To create identical starting situations for both expansion approaches, the crimped stent, including the preexisting strain and stress states, was taken from the preliminary crimping simulation analogous to FEA of balloon-stent expansion. The expansion cylinder with an initial outer diameter of $D_{z,0}$= 1.0 mm was positioned co-axially within the stent. To increase the diameter of the expansion cylinder, a radial displacement of u_r = 1.25 mm was applied at all nodes of the cylinder aiming at a final outer diameter of the cylinder of $D_{z,exp}$= 3.5 mm, which is identical to the expanded balloon diameter. To depict the elastic stent recoil, the radial displacement boundary condition was reversed, thus restoring the original shape of the expansion cylinder. Contact between the stent and the expansion cylinder was realized with the general contact algorithm considering a friction coefficient of μ = 0.2 (stent-polyamide) analogous to FEA of balloon-stent expansion simulation.

Investigated stent expansion scenarios

To investigate the general applicability of the simulation models, different stent expansion scenarios were investigated and subsequently validated against experimental data. Thus, two different stent designs, two different stent placements on the balloon catheter, and two different expansion approaches were considered. With the displacement-controlled approach, no differences in transient expansion behavior between the two stent designs or decentralized stent positioning were expected due to the homogeneous expansion of the stents. Thus, FEA of the displacement-controlled expansion was only conducted for stent$_{hom}$. An overview of the investigated stent expansion scenarios is given in table 4.1.

Table 4.1: Overview of the various investigated computational stent scenarios.

Stent design	Strut width	Stent position*	Stent expansion approach	
stent_{hom}	homogeneous	central	balloon-stent expansion	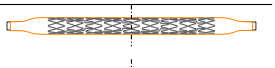
stent_{het}	heterogeneous	central	balloon-stent expansion	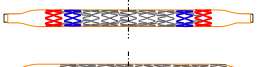
stent_{hom}	homogeneous	decentral	balloon-stent expansion	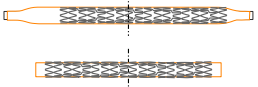
stent_{hom}	homogeneous	not applicable	displacement-controlled expansion	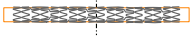

* with respect to the balloon catheter

4.3 Experimental framework

The experimental framework provided the basis for the validation of the numerical predictions regarding the balloon folding pattern, the shape of the crimped and expanded stent, and the course of transient stent expansion. Within this doctoral thesis, the experimental methods and results for stent testing were adopted from existing internal work of the Medical Devices Laboratory of the OTH Regensburg. Experimental stent testing was not part of this work and the results of experiential testing were exclusively used for the validation of the numerical simulations. Nevertheless, for the sake of completeness, a brief overview of the origin of experimental data is given below.

For the validation of the balloon folding pattern, a μ-CT [5] scan of a semi-compliant Baroonda angioplasty balloon was obtained. For validation of the stent simulations, a total of eight stents for both stent_{hom} and stent_{het} were reproducible crimped using an existing in-house crimping device and measured under the light microscope. A μ-CT scan of a crimped stent_{hom} was further obtained. Thereupon, the crimped stents were expanded and measured under the light microscope following a defined internal protocol. Stent expansion was performed using an existing in-house developed pump unit and recorded using a high-speed camera[6]. Based on the high-speed camera recordings, the DB ratio of each stent was determined based on an in-house MATLAB[7] script. For a more comprehensive validation of the stent expansion simulations, SEM[8] images of an expanded stent_{hom} were obtained that enabled the validation of the local onset of plastification processes within the stent material.

[5] μ-CT (Phönix v|tome|xs 240/180 research edition, GE Sensing & Inspection Technologies, Wunstorf, Germany)
[6] high-speed camera (HCC-1000, VDS® Vosskühler, Osnabrück, Deutschland)
[7] MATLAB (The MathWorks, Natick, Massachusetts, USA)
[8] SEM (1450 VP, Leo Elektronenmikroskopie GmbH, Oberkochen, Germany)

4.4 Results & Discussion

4.4.1 Balloon folding

The creation of the balloon folds is shown in figure 4.7 using sectional views of the balloon after each folding step. The predicted folded balloon has an overall length of l = 27.44 mm and a diameter of D = 1.5 mm.

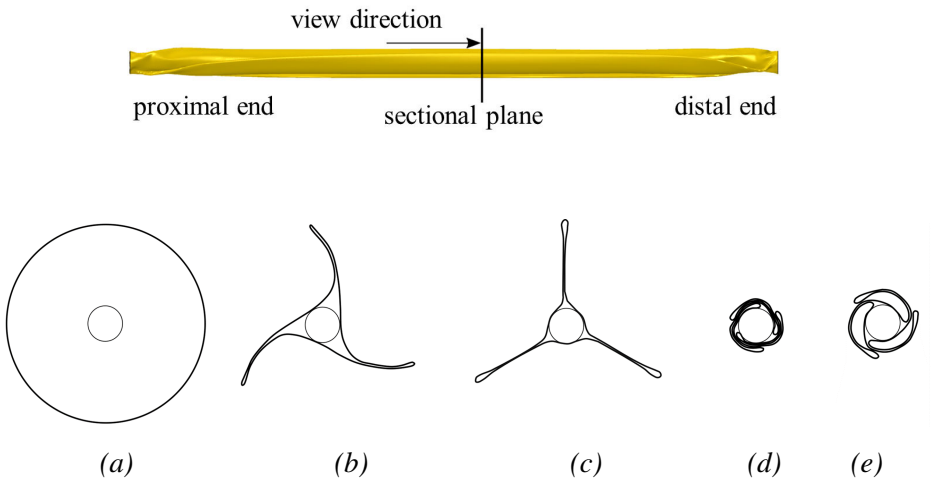

Figure 4.7: FEA of balloon folding represented by cross sectional images of the balloon after the various folding steps, adapted from Wiesent et al. [10]. Balloon cross section (a) in the initial state, (b) after rotating the folding jaws, (c) after the vacuum generation and retraction of the folding jaws, (d) after the rotating of the pleating and (e) after retraction of the pleating jaws also representing the final balloon folding pattern.

To validate the FEA of balloon folding, the predicted balloon shape was superimposed on a μ-CT scan of a folded Baroonda balloon catheter system (figure 4.8). The predicted and scanned balloon folding pattern were in good agreement, with only a slightly increased compression of the predicted balloon compared to the μ-CT scan. This could be due to relaxation processes of the balloon material or a decrease in vacuum with time in the real balloon, causing the balloon catheters to unfold slightly. However, these phenomena were not considered in the simulation. Since the balloon is compressed again during the FEA of stent crimping, this slight deviation is not expected to have a significant effect on the subsequent simulation steps.

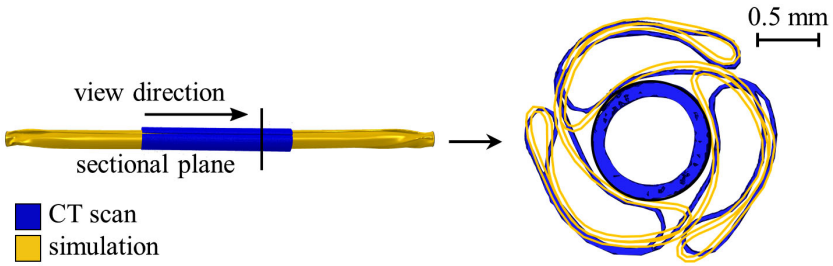

Figure 4.8: Validation of the balloon folding simulation by superimposition of the predicted folded balloon (yellow) with a μ-CT scan of a folded Baroonda balloon (blue), adapted from Wiesent et al. [10].

4.4.2 Stent crimping

With a maximum deviation of ≈ 1 %, the predicted dimensions of the stent after crimping were very consistent with the experimental measurements (table 4.2). To further validate the FEA of stent crimping, the predicted crimped stent$_{hom}$ was superimposed on a μ-CT scan of an experimentally crimped stent of the corresponding stent design (figure 4.9). The superimposition showed very good agreement with nearly congruent stent struts and connectors. The minor discrepancies in the superposition may be due to small statistical deviations in the original stent geometry or slight bending of the stent during fixation in the μ-CT.

Table 4.2: Comparison of the predicted mean stent dimension after crimping with the mean values of experimental measurements (specified with standard deviation).

	Stent$_{hom}$		Stent$_{het}$	
	Sim., mm	Exp., mm	Sim., mm	Exp., mm
stent diameter D_{crimp}	1.20	1.19 ± 0.02	1.20	1.19 ± 0.01
stent length l_{crimp}	19.70	19.75 ± 0.05	19.69	19.78 ± 0.16

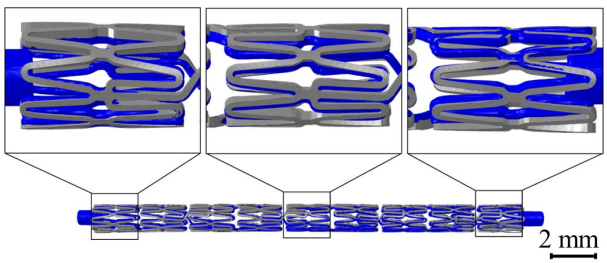

Figure 4.9: Validation of the stent crimping simulation by superimposition of the predicted stent$_{hom}$ (grey) with CT data (blue), adapted from Wiesent et al. [10].

4.4.3 Stent Expansion

In a first step, the FEAs of balloon-stent expansion and displacement-controlled stent expansion were evaluated with respect to their ability to predict the transient expansion behavior of the various stent scenarios by comparing the numerically predicted expansion behavior with high-speed camera images of the associated experimentally expanded stent (figure 4.10). The FEAs based on the balloon-stent expansion approach successfully predicted the transient stent expansion and shows good qualitative agreement with the high-speed camera images for all of the investigated stent expansion scenarios (figure 4.10a-c), whereas the displacement-controlled expansion did not predict the transient stent expansion behavior (figure 4.10d). For a more comprehensive evaluation of transient stent expansion, the predicted diameter development of the different stent expansion scenarios is evaluated in figure 4.11.

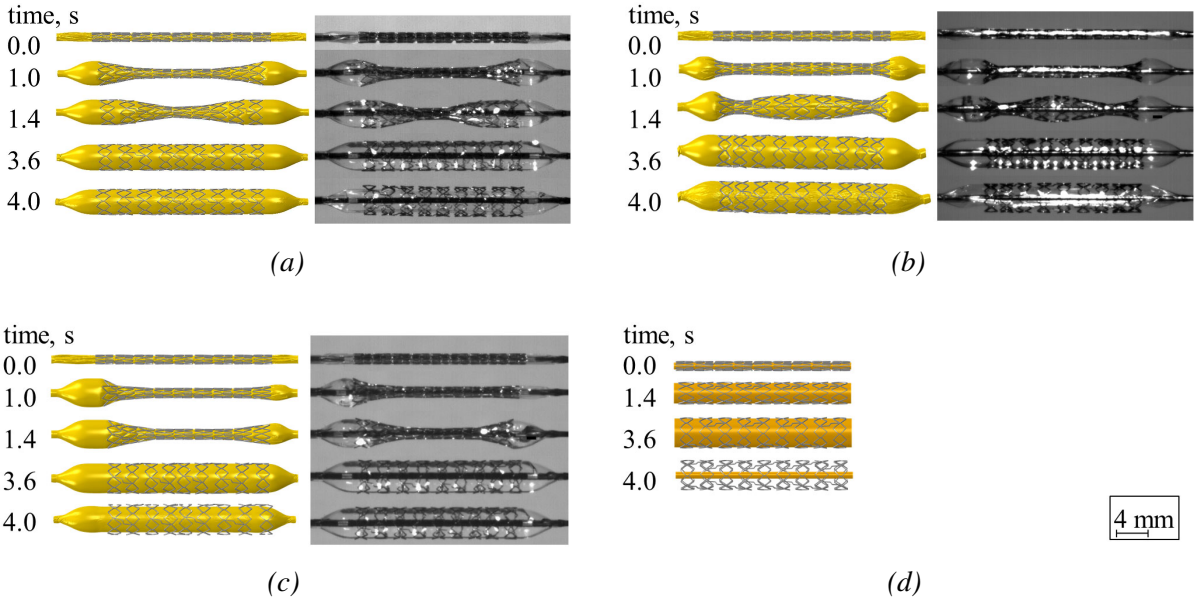

Figure 4.10: Comparison of the predicted stent expansion behavior (left) with high-speed recordings (right) adapted from Wiesent et al. [10]. Balloon-stent expansion of (a) $stent_{hom}$, (b) $stent_{het}$ and (c) $stent_{hom}$ decentrally positioned on the balloon catheter (offset Δ = 1 mm from the center towards the proximal balloon end). (d) Displacement-controlled expansion of $stent_{hom}$ failing to predict the transient stent expansion behavior. The specified time corresponds to the expansion time.

$Stent_{hom}$ is representative of a conventional stent design that exhibits typical expansion behavior with a pronounced DB ratio (figure 4.10a). Following an initial pressure accumulation at the free balloon ends, a distinct diameter increase occurred at both stent ends starting at an expansion time of t $\approx$ 0.5 s (figure 4.11a). At the central stent part, the distinct diameter increase initiated at an expansion time of $t \approx 1.4$ s. During the further nearly linear diameter increase, the gradient

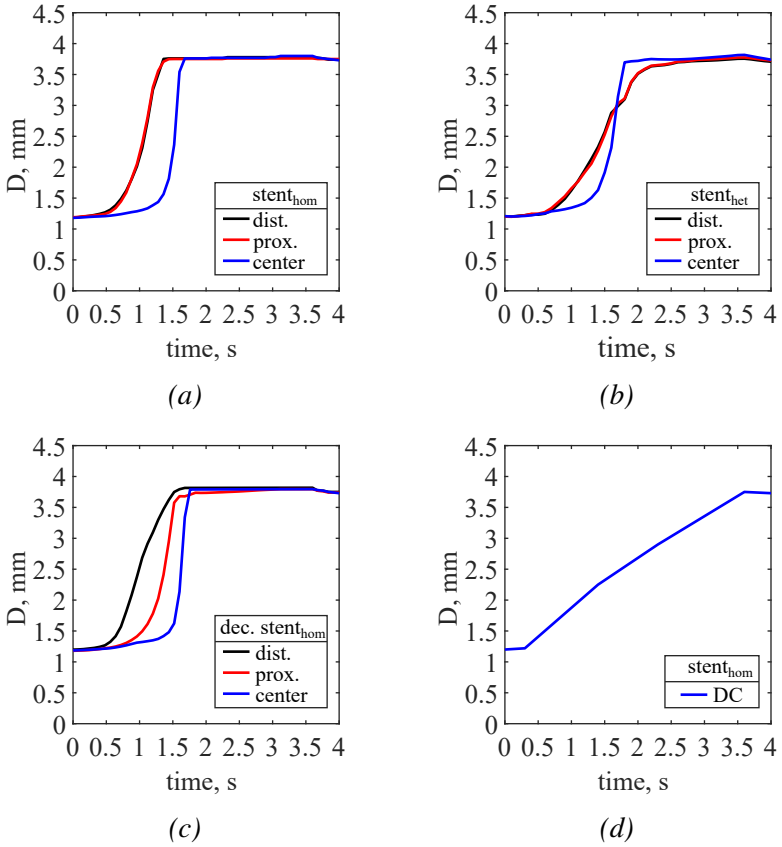

Figure 4.11: Predicted diameter evolution of the various stent expansion scenarios, adapted from Wiesent et al. [10]. Balloon-stent expansion of (a) $stent_{hom}$, (b) $stent_{het}$ and (c) $stent_{hom}$ decentrally positioned on the balloon catheter (offset 1 mm from the center towards the proximal balloon end). (d) Displacement-controlled (DC) expansion of $stent_{hom}$. For the balloon-stent expansion a distinction is made between the diameter progression of the distal (black), proximal (red) and central stent part (blue). Since the diameter development in the DC approach is homogeneous over the entire length of the stent, only the central diameter is illustrated. The specified time corresponds to the expansion time.

of stent diameter increase in the stent center ($\Delta D/dt$ = 6.9 mm/s) is slightly increased compared to the stent ends ($\Delta D/dt$ = 5.9 mm/s).

The $stent_{het}$ is representative of an unconventional stent design with an atypical, rather convex, expansion behavior (figure 4.10b). Following an initial pressure accumulation at the free balloon ends, a distinct diameter increase occurred at both stent ends at an expansion time of t $\approx$ 0.5 s, but with a lower gradient ($\Delta D/dt$ = 1.9 mm/s) compared to $stent_{hom}$ ($\Delta D/dt$ = 6.9 mm/s). This is attributed to the increased geometrically induced radial stiffness at the two outer rings of $stent_{het}$ (i.e., increased strut widths). The distinct diameter increase in the central part is analogous to $stent_{hom}$, thus starting at an expansion time of t $\approx$ 1.3 s, however, with a slightly reduced gradient ($stent_{het}$ center: $\Delta D/dt$ = 5.9 mm/s; $stent_{hom}$ center: $\Delta D/dt$ = 6.9 mm/s;). Compared to the gradient of diameter increase at the stent ends, the gradient at the stent center is about three times

higher, which finally causes the convex transient expansion of stent$_{het}$.

The FEA of balloon-stent expansion further accurately predicted the transient expansion behavior of the decentrally positioned stent$_{hom}$ which was associated with an asymmetric DB ratio (figure 4.10c). Unlike the previous described stent scenarios, initial pressure accumulation was not symmetrical, with increased pressure accumulation occurring at the longer free (i.e., distal) stent end. Thus, a distinct increase in stent diameter was initially observed at the distal stent end at an expansion time of t $\approx$ 0.5 s (figure 4.11c). In the proximal and central stent region, the increase in stent diameter is delayed at an expansion time of t $\approx$ 1.1 s and t $\approx$ 1.5 s, respectively. The gradients of stent diameter increase at the proximal and central part of the stent are comparable to those of the centrally placed stent$_{hom}$ (decentral stent position: $\Delta D/dt$ = 7.3 mm/s; central stent position: $\Delta D/dt$ = 6.9 mm/s), whereas the gradient at the distal stent end is significantly reduced ($\Delta D/dt$ = 2.5 mm/s).

The displacement-controlled approach did not predict the transient expansion behavior, which is not surprising given that stent expansion is achieved by expanding a semi-rigid cylinder (figure 4.10d). Thus, a linear increase in stent diameter was observed over the entire stent length of stent$_{hom}$ (figure 4.11d).

For further validation of the predicted transient stent expansion, the average $\overline{DB}$ ratio based on the DB ratio at the distal and proximal stent ends was obtained (equation 1.1, figure 4.12) and compared with experimental data, again showing good agreement (table 4.3). For stent$_{het}$ the average minimum $\overline{DB}$ ratio is given instead of the average maximum $\overline{DB}$ ratio, as it exhibits a rather convex transient expansion shape.

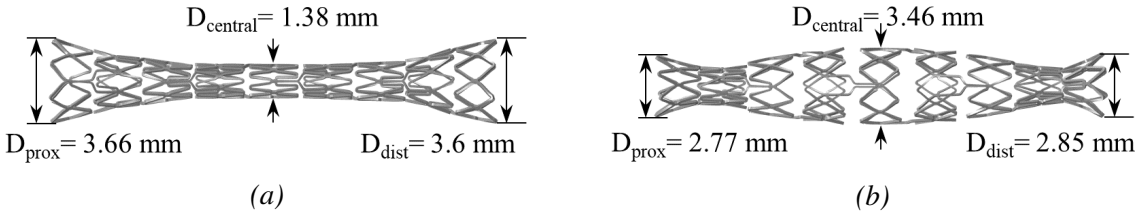

Figure 4.12: Determination of the predicted DB ratio obtained from the balloon-stent expansion approach for (a) stent$_{hom}$ and (b) stent$_{het}$, adapted from Wiesent et al. [10].

Table 4.3: Comparison of the numerical predicted $\overline{DB}$ ratio with the experimental determined average $\overline{DB}$ (specified with standard deviation) ratio of the investigated stents.

	Stent$_{hom}$		Stent$_{het}$	
	Sim.	Exp.	Sim.	Exp.
$\overline{DB}$ ratio	0.62	0.62 $\pm$ 0.02	-0.19	-0.21 $\pm$ 0.04

After assessing the transient expansion behavior, the FEA of balloon-stent expansion and displacement-controlled stent expansion were evaluated in terms of their ability to predict the expanded stent shape before and after recoil. The numerical predictions were in good agreement with the experimental measurements in terms of stent diameters and lengths in the expanded state (D_{expand}, l_{expand}) and also after recoil (D_{recoil}, l_{recoil}) for both stent expansion approaches (table 4.4). The deviation between the numerical predictions and the experimental measurements are limited to a maximum error of ≈ 0.5 to 2.3%. It can be concluded that both, the balloon-stent expansion approach and the displacement-controlled expansion approach are capable of predicting the final expanded stent shape.

Table 4.4: Comparison of the predicted stent diameter D and length l with experimental measurements. Stent dimensions are determined at maximum balloon expansion (index: expand) and after elastic recoil/balloon deflation (index: RC). The experimental measurements are given as mean value and standard deviation.

	Stent$_{hom}$		Stent$_{het}$		Stent$_{hom}$	
	Sim., mm (balloon*)	Exp., mm	Sim., mm (balloon*)	Exp., mm	Sim., mm (DC**)	Exp., mm
D_{expand}	3.80	3.78 ± 0.03	3.77	3.75 ± 0.07	3.77	3.78 ± 0.03
l_{expand}	18.0	18.35 ± 0.13	18.76	19.10 ± 0.14	18.77	18.35 ± 0.13
D_{RC}	3.73	3.71 ± 0.05	3.71	3.70 ± 0.07	3.67	3.71 ± 0.05
l_{RC}	18.20	18.54 ± 0.13	18.65	19.02 ± 0.16	18.78	18.54 ± 0.13

* balloon-stent expansion approach

** displacement-controlled expansion approach

With a maximum error of < 2 %, the largest deviation between the numerical prediction and the experimental measurements occurred for the prediction of the expanded stent length. For the FEAs of balloon-stent expansion, this is possibly due to the different balloon adhesion in simulation and reality. In reality, the balloon is locally compressed during stent crimping, which increases adhesion. Thus, during initial stent expansion, the stent has a higher longitudinal resistance to the wedge effect arising from the dilation of the free balloon ends and may therefore be less compressed longitudinally in reality. Within the FEAs of balloon-stent expansion, friction was accounted for by a static friction, which can only partially represent this effect. However, by implementing a dynamic friction coefficient that incorporates, e.g., the velocity of the relative motion or the stent surface condition, this effect could be more accurately considered [20]. For the displacement-controlled expansion approach, the deviation in predicted stent length might further be due to the simplified cylindrical expansion which does not account for any longitudinal compression. Thus, stent foreshortening is purely due to radial displacement of the stent, resulting in radial elongation and longitudinal compression of the stent struts. Local compression and elongation due to the evolution of DB ratio during stent expansion are not

considered, which in turn could cause the slightly increased predicted stent length.

After assessing the expanded stent shapes, the FEA of balloon-stent expansion and displacement-controlled stent expansion were evaluated with respect to the predicted stress distribution within the stent. In general, the stress distribution is similar for all investigated stents, with the highest stresses occurring in the region of the radii of the stent struts or the transitions between two stent rhombuses. Displacement-controlled expansion of $stent_{hom}$ resulted in slightly lower stresses than balloon-stent expansion of $stent_{hom}$, possibly due to the slightly smaller predicted expanded stent diameter. Compared with the expanded $stent_{hom}$, slightly increased stresses are observed within the last ring of the $stent_{het}$, possibly due to increased geometrically induced stiffness resulting from the increased strut width there.

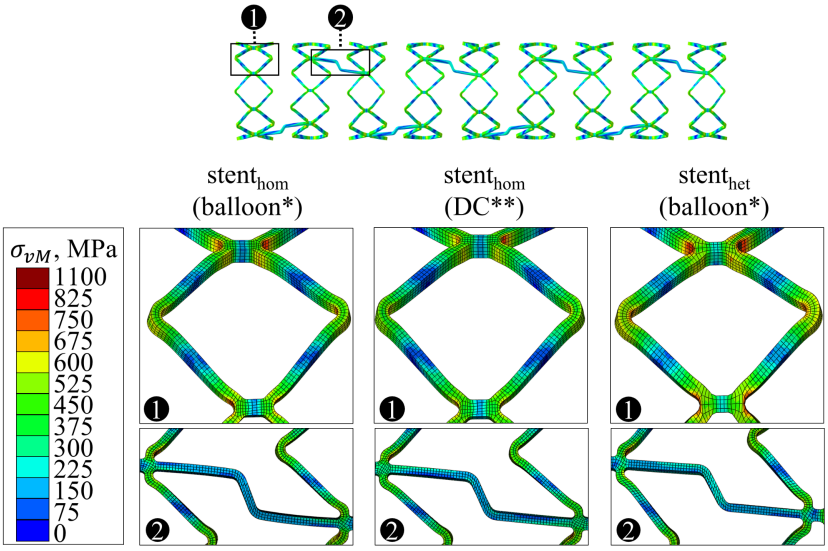

Figure 4.13: Contour plots of the von Mises stress σ_{vM} distribution of the various expanded stents, adapted from Wiesent et al. [10]. From left to right: balloon-stent expansion of $stent_{hom}$, displacement-controlled expansion of $stent_{hom}$, and balloon-stent expansion of $stent_{hom}$ with magnified view of a rhombus and connectors.

Finally, the plastic equivalent strain distribution of $stent_{hom}$ obtained from the FEA of balloon-stent expansion was compared with SEM images of an expanded $stent_{hom}$ (figure 4.14). This comparison allows a qualitative assessment of the occurrence of local flow processes and thus the plastification of the stent material. In regions of low stress/deformation ($\sigma < \sigma_{yield} = 328$ MPa) a smooth surface was observed in the SEM images, as no plastic deformation occurs there. This observation is consistent with numerical predictions, with little or no equivalent plastic strain evident in these regions. In the regions of higher stress/deformation ($\sigma > \sigma_{yield} = 328$ MPa), a wavy surface was observed in the SEM images, as local flow processes initiate, and plastic deformation occurs. This observation was also consistent with the numerical predictions, with increasing plastic strain evident in these regions.

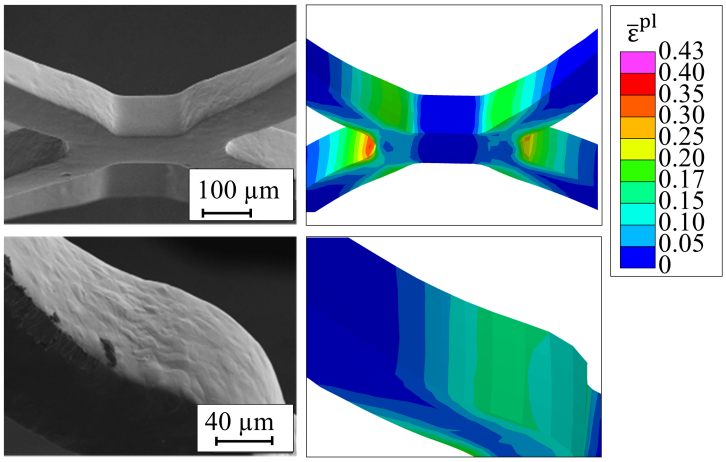

Figure 4.14: Comparison of the contour plot of the equivalent plastic strain $\bar{\varepsilon}^{pl}$ distribution of stent$_{hom}$ (right) with SEM images of an expanded stent$_{hom}$ (left), adapted from Wiesent et al. [10].

4.4.4 Limitations and Remarks

In this chapter, two numerical stent expansion approaches were presented and extensively validated both qualitatively and quantitatively using experimental data. It was found that the balloon-stent expansion approach accurately predicts the transient expansion behavior and the final deformation and stress states of the expanded stent, whereas the displacement-controlled stent expansion approach accurately predicts only the final deformation and stress states of the expanded stent. Nevertheless, there are some modeling assumptions in this work that merit further discussion. These mainly concern the stent geometry, material and contact modeling, balloon deployment strategy, and the pure analysis of free stent expansion.

The investigated stent models were based on statistical measurements of the respective real stent geometry. Direct reconstruction from CT data was not considered, and the investigated stent models are therefore to be regarded as statistically representative models. For conventionally manufactured laser cut stents, no strongly pronounced process-related irregularities, such as local notches, wavy strut areas, are to be expected, which justifies this approach for conventional stents.

To describe the plastic material behavior of the stents, a von Mises plasticity model with isotropic hardening was derived from quasi-static uniaxial tensile test on a stent blank (small tube). The influence of the strain rate on the material behavior of the stents was neglected, which may cause an underestimation of the yield stress of the stent material. Maximum strain rates of $\dot{\varepsilon} \approx 0.5$ were observed during stent expansion. Experimental studies in literature have found that mechanical behavior of 316L at this strain rate is comparable to the quasi-static state [118], thus justifying the assumption of quasi-static material behavior. Furthermore, kinematic strain

hardening and thus the Bauschinger effect was not considered within the stent material model. The Bauschinger effect causes a decrease in the yield strength of polycrystalline metals and thus a working softening after successive loading in opposite directions. During stent crimping, the stent material is subjected to local tensile and compression stresses, which then reverse sign as the stent expands. Thus, work softening due to the Bauschinger effect may reduce the overall resistance of the stent to balloon expansion. However, as stent expansion is mainly influenced by the geometrically induced stiffness of the stent topology (e.g., shape of the stent unit cell, strut cross section), the Bauschinger effect was expected to have a negligible effect on the stent expansion behavior.

The implementation of the balloon expansion by imposing a linear increasing pressure at the inner balloon surface represents another limitation of the presented stent FEAs. In reality, balloon expansion is achieved by injecting a fluid into the balloon catheter. This may cause local differences in the pressurization of the balloon catheter. For a more realistic implementation of balloon-stent expansion, a complex fluid-structure interaction (FSI) simulation must be conducted. However, theses simulations are very complex and computational-intensive. A major challenge is posed by the large changes in the volume of the balloon lumen, which places high demands on the adaptivity of the mesh. The presented balloon-stent expansion approach successfully predicted the transient stent expansion of symmetric stent designs. However, for asymmetric stent designs, this approach may have its limitations. Therefore, in subsequent studies, the presented balloon-stent expansion approach should be compared with a detailed balloon-stent expansion based on a FSI simulation

Furthermore, within this work only free stent expansion was considered neglecting stent-artery interaction. Even though, it could be shown that even small changes in the stent design can significantly alter the stent expansion behavior, only minor conclusions on the stent-artery interaction can be drawn. It can be assumed that a lower DB ratio, and thus a more homogeneous stent expansion, reduces the stent-induced arterial stresses. Nevertheless, this assumption needs to be substantiated by extensive analyses.

4.5 Conclusions

In this chapter, FEAs of stent expansion was conducted considering both the balloon-stent expansion approach and the displacement-controlled stent expansion approach. Moreover, different stent expansion scenarios (two stent designs, two stent positioning) were investigated and subsequently validated against experimental data. The balloon-stent expansion approach included the simulation of balloon folding, stent crimping, and balloon-stent expansion. The

displacement-controlled expansion approach included a crimped stent, as well as homogeneous stent expansion using semi-rigid cylinders. The following conclusions are drawn:

- FEAs of balloon folding and stent crimping showed good agreement with the experimental data regarding the final folded balloon geometry and the crimped stent geometry, respectively.
- FEA of balloon-stent expansion allowed an accurate prediction of the transient stent expansion behavior and of the final expanded stent geometry. Moreover, the accurate prediction of the expansion behavior of two different stent designs with typical and atypical stent expansion behavior, as well as the prediction of the expansion behavior of a stent positioned decentrally on the balloon catheter, demonstrated the universal applicability of balloon-stent expansion approach for transient stent expansion analysis.
- FEA of displacement-controlled stent expansion approach was not capable of predicting the transient stent expansion behavior, but enabled an accurate and computational-efficient prediction of the final expanded stent shape and the associated deformation and stress states.
- For numerical stent analysis, the balloon-stent and the displacement-controlled expansion approaches should be efficiently chosen depending on the focus of the study: If the focus is on transient stent expansion analysis, the use of the balloon-stent expansion approach is essential. If the focus is on the analysis/optimization of the deformation and stress states, the use of the displacement-controlled stent expansion approach is recommended for efficiency reasons.

5 Experimental analysis of L-PBF 316L tensile specimens

In literature, various studies on the mechanical behavior of L-PBF 316L in the as-built condition and after heat treatment have been conducted [68, 70, 73, 74]. However, these studies are mainly focused on investigations on standard tensile specimens with a thickness of $t > 1.0$ mm. Like L-PBF lattice structures, coronary stents exhibit strut diameter in the micrometer range. The particular mechanical properties of individual filigree struts have hardly been investigated so far, since most research on L-PBF-lattices focuses on the global mechanical behavior of the lattice structures [24, 34, 36, 37]. Few studies concerned the determination of mechanical properties of individual L-PBF struts, suggesting lower strength of individual L-PBF struts compared to the bulk material [119, 120]. The determination of mechanical properties of single L-PBF struts is challenging, both in terms of manufacturability, experimental methods and reliability of the obtained results. During L-PBF, single struts exhibit high risk of failure due to the occurrence of e.g., residual stresses, swelling or damage of the structures during recoating [121]. To ensure the stability of L-PBF parts during the build process, a maximum height to diameter aspect ratio of 8:1 is recommended [122], e.g. a maximum strut length of only $l < 1.0$ mm for a stent strut diameter of $D \approx 0.1$ mm. Besides the limited strut height, experimental testing poses a major challenge, e.g. in terms of strut clamping, strut buckling before/during the uniaxial tensile tests, determination of the strut cross section. Filigree L-PBF specimen are also more susceptible to unfavorably distributions of pores and surface defect due to the increased surface-to-volume ratio [121]. In summary, the determination of the mechanical behavior of miniaturized L-PBF tensile specimens/struts may be biased, and therefore their transferability to the mechanical behavior of individual L-PBF stent struts must be critically considered and evaluated.

Thus, in this work, testing of single L-PBF 316L struts was omitted. Rather, in a first step, the influence of the specimen size on the mechanical behavior of L-PBF 316L was analyzed on standard tensile specimens, which ensured reliable preparation of the specimens as well as their experimental analysis. Therefore, a comprehensive study on the influence of specimen thickness on the mechanical properties and microstructure of L-PBF 316L is presented, analyzing not only the influence of specimen thickness but also the influence of specimen orientation angle and post-processing conditions (i.e., as built, heat treated). To ensure the comparability of the

results of the experimental analysis, the investigated L-PBF 316L specimen were built from the same volume. Thus, variations in the microstructure and mechanical properties of the specimens due to small differences in the process parameters between individual build jobs can be excluded. Some contents of the experimental methods and results of the tensile specimens in the as-built condition have previously been published in Wiesent et al. [123] and were supplemented with further findings in the course of this work. Based on the findings of this work, a principle tendency of the transferability of the mechanical properties of L-PBF bulk material specimens to the mechanical properties of L-PBF stents was determined.

5.1 Experimental procedure

5.1.1 L-PBF specimen generation and post-processing

Specimen geometry

The geometry of the investigated tensile specimens was in accordance with DIN 50125 form E [124], with its basic dimension illustrated in figure 5.1a. To determine the effect of specimen orientation angle Θ and specimen t thickness on the mechanical properties of L-PBF tensile specimens, these two parameters were varied while the remaining dimensions of the specimen were kept constant. Thus, specimen orientation angles of $\Theta = 0°$, 30°, 45° and 90° to BD, were considered, respectively (figure 5.1b). The specimen orientation angle Θ is defined as the angle between the longitudinal specimen axis and BD. For each specimen orientation angle, specimens with a thickness of $t = 0.5$ mm, 0.75 mm, 1.0 mm, 1.5 mm, and 2.0 mm were analyzed. For the specimen orientation angles of $\Theta = 0°$ and $\Theta = 90°$, additional specimen thicknesses of $t = 2.5$ mm, 3.0 mm, 3.5 mm, 4.5 mm and 5.0 mm were evaluated to gain further insights into the L-PBF 316L bulk material behavior. For each specimen configuration, three specimens were built.

Laser Powder bed fusion

Within the L-PBF process, gas-atomized 316L powder[1] with a particle size of $D_{powder} \approx 15$ - 45 μm was used. The chemical composition of the 316L powder is provided in table 5.1.

Table 5.1: Chemical composition of the 316L powder (wt.-%).

C	Cr	Cu	Mn	Mo	N	Ni	O_2	P	S	Si	Fe
0.019	17.80	0.1	1.12	2.32	0.10	12.65	0.02	0.009	0.005	0.64	balance

The L-PBF tensile specimens were built in a single batch using a SLM 250 machine[2]. The SLM 250 machine was equipped with an Ytterbium (Yb)-fibre-laser with a maximum power

[1] LPW Technology Ltd., Rundcorn, UK
[2] SLM Solutions Group AG, Lübeck, Germany

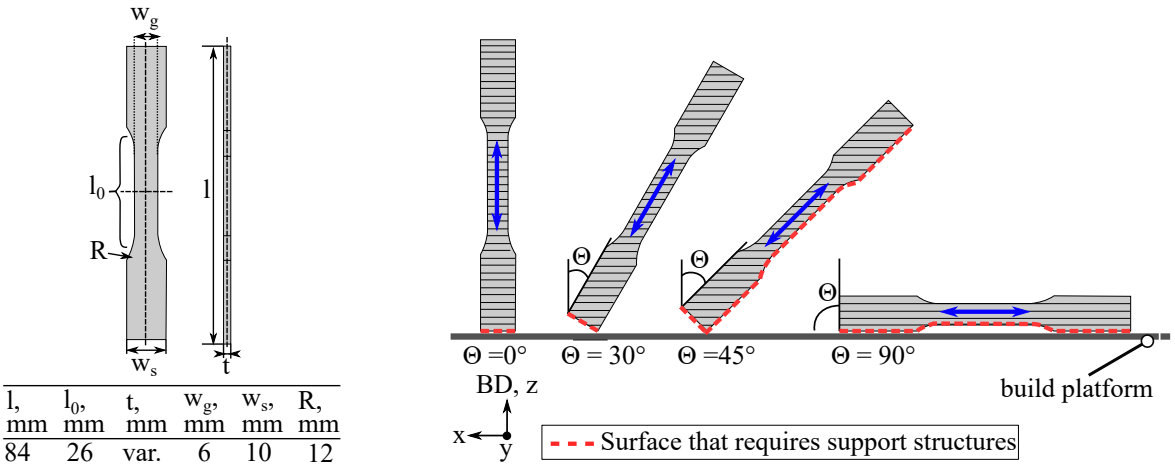

l, mm	l_0, mm	t, mm	w_g, mm	w_s, mm	R, mm
84	26	var.	6	10	12

(a) *(b)*

Figure 5.1: Investigated tensile specimens, adapted from Wiesent et al. [123]. (a) Dimensions of the tensile specimens with the specimen length l, the gauge length l_0, the gauge width w_g, the width of the grip section w_s, the specimen thickness t and the radius R. (b) Specimen orientation angles Θ of the investigated tensile specimens. The specimen orientation angle Θ is defined as the angle between the longitudinal specimen axis and the build direction (BD)). The horizontal lines within the specimens represent the individual build layers. The loading direction is indicated by the blue arrows. Surfaces that require support structures are highlighted with red dashed lines.

of $P = 400$ W. At a laser power of $P = 400$ W (100 % of maximum power) the laser spot diameter was $D_{laser} = 150$ µm. The contour-hatch strategy was used (figure 5.3). For the hatch scan (in-fill), a stripe filling scanning pattern with bidirectional scanning direction was applied with a base offset of $\Delta d = 150$ µm from the part contour. The contour scan was composed of a post-contour scan (outer part contour) and a pre-contour scan (connection between the outer contour and the hatch fill). After each layer the hatch pattern was rotated by an angle of $\alpha = 83°$. Furthermore, platform preheating with a temperature of $T = 100$ °C was applied. The applied process parameters as well as the energy input E of the applied scanning strategies, i.e. the line energy E_L of the contour scan and the area energy E_A of the hatch scan are summarized in table 5.2.

Table 5.2: L-PBF processing parameters used in the present work.

Scan type	Laser power P	Scan speed v	Layer thickness t	Hatch spacing h	Energy E
In-fill/ hatch	350 W	700 mm/s	50 µm	80 µm	6.25 J/mm^{2*}
Contour	100 W	350 mm/s	50 µm	–	3.5 J/mm**

* area energy: $E_A = \frac{P}{v \cdot h}$; ** line energy: $E_L = \frac{P}{v}$.

During pre-processing, support structures were selectively attached to the intended L-PBF tensile specimen to ensure their stability during the L-PBF process (figure 5.1b, figure 5.2). For

specimens with an orientation angle of $\Theta = 0°$ and $\Theta = 30°$ support structures were considered at the specimen shoulder. For specimens with an orientation angle of $\Theta = 45°$ and $\Theta = 90°$, support structures were attached along the entire length of the downward-facing side of the longitudinal specimen axis. After completion, the tensile specimens were cut from the build platform and the support structures were removed by grinding. Other than that, no further machining was applied to the L-PBF tensile specimens.

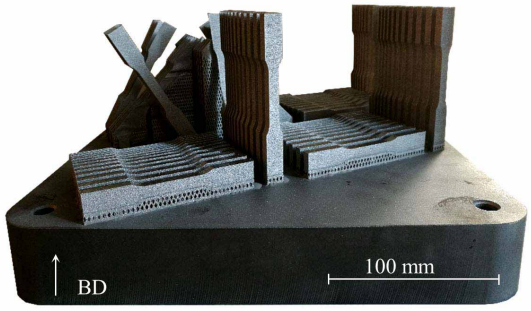

Figure 5.2: As-built 316L L-PBF tensile specimens on the build platform.

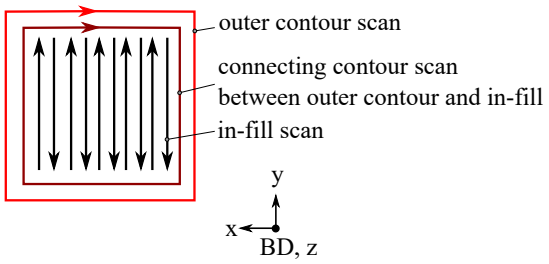

Figure 5.3: Applied contour-hatch scanning strategy of the L-PBF process.

Heat treatment

For each specimen configuration, two specimens were investigated in the as-built condition. The remaining tensile specimens of the build job, i.e., one specimen for each specimen configuration, were subjected to heat treatment at a temperature of $T = 1050$ °C for a duration of $t_H = 60$ min and subsequently cooled within the oven. This homogenization heat treatment was considered to be suitable for stent application by increasing the material strength and ductility of L-PBF 316L. Thus, the applied heat treatment was aimed at homogenization of the microstructure, i.e., reduction of residual stresses, dissolution of micro-segregations (e.g., melt pools, cellular microstructure), while maintaining the fine-grained microstructure and high strength characteristic of L-PBF metals. Complete recrystallization, i.e., heat treatment at a temperature of $T > 1200$ °C, was therefore deliberately not attempted, since this is associated with grain coarsening and hence a reduction in strength as per the Hall-Petch ratio [40, 66, 83].

5.1.2 Metallographic analysis

To evaluate the influence of specimen thickness on the microstructure, metallographic section of the tensile specimens with a thickness of $t = 0.5$ mm and $t = 2.0$ mm were analyzed, respectively. For this purpose, three cross sections were taken from each of the three specimen planes of the unloaded portion of the tensile specimens. Thereupon, these cross sections were embedded

perpendicular and parallel to BD in hot mounting resin, respectively, ground, mirror polished and etched in hot V2A etchant. Subsequently, the thus prepared metallographic sections were analyzed under the light microscope according to standard procedures.

5.1.3 Uniaxial tensile tests

Uniaxial tensile tests at room temperature were conducted using a universal testing machine[3]. The specimens were loaded at a constant deformation rate of $v = 1$ mm/min. Strain was obtained using an extensometer with an initial gauge length of $l_0 = 25$ mm. For each specimen configuration, two tensile specimens were tested in the as-built and one in the heat treated condition. The test matrix is provided in table 5.3. The thickness and width of the specimens were determined using a caliper, with the mean value of three measurements determined in each case.

Table 5.3: Test matrix of the uniaxial tensile tests considering L-PBF 316L tensile specimen with various thickness t, orientation angle Θ and post-processing condition (as-built, heat treated).

	As-built				Heat treated			
	Specimen orientation angle Θ, °				Specimen orientation angle Θ, °			
Specimen thickness t, mm	0	30	45	90	0	30	45	90
0.5	2	2	1*	2	1	1	1	1
0.75	1*	2	1	2	1	–**	–**	–**
1.0	1	2	1*	2	1	1	1	1
1.5	2	2	1*	2	1	1	–**	–**
2.0	2	2	1*	2	1	1	1	1
2.5	2	–	–	2	1	–	–	1
3.0	2	–	–	2	1	–	–	–**
3.5	2	–	–	2	1	–	–	–**
4.0	2	–	–	2	1	–	–	1
5.0	2	–	–	2	1	–	–	1

* one specimen was damaged during the build process or the removal of the support structure. Thus, only one tensile specimen was tested for the respective specimen configuration.
** all specimens were damaged during the build process or the removal of the support structure. Thus, no tensile specimen was available for the analysis of the heat treated tensile specimen configuration.

5.2 Results and discussion

5.2.1 Metallographic analysis

3D visualization of the microstructure of representative L-PBF tensile specimens in the as-built and heat treated condition are provided in figure 5.4. Furthermore, metallographic sections in the

[3]Hegewald & Peschke Mess- und Prüftechnik GmbH, Nossen Germany

as-built condition are shown in figure 5.5.

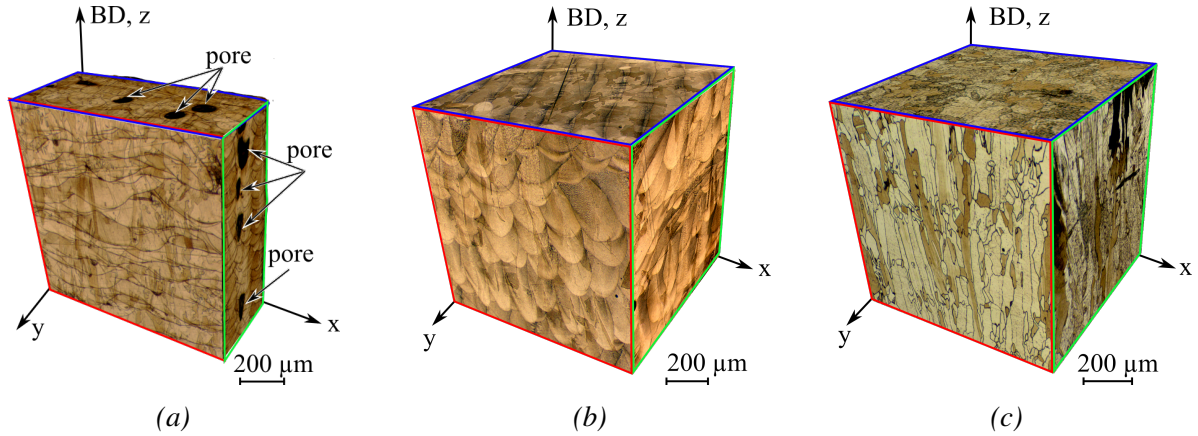

Figure 5.4: 3D visualization of the microstructure of L-PBF 316L of a tensile specimen with (a) a thickness of t = 0.5 mm in the as-built condition, (b) a thickness of t = 2.0 mm in the as-built condition and (c) a thickness of t = 2.0 mm after heat treatment at a temperature of T = 1050 °C for 60 min, adapted from Wiesent et al. [123] and supplemented.

Microstructure of L-PBF 316L in the as-built condition

Figure 5.4a, b shows the the microstructure of the L-PBF 316L tensile specimen with a thickness of t = 0.5 mm and t = 2.0 mm in the as-built condition. The strongly textured microstructure is typical of as-built L-PBF metals and is mainly associated with rapid solidification of the melt pools in combination with directional heat removal [60]. Thus, the microstructure is characterized by overlapping melt pools, elongated grains commonly aligned with BD, pores and a fine cellular substructure.

The arc-shaped melt pools and melt traces are associated with the Gaussian energy distribution of the laser. The periodical alignment of the melt pools results from the track and layer wise melting of metal powder as well as partial remelting of previously solidified layers which are penetrated by newly formed the melt pools. The respective shape of the melt pools in the metallographic sections depends on the current scan direction with respect to the investigated cross section. During the build process, the scanning pattern was rotated by an angle of $\alpha = 83°$ after each layer. Thus, if the scanning direction was approximately perpendicular to the investigated cross section, almost semicircular melt pools are visible. Otherwise, more elliptical melt pools are observed. In the central part of the specimen, the melt pools have a width of $w_{MP} > 130$ - 150 μm. In the contour region, smaller melt pools with a width of $w_{MP} \approx 90$ - 100 μm are evident (figure 5.5c). The difference in melt pool size between the central and contour regions can be attributed to differences in process parameters and thus energy input between the hatch and contour scans. Thus, Ocylok et al. [125] observed an increase in melt pool size with increasing energy input. Derived from the *Rosenthal equation* [126], Tang et al. [127] approximated

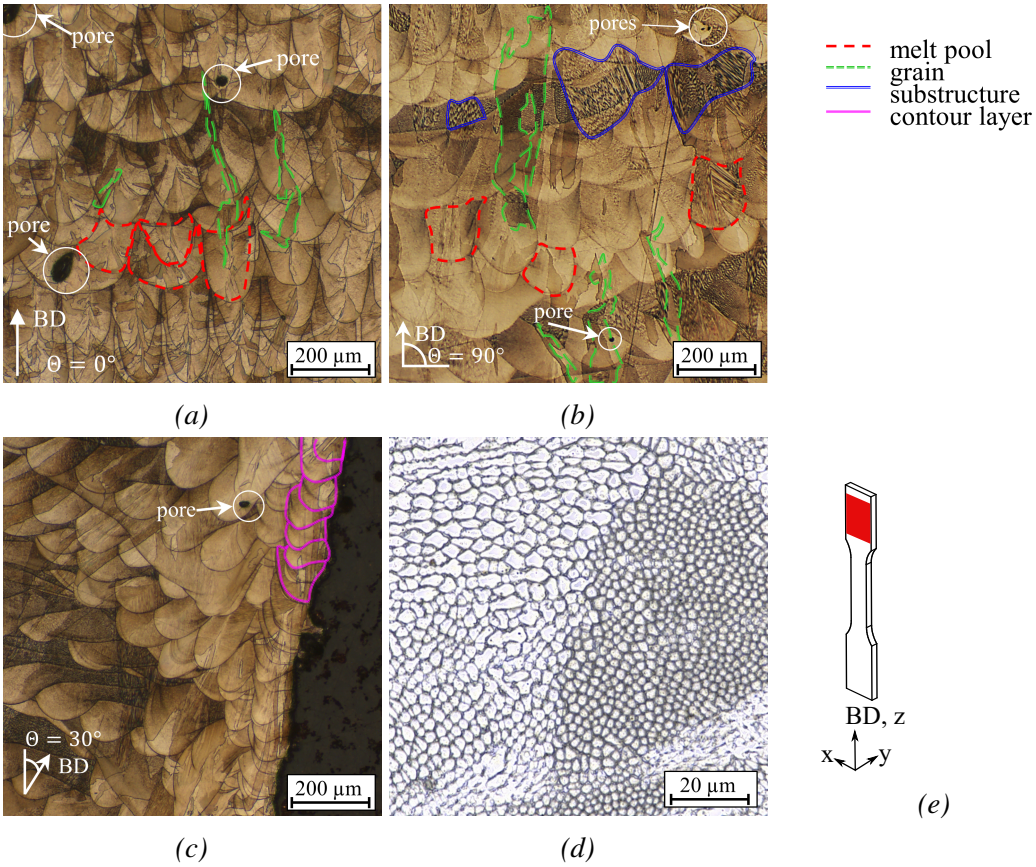

Figure 5.5: Metallographic sections of the L-PBF tensile specimens (zx-plane) in the as-built condition, adapted from [123]. Specimen orientation angle of (a) $\Theta = 0°$, (b) $\Theta = 90°$ and (c) $\Theta = 30°$. (d) Fine intragranular substructure. (e) Location of the metallographic sections (red square) with respect to the tensile specimen.

an analytical expression for melt pool width w_{MP}[4]. Thus, besides some material-specific parameters, melt pool width mainly depends on the square root of the ratio of laser power P and laser speed v. Related to the L-PBF process parameters used in this study, the respective differences in laser power and speed result in approximately 33 % higher melt pool widths in the hatch scan area than in the contour scan area (contour scan: $P = 100$ W, $v = 350$ mm/s ; hatch scan: $P = 350$ W, $v = 700$ mm/s). This trend is consistent with the observation from the metallographic sections in this work. However, since no in-depth statistical evaluations of the melt pool diameter have been performed, more comprehensive investigations should be carried out relating the energy input to the melt pool diameters.

Besides melt pools, elongated columnar grains of various size are observed. The grains are aligned with BD and frequently spread across the melt pool boundaries indicating epitaxial growth from remelted areas along the maximum thermal gradient [70, 73, 128]. In L-PBF parts, heat is mainly dissipated through the build platform during solidification thus causing

[4] melt pool width $w_{MP} = \sqrt{\frac{8}{\pi e}\frac{\lambda P}{\rho C_p v (T_m - T_0)}}$, with the absorptivity λ, laser power P, density ρ, heat capacity c_p laser speed v, melting temperature T_m and the temperature far from the melt pool T_0, [127]

the alignment of elongated grains with BD [60]. Leicht et al. [129] provided EBSD for cross section in the zx-plane of L-PBF tensile specimens with a thickness of t = 1.0 mm and t = 3.0 mm. These EBSD images confirmed the occurrence of the elongated grains and indicated that specimen thickness does not have a significant effect on the grain size. Nevertheless, these should be reconfirmed in subsequent work using EBSD images of more filigree specimens with a thickness $t \leq 0.5$ mm.

A fine cellular structure is further observed within the grains (figure 5.5d). This fine cellular structure is associated with the high cooling rate and high dislocation densities of L-PBF metals [60, 76]. Dislocation densities of the order of $\rho_d \approx 4{\cdot}10^{14}$ have been reported in the literature for L-PBF 316L, thus resembling dislocation densities of highly deformed metals [60]. Moreover, micro-segregation of chromium, molybdenum, nickel, and manganese were reported at the boundaries of the cellular substructures [60].

In this work, the investigated microstructure of thinner ($t = 0.5$ mm) and thicker specimens ($t = 2.0$ mm) is quite similar. However, there are significant differences in porosity. Porosity is characteristic for L-PBF metals [71, 130, 131]. Spherical pores are mainly associated with gas entrapment, whereas non-spherical pores are commonly referred to as lack of fusion defects. Later are caused by insufficient penetration of the melt pool of an upper layer into the previous solidified layer or the powder [71]. For a specimens with a thickness of t = 0.5 mm, larger, non-spherical pores were frequently observed in the transition region between the hatch and the contour scan (figure 5.4a). This phenomenon was also observed in literature [132]. Thus, Koutiri et al. [132] observed spherical pores with a size of D = 10 - 40 μm in the hatch scan region and non-spherical pores with a size of D = 150 - 220 μm in the transition area between the contour and the hatch scan. As indicated before, non-spherical pores are commonly associated with lack of fusion effects associated with potential exposure errors during the build process [71]. During contour scanning, the edge regions of the parts are re-melted and subjected to a complex thermal history that differs from that of the bulk material [132]. Furthermore, the process parameters for the hatch and the contour scan commonly vary. Thus, the the hatch scan is optimized to maximize the density of the bulk material [133] whereas the the contour scan is optimized to minimize surface roughness [80]. Exposures errors might further be induced by the reduction of the scan lines/exposure times with decreasing specimen thickness. Due to the applied base offset of Δd = 150 μm, the length of the hatch scan lines parallel to the specimen thickness are reduced by Δd = 300 μm; i.e. the scan lines of specimens with a thickness of t = 0.5 mm are reduced to a length of l_{scan} = 200 μm. This reduction in turn favors acceleration and deceleration problems and thus exposure errors, which in turn can lead to the observed lack of fusion pores [132]. The effect of these pores on the mechanical properties of the tensile specimens will be discussed in section 5.2.2.

Microstructure of L-PBF 316L in the heat treated condition

After heat treatment at a temperature of T = 1050 °C, the melt pool boundaries and the fine cellular substructure have vanished while elongated grains and pores are still present (figure 5.4c). The observed microstructure of L-PBF 316L in the heat treated condition is consistent with findings in literature [66, 81, 83]. In the literature, nearly complete dissolution of melt pool boundaries and the cellular substructures were reported after heat treatment at a temperature of T = 1050 °C. This is attributed to the elimination of chemical micro-segregation by atomic diffusion as well as the reduction in dislocation densities [66]. Thus, heat treatment at a temperature of T = 1050 °C is mainly associated with homogenization of the microstructure. Recrystallization and thus grain coarsening and changes in grain shape were reported for heat treatment at a temperature of T = 1200 °C [66, 81, 83]. This observation is also consistent with the findings in the work, as no distinct changes between grain size and shape between the as-built and heat treated specimens were observed at a first glance (figure 5.4).

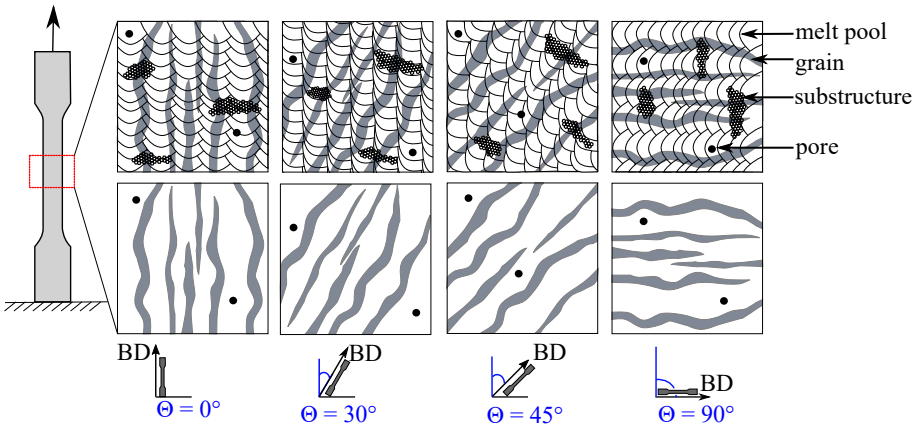

Figure 5.6: Schematic illustration of the microstructure of L-PBF 316L for various specimen orientation angles Θ in the as-built (top row) and heat treated condition (bottom). The as-built condition is characterized by melt pools, elongated grains aligned with the build direction (BD), pores and the fine substructure. After heat treatment at a temperature of T = 1050 °C, no melt pools and substructures are evident, while the elongated grains and pores remain.

5.2.2 Uniaxial tensile properties

In a first step, stress-strain curves obtained from representative L-PBF 316L tensile specimens with a specimen thickness of t = 0.5 mm, 1.0 mm and 1.5 mm 2.0 mm are analyzed (figure 5.7). The stress-strain curves of the L-PBF 316L tensile specimens both in the as-built and heat treated condition are typical for L-PBF metals (figure 5.7, chapter 2.3.3). In the as-built condition, high strength and hardly strain hardening is observed. In the heat treated condition, the yield strength is reduced and strain hardening is increased for all specimen thicknesses and specimen

orientation angles. A more detailed analysis of the differences between the as-built and the heat treated condition will be provided during the detailed analysis of the effects of heat treatment.

For a more comprehensive analysis of the influence of specimen thickness and orientation angle, the yield strength, tensile strength, and elongation at break are evaluated with respect to specimen thickness for the respective specimen orientation angle in figure 5.8.

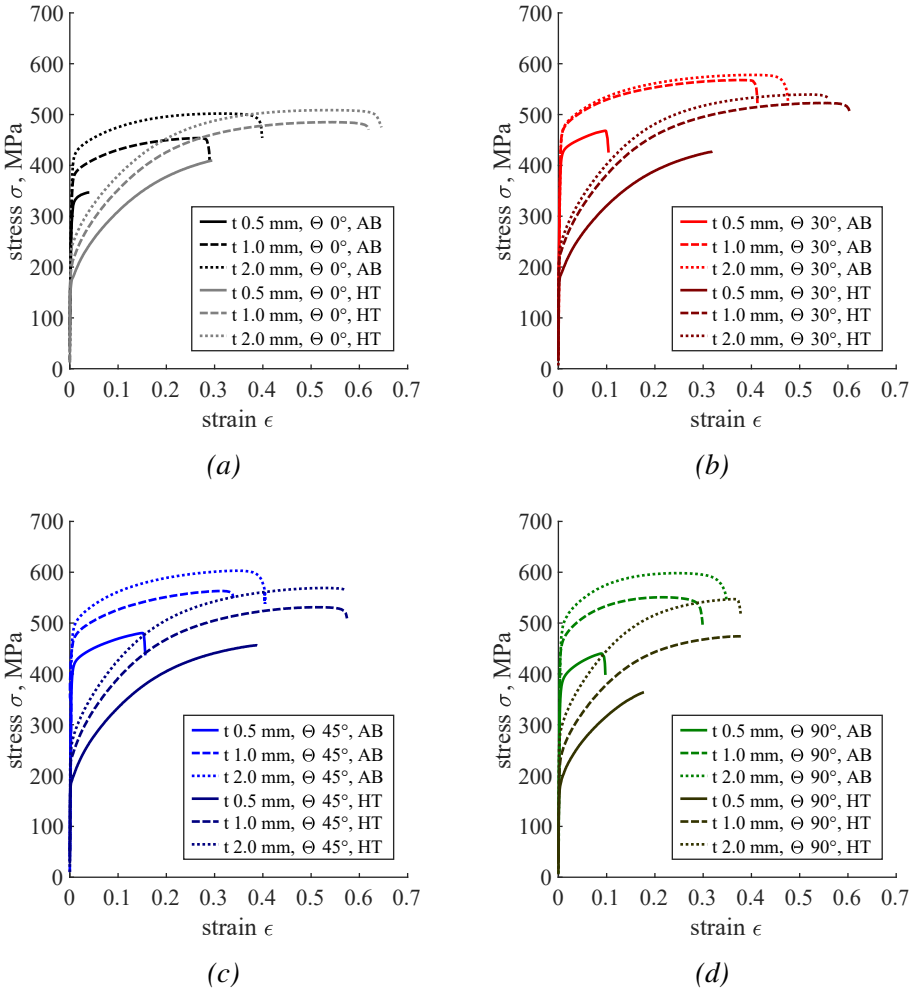

Figure 5.7: Stress-strain curves of selected tensile specimens L-PBF 316L with various specimen thickness t, orientation angle Θ in the as-built (AB) and heat treated condition (HT), adapted from Wiesent et al. [123] and supplemented. Specimen orientation always refers to the angle Θ between the longitudinal axis of the tensile specimens and the build direction (BD).

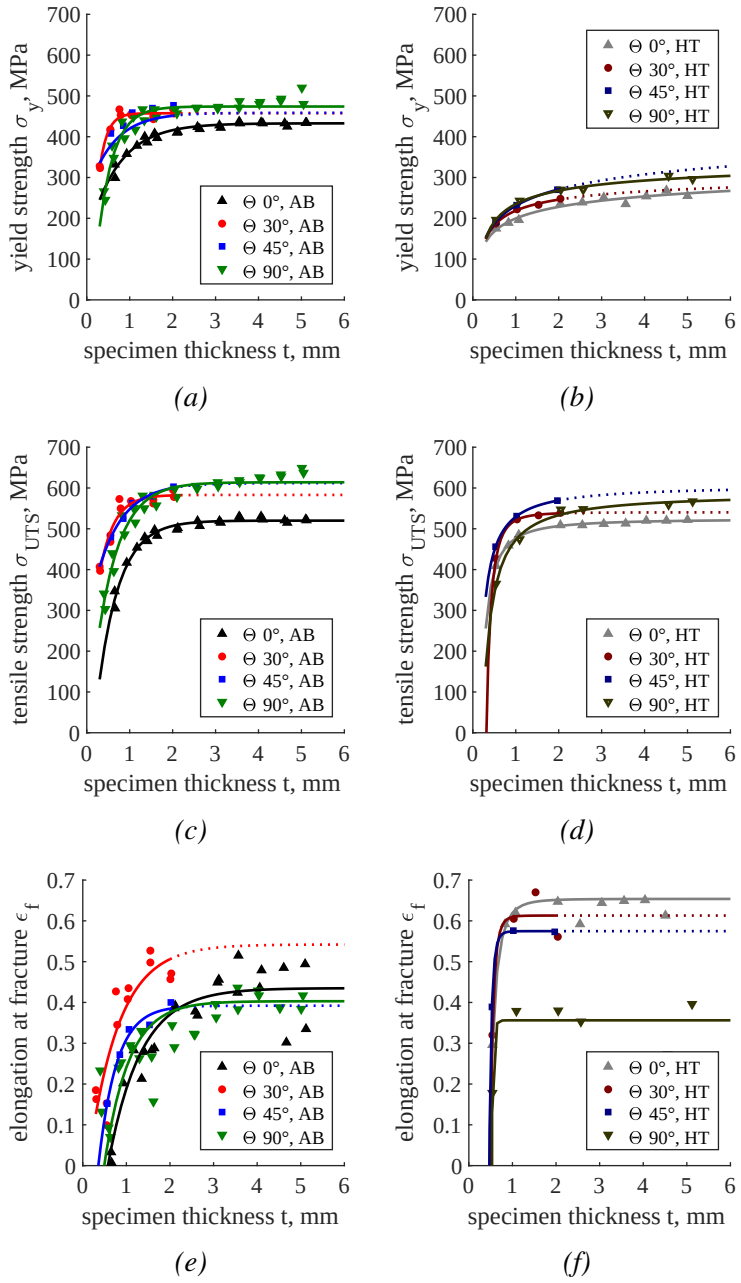

Figure 5.8: Correlation of specimen thickness t with yield strength σ_y (a,b), tensile strength σ_{UTS} (c,d) and elongation at break ε_f (e,f) for specimen with various orientation angle Θ both in the as-built (left column) and heat treated condition (right column), adapted from Wiesent et al. [123].

Impact of specimen thickness on the tensile properties of L-PBF 316L

Regardless of the specimen orientation angle and the post-treatment condition (as-built, heat treated), an increase in yield strength, tensile strength and elongation at break is observed with increasing specimen thickness (figure 5.8). From a specimen thickness of $t > 1.5$ mm, however, the strength values stagnate, so that a saturation value is reached. The increase in strength with increasing specimen thickness, as well as the observed similarity in microstructure and strain hardening behavior at thinner ($t < 1.5$ mm) and thicker ($t > 1.5$ mm) specimen thicknesses, are consistent with previous findings in literature [129, 134]. Therefore, differences in strength between thinner and thicker specimens cannot be attributed to fundamental differences in the microstructure and additional factors must be considered.

L-PBF parts are commonly characterized by high surface roughness, as well as process-related (geometric) defects, such as notches or pores. High surface roughness results from the layer-by-layer build-up during L-PBF as well as from adhering of (partially melted) powder particles. As surface-to-volume ratio increases with decreasing specimen thickness, thinner specimens are more susceptible to process-related geometric imperfections, leading to the observed reduction in strength [134]. Moreover, pores were also found in the investigated L-PBF tensile specimens. In tensile specimen with a thickness of $t = 2.0$ mm, pore diameters of $D_{pore} \approx 5$ - 60 μm were observed on selected metallographic sections (figure 5.5). However, in the metallographic sections of the L-PBF specimens with a thickness of $t = 0.5$ mm, non-spherical pores with a size of up to $D_{pore} \approx 150$ μm have been observed. This difference in pore size and shape could contribute to the observed reduction in strength of the thinner specimen ($t > 1.5$ mm). To evaluate uniaxial tensile tests, the dimension of conventionally manufactured tensile specimens are commonly determined with a caliper. However, the previous described geometric imperfections on the surface of L-PBF specimens as well as internal defects/pores, might provoke a deviation between the actual load bearing cross section and the determined cross section of L-PBF specimens based on caliper measurements (figure 5.9) [129]. Thus, e.g, two adherent powder particles with a maximum powder diameter of $D_{powder} = 45$ μm in combination with a pore diameter of $D_{pore} \approx 150$ μm, might result in a maximum measurement errors of up to $\Delta t = 240$ μm in the worst case. For a nominal specimen thickness of $t = 0.5$ mm, this measurement error would lead to an underestimation of the determined strength values by up to 48 %. In contrast, for specimens with a nominal thickness of $t = 2.0$ mm, the same measurement error would only cause an underestimation of 11 %. This susceptibility to errors in the determination of specimen dimensions by calipers was also addressed by Leicht et al. [129], who found that the diameters determined by caliper were about 120 μm larger than those determined by microscopy. To account for this potential measurement error, the result of the uniaxial tensile test of the as-built specimens was exemplary adjusted by a mean measurement error, i.e. the determined specimen thickness was reduced by a fictitious mean measurement error of $\Delta t = 90$ μm before determining the respective material parameters (figure 5.10). This reduction corresponds, e.g., to

a representative pore with a diameter of D_{pore} = 50 μm and two adherent powder particles with a diameter of D_{powder} = 20 μm each or one larger pore with a diameter of D_{pore} = 90 μm. A similar approach was previously used in a study by Gonzalez et al. [37] to account for variations in the real load-bearing strut cross section in the numerical analysis of L-PBF lattice structures.

After adjusting the cross sectional area to account for the possible measurement error, the significant decrease in strength with decreasing specimen thickness is still evident. However, saturation of the respective material parameter is already reached at a specimen thickness of $t \approx 1$ mm. It can therefore be assumed that the decrease in strength with decreasing specimen thickness is due to even further factors.

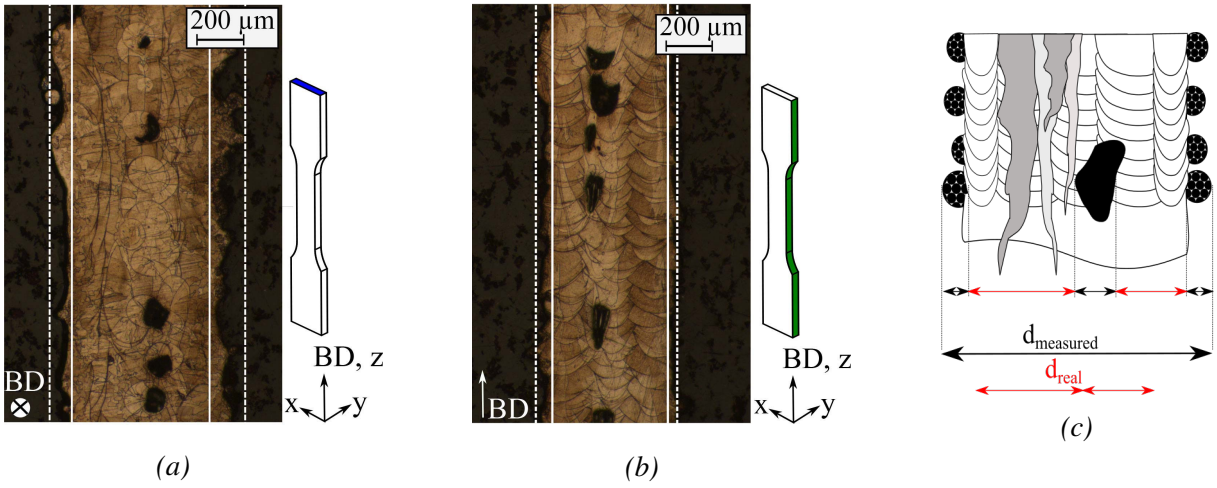

Figure 5.9: Illustration of the potential measurement error using metallographic sections of tensile specimen with a thickness of t = 0.5 mm in the as-built condition. (a) Metallographic section in the xy-plane. The xy-plane is schematically illustrated by the blue face of the tensile specimen next to the metallographic section. (b) Metallographic section in the yz-plane. The yz-plane is further schematically illustrated by the green face of the tensile specimen next to the metallographic section. (c) Schematically comparison of the actual load-bearing dimension d_{real} and measured dimension $d_{measured}$ of the L-PBF tensile specimen. Deviations between d_{real} and $d_{measured}$ are attributed to adherent powder particles and internal defects/pores.

One of these factors is the increased impact of the surface layer on specimen with a reduced specimen thickness. The following overview on the impact of the surface layer is based on Ref. [135], which is referred to for further description. Metals are characterized by a natural surface layer, which is composed of a certain number of sublayers depending on the material. Weaker energy barriers to dislocations exist at free specimen surfaces, allowing an increased number of dislocation motions in the surface sublayer and thus reducing the yield strength at the sublayer compared to the bulk/central material. Plastic yielding in the outer sublayer in turn reduces the dislocation barrier and thus also the yield strength in the next sublayer. The surface layer is restricted to a certain number of sublayers characterized by a reduced yield

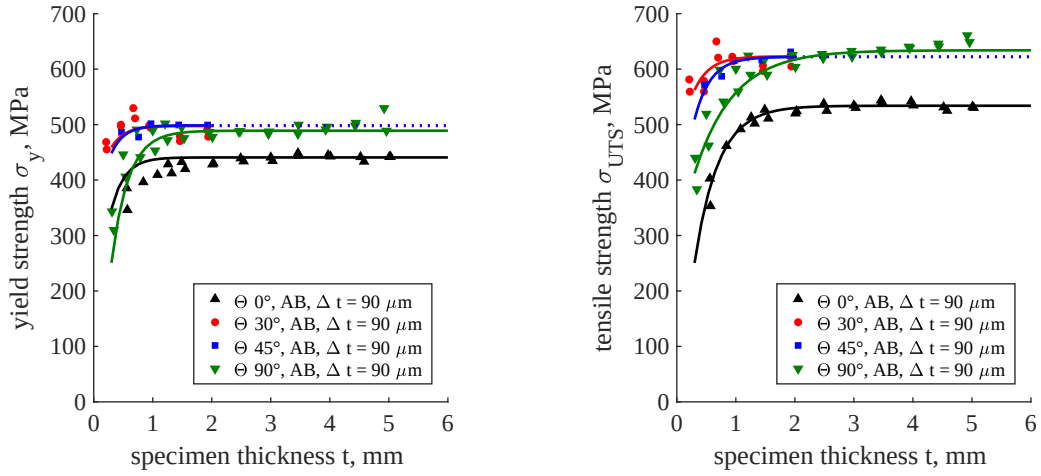

Figure 5.10: Correlation of the strength values and specimen thickness after dimensional measurement correction: (a) Yield strength σ_y and (b) tensile strength σ_{UTS} with dimensional measurement correction by reducing the specimen thickness t by $\Delta t = 0.09$ µm, adapted from Wiesent et al. [123].

point compared to the bulk/central material. Thinner specimens have a smaller number of grains across the specimen thickness. As a result, major parts of the specimens consists of these surface sublayers with a reduced yield strength, which in return decreases the overall yield strength of the specimens. The strength reducing effect of the surface layer is also present in thicker specimen. However, due to the increased number of grains across the specimen thickness, the reduction in yield strength at the surface layer will be partially compensated by the bulk/central material behavior. Thus, with increasing specimen thickness, the strength reducing effect of the surface layer has less effect on the macroscopic behavior of the specimen.

Finally, the change in specimen strength with specimen thickness may also be due to the applied scanning strategy and, in particular, the contour scanning. As previously described, large, non-spherical pores with a size of up to $D_{pore} = 150$ µm were observed in the transition area between contour and hatch scan (figure 5.9). Although these pores were also found in specimens with a thickness of $t = 2.0$ mm, their occurrence is considerably more frequent in specimens with a thickness of $t = 0.5$ mm. These pores lead to a reduction of the load-bearing cross section and thus to the observed overall reduced strength of the L-PBF tensile specimens. However, a more detailed investigation, e.g., a comprehensive analysis of porosity and its relation to process parameters, scanning strategies and specimen thickness, are required to better substantiate this assumption.

The elongation at break shows a large scatter for all specimen orientations (figure 5.8e, f). Nevertheless, the tendency of an increase in elongation at break with increasing specimen thickness is also evident.. Besides L-PBF process-related (geometric) irregularities, the reduction

in elongation at break with decreasing specimen thickness can be related to specimen geometry, i.e., slenderness ratio. The slenderness ratio k is defined as the ratio of the gauge length l_0 and the specimen cross section A_0 ($k = l_0/\sqrt{A}$). Moura et al. [84] found a linear relationship between slimness ratio and ductility for AM flat tensile specimens made of titan alloy (Ti-6Al-4V), as per the Bertella–Oliver equation[5]. Thus, a reduction in specimen thickness (i.e., an increase in slenderness ratios) was found to be related to a reduction in elongation at break. In the study of Moura et al. [84], the investigated tensile specimens had cross sections of A = 6 x 6 mm^2, A = 6 x 3 mm^2, and A = 12.5 x 2 mm^2 and an initial gauge length of l_0 = 25 mm and l_0 = 50 mm, respectively. In the present work, the specimen thickness of the investigated L-PBF 316L tensile specimen was further reduced which might exaggerate the reduction in ductility due to the further increase in slenderness ratio. In this work, large variations of elongation at break were observed for thin specimens with a thickness of t < 1.5 mm. This trend was also observed in literature and might be attributed to an unfavorable distribution of defects (e.g., pores, lack of fusion defects, staircase effect) [129]. Furthermore, with decreasing specimen thickness, the surface-to-volume ratio of the specimen increase potentially increases the susceptibility to local imperfections or notch effects arising from the high surface roughness of L-PBF parts. Thus, in summary, the reduction of elongation at break with decreasing specimen thickness can be attribute to the increase in slenderness ratio in combination with L-PBF process related (geometric) irregularities/defects and the increase in surface-to-volume ratio of thinner tensile specimens.

Impact of heat treatment on the tensile properties of L-PBF 316L

The impact of specimen thickness was already presented above. Thus, for the analysis of the impact of heat treatment on the tensile properties of L-PBF 316L tensile specimens, the focus is on specimen with a thickness of $t > 1.5$ mm.

In the as-built condition, the tensile specimens exhibit high yield strength combined with a low degree of strain hardening and ductility (figure 5.7, figure 5.8). Furthermore, anisotropy of the mechanical properties is observed. From a specimen size of $t > 1.5$ mm, with yield strength of $\sigma_{y,L-PBF_{AB}} \approx$ 380 - 520 MPa, the yield strength of L-PBF 316L tensile specimens distinctly exceeds the yield strength of conventional manufactured 316L of $\sigma_{y,con}$ = 170 MPa [75]. With tensile strength of $\sigma_{UTS,L-PBF_{AB}} \approx 480 - 650$ MPa, the tensile strength values of the L-PBF 316L tensile specimens approximates or even exceeds the values of conventional manufactured 316L ($\sigma_{UTS,con}$ = 485 MPa, [75]).

Initially the increased strength of as-built L-PBF 316L is associated with the refined microstructure inherent for L-PBF materials compared to its conventional processed counterpart [60]. High

[5]Bertella–Oliver equation: $\varepsilon_f = e_0 \cdot k^(-a)$, with e_0 and a being material constants

temperature gradients and densification rates during L-PBF further induce high dislocation densities and residual stresses causing the L-PBF material to undergo saturation with respect to strain hardening [76, 77, 80]. High yield and tensile strength of as-built L-PBF 316L might further be attributed to the presence of δ-ferrite [38]. δ-ferrite exhibits a higher content of chromium and molybdenum than the austenitic matrix and therefore acts as a strength enhancing second phase. However, there are also studies that report a purely austenitic L-PBF 316L without the occurrence of δ-ferrite [60]. Since no phase analysis was performed in this work, the potential strength-increasing mechanism of δ-ferrite needs to be substantiated by further investigations.

The stress-strain curves of the heat treated tensile specimens, exhibit reduced yield and tensile strength but increased work hardening, ductility and elongation at break compared to the as-built specimens which is consistent with findings in the literature (figure 5.7, figure 5.8) [66, 81, 83]. With yield strengths of $\sigma_{y,L-PBF_{HT}}$ = 230 - 300 MPa and tensile strength values of $\sigma_{UTS,L-PBF_{HT}}$ = 410 - 560 MPa, the strength values of the heat treated L-PBF 316L specimens clearly approach or even exceed those of conventional 316L ($\sigma_{UTS,con}$ = 485 MPa , [75]).

The observed distinct decrease in yield strength of the heat treated L-PBF 316L is attributed to the reduction of dislocation densities and the dissolution of micro-segregation (e.g. melt pool boundaries, fine cellular structures) during heat treatment (figure 5.4c) [83]. In literature, heat treatment at a temperature of T = 1050 °C was further found to reduce/dissolve δ-ferrite [38]. Thus, the reduction of δ-ferrite as a strength-enhancing second phase could contribute to a reduction in the strength of the heat treated specimens. Again, as no phase analysis was conducted in this work, this assumption needs to be substantiated by further investigations. The preservation of the high tensile strength is related to the applied heat treatment temperature and the associated microstructure. At a heat treatment of T = 1050 °C, homogenizing of the microstructure occurs without complete recrystallization and the associated grain coarsening; i.e. the strength-enhancing effect of the fine-grained structure inherent for L-PBF metals is retained.

Impact of specimen orientation angle on the tensile properties of L-PBF 316L

The influence of specimen orientation angle on the mechanical properties of the tensile specimens is particularly pronounced at low specimen thickness of $t < 1.5$ mm, whereas the influence of specimen orientation gradually decreases with increasing specimen thickness. From a specimen thickness of $t > 1.5$ mm, the yield and tensile strength of as-built tensile specimens with a specimen orientation of Θ = 30°, 45° and 90° is quite similar, i.e. $\sigma_{y,L-PBF,AB} \approx$ 450 - 500 MPa and $\sigma_{UTS,L-PBF,AB} \approx$ 570 - 640 MPa). However, yield and tensile strength of the as-built tensile specimens with a specimen orientation of Θ = 0° are significantly reduced, e.g., by about 12 % and 14 %, respectively, compared to a specimen orientation angle of Θ = 90° for a specimen thickness of t =1.5 mm.

The observed anisotropic mechanical behavior of as-built L-PBF tensile specimen depending on the specimen orientation angle with respect to the BD is characteristic of L-PBF parts. These direction-dependent properties are mainly attributed to the layer-by-layer manufacturing process and the resulting microstructure, although the distinct contribution of the individual factors is still unclear [68, 70, 73, 136]. Anisotropy in yield strength is associated with grain structure or more specifically the alignment of the columnar grains with respect to loading direction. Depending on the specimen orientation angle, the microstructure of L-PBF 316L appears finer or coarser grained perpendicular to the loading direction. Following the Hall-Petch relation[6] (i.e., intrinsic size effect; grain boundary strengthening), the yield strength increases with decreasing grain size. This is due to the obstruction of the dislocations at the grain boundaries, and the increased energy required to advance the dislocation beyond the grain boundaries. Thus, the obstruction of the dislocations prevents the onset of plastic deformation and thus increases the yield strength. At a specimen orientation angle of $\Theta = 90°$, the finest grain dimension is perpendicular/normal to the loading direction. At a specimen orientation of $\Theta = 0°$ however, the coarsest grain dimension is perpendicular to the loading direction which is associated with reduced strength. Thus, as per the Hall-Petch relation the yield strength of specimen orientation angle of $\Theta = 90°$ is increased whereas the yield strength of specimen orientation angle of $\Theta = 0°$ is decreased. It was also found in the literature that analogous to the grains, the cellular substructures are also preferentially aligned with the BD and thus their strength enhancing effect is also anisotropic [83]. Finally, anisotropy is also related to different heating and cooling processes and thus the development of different local dislocation densities between the different specimen orientation angles [83].

In the heat treated condition, the difference in the strength values of the various specimen orientation angles is decreased. Thus, e.g. for a specimen thickness of t =1.5 mm, yield strength values of $\sigma_{y,L-PBF,HT} \approx$ 195 - 250 MPa and tensile strength values of $\sigma_{UTS,L-PBF,HT} \approx$ 470 - 500 MPa were observed for all specimen orientation angles including the specimen orientation of $\Theta = 0°$. Since elongated grains are still present after the applied homogenization heat treatment, the observed reduction of anisotropy is mainly associated with the reduction of the dislocation densities and the dissolution of the cellular substructures following heat treatment. As discussed before, the elongation at break shows high variability. In the literature, this variance is mainly attributed to the presence of pores and, in particular, to an unfavorable arrangement of large pores as well as their orientation with respect to the loading direction [83]. If the main axis of the pore is aligned perpendicular to the direction of loading, stress concentrations occur at their apexes even at low loads and initiate crack growth or ductile void growth. In addition, surface defects, e.g. due to the staircase effect, the overmelting of downward-facing surfaces, notches or due to local damage when removing the support structure, further impair the elongation at break. Specimen with an orientation angle of $\Theta = 0°$ are less susceptible to these factors, which

[6] $\sigma_y = \sigma_0 + k_y/\sqrt{D_{rain}}$, with σ_y being the yield stress, σ_0 a material constant describing the starting stress for dislocation movement, k_y the strength coefficient, and D_{grain} the average grain diameter

in return leads to their observed increase in elongation at break. For the heat treated specimens, reduced elongation at break is particularly noticeable at a specimen orientation angle of $\Theta = 90°$ for all specimen thicknesses. Apart from a potential local microstructural defect (e.g., lack of fusion, local powder recoating defects), this could be due to damage to the specimens during removal of the support structures.

5.2.3 Limitations and scope of future work

There are some limitations in the work that merit further discussion. Due to the small number of specimens, especially for the heat treated specimens, no statistically reliable statements can be made. Furthermore, the mechanical properties of L-PBF specimens are known to be dependent not only on the raw material, but also on the L-PBF machine and the applied process parameters. Therefore, overarching quantitative statements or generalizations about the influence of individual geometric parameters on the material behavior of the specimen are hardly reliable. However, since the basic findings of decreasing strength with decreasing specimen thickness are consistent with the findings in the literature [129, 134], the trends identified in this work can be used as a rough guideline for the development of filigree L-PBF structures. Nevertheless, further in-depth investigations are necessary to statistically validate the obtained results. For this purpose, further L-PBF tensile specimens should be analyzed, and multi-scale investigations should be performed to draw conclusions from the microstructure to the macroscopic part behavior. This multi-scale investigations should include comprehensive analysis of the microstructure (e.g., grain size, shape, orientation, phases), the porosity (pore size, pore shape, distribution) as well as local hardness measurements (e.g., nanoindentation), to obtain quantitative correlations between the microstructure and the mechanical properties of L-PBF 316L. However, such a detailed analysis was beyond the scope of this work. Rather, the aim was to determine whether the mechanical properties of L-PBF standard tensile specimens can be transferred to L-PBF filigree structures, such as L-PBF stents.

Furthermore, this study was limited to a fixed set of standard L-PBF material parameters. The quality of L-PBF parts, and especially of filigree structures, was found to be strongly dependent on a variety of L-PBF process parameters, e.g., laser type, laser power, scanning speed, scanning strategy and hatch spacing [137]. Although fundamental effects, e.g., due to size effects or microstructure, will also occur with a different choice of process parameters, it is nevertheless likely that the quantitative values, e.g. with respect to the extent of anisotropy, strength or ductility, will differ from the values determined in this work. It is therefore necessary to verify the findings of this work by further investigations with a more comprehensive set of various process parameters.

This work also showed that the process parameters of bulk specimens ($t > 2.0$ mm) are only conditionally suitable for more filigree L-PBF structures. Thus, especially in thinner specimens ($t < 0.5$ mm), lack-of-fusion pores were frequently observed in the transition region between the hatch and the contour scan. Since the number of these lack of fusion pores decreased with increasing specimen thickness, it can be concluded that the L-PBF process parameters used in this work were suitable for bulk specimens but hardly for filigree structures. To ensure the quality of filigree L-PBF structures, the L-PBF process parameters must be optimized specifically to meet the requirements of these filigree structures.

In this work, an industrialized L-PBF machine was used to build the L-PBF tensile specimens. For the applied laser power, this machine has a laser spot diameter of $D \approx 100 - 150$ μm. Thus, with a melt pool diameter of $D_{MP} > 150$ μm, only a few melt pools extend across the specimen thickness of the thinner specimens. It is therefore likely that filigree L-PBF structures are more prone to local exposure/surface defects due to the limited number of melt pools and grains across the specimen thickness. Thus, by using L-PBF machines specifically designed for filigree L-PBF structures, the mechanical behavior of filigree specimens could be improved by the realization of smaller melt pool sizes and thus a higher number of melt pools across the specimen thickness. It is therefore necessary to verify the results of this work with further analysis of L-PBF specimens built on L-PBF machines specialized in the production of filigree structures.

Finally, one must emphasize that the mechanical properties determined on the L-PBF 316L tensile specimens are likely not suitable for describing the mechanical behavior of L-PBF stents. For comparability reasons, the mechanical behavior of L-PBF stents must be determined using miniaturized L-PBF tensile specimen with comparable dimension to the latter stent. However, as indicated before, the determination of the mechanical properties of single L-PBF struts poses a great challenge, in manufacturability, experimental methods and reliability of the obtained results. Therefore, other methods for determining the mechanical properties of L-PBF stents should be considered, such as inverse determination of mechanical properties based on combined experimental and numerical analysis of the macroscopic response of the L-PBF stent to deformation, similar to L-PBF lattice structures.

5.3 Conclusion

In this chapter, the influences of specimen thickness, specimen orientation angle, and homogenizing heat treatment on the microstructure and the mechanical properties of L-PBF 316L tensile specimens were investigated. The following conclusions are drawn:

- With increasing specimen thickness, the strength of L-PBF flat tensile specimens increases, reaching saturation from a specimen thickness of $t > 1.5$ mm, resembling the bulk material properties. The reduced strength of the thinner specimens ($t < 1.5$ mm) is attributed to the size effect, the increased slenderness ratio, and the increased susceptibility of the filigree structures to L-PBF process-related defects.

- The anisotropic mechanical behavior dependent on the specimen orientation angle to BD are particularly pronounced for thinner specimens ($t < 1.5$ mm) and decrease with increasing specimen ($t > 1.5$ mm) thickness. After reaching the saturation value, specimens with an orientation angle of $\Theta = 30°$, 45° and 90° exhibit approximately the same strength, whereas specimens with an orientation angle of $\Theta = 0°$ show significantly lower values. For the determination of the anisotropic material properties of L-PBF specimens, testing of the two extremes of the orientation angles, i.e., $\Theta = 0°$ and $\Theta = 90°$, might therefore be sufficient.

- Post-processing heat treatment can alter the microstructure and thus the mechanical behavior of L-PBF 316L. The applied homogenization heat treatment at a temperature of $T = 1050$ °C leads to a reduction of yield strength while maintaining the ultimate tensile strength and anisotropy of the L-PBF 316L.

- Specimen thickness, orientation angle and subsequent heat treatment have a distinct effect on the mechanical behavior of L-PBF 316L specimens. Comparison of the mechanical properties of L-PBF specimens is therefore only reasonable for L-PBF specimens with similar specimen thickness, orientation angle and post-processing condition. For reliable structural mechanical evaluation of L-PBF parts, and especially for filigree L-PBF structures, only the mechanical properties determined on specimens with comparable size and orientation to the later L-PBF part may be used. If this is not possible, other ways to account for the influence of the size effect on the mechanical properties of the L-PBF structures must be considered, e.g., using a correction factor or inverse determination of the mechanical properties of the L-PBF structures.

6 Computational analysis of L-PBF stents

Based on the preceding findings regarding the numerical analysis of conventional stents (chapter 4), as well as the experimental analysis of L-PBF 316L tensile specimens (chapter 5), this chapter presents a methodology for determining the mechanical properties of L-PBF 316L stent, as well as their numerical analysis.

As already indicated in the literature review (chapter 2.3.4), L-PBF lattice structures/stents are affected by a variety of process-related geometric irregularities, including local variations in strut diameter and cross sectional shape, surface roughness, strut waviness, tapers, and porosity [25, 34–37]. Combined experimental and numerical studies have shown that these geometric irregularities have a distinct influence on the mechanical properties of L-PBF lattice structures, leading to differences between the numerical prediction based on the as-designed geometry and the experimentally determined mechanical response of the L-PBF structure [25, 34–37, 45]. These studies suggest that reconstruction from, for example, X-ray CT or statistical consideration of process-related geometric irregularities is essential for the accurate prediction of the process-structure-property relationship of L-PBF lattice structures. Conventional approaches to numerical stent analysis/optimization based on idealized models are therefore unlikely to be suitable for the analysis of L-PBF stents and therefore need to be adapted to account for the specific features of L-PBF stents.

The mechanical behavior of L-PBF stents is further expected to be influenced by the size effect, resulting in deviation between the mechanical response of the bulk material and the actual L-PBF stent/lattice structures [25, 31, 33, 128]. As shown in chapter 5, the yield strength of L-PBF 316L flat tensile specimens with a thickness of t = 0.5 mm is reduced by about 30 % compared to specimens with a thickness of t = 2.0 mm. This trend is further supported by the findings of Ravari et al. [25], who found a reduction in strength of L-PBF 316L lattice struts (D_{strut} = 200 μm) by about 25 % compared to L-PBF 316L bulk material.

Besides the geometric irregularities inherent for L-PBF, the morphology and mechanical behavior of L-PBF stents are further expected to be by influenced by post-processing steps, such as heat or surface treatment (viz., electropolishing). Theses post-processing steps are intended to increase the ductility as the biocompatibility of the stents. As for surface treatment, 316L stents are usually electropolished to smooth their surface and create a passivation layer, which increases

the corrosion resistance and thus the biocompatibility of 316L stents. [64, 138]. Post-build heat treatments are intended to improve the microstructure and corresponding mechanical properties of L-PBF 316L stents. For L-PBF stents, homogenization rather than recrystallization heat treatment should be considered. Recrystallization heat treatment is associated with grain coarsening thus a reduction of the ultimate tensile strength of L-PBF 316L as per the Hall-Petch relation. Homogenization heat treatment on the other was found to decrease yield strength and increase ductility while preserving the ultimate tensile strength. In contrast to recrystallization heat treatment, homogenization heat treatment dissolves only the melt pool boundaries, substructures, and δ-ferrite and reduces residual stresses, while grain sizes and orientations remain approximately unchanged from the as-built condition (chapter 5.2.2) [38, 65, 80].

In summary, L-PBF process-related geometric irregularities, post-processing steps, and the size effect are all expected to have an impact on the mechanical response of L-PBF 316L stents. The development and optimization of L-PBF stent designs based on idealized CAD models are, therefore, likely not appropriate. Thus, the applicability of the numerical methods established for the analysis and optimization of conventionally laser-cut stents should be investigated.

Therefore, in this chapter, the impact of process-related geometric irregularities, the size effect, and post-processing steps on the mechanical response of L-PBF 316L stents using a combined experimental and computational framework is investigated. Moreover, a numerical framework for the evaluation of both the mechanical properties and the expansion behavior of L-PBF stents is provided and compared to existing approaches for conventionally manufactured stents. The content of these chapters was published in Wiesent et al. [139] and is adopted in this chapter with only minor adjustments, mainly concerning the reading flow and nomenclature of the overall context of this doctoral thesis.

6.1 Methods

6.1.1 Design of the stent

The L-PBF stents had a self-supporting, closed-cell design composed of two unit cells in the circumferential direction and six unit cells in the axial direction. The unit cell exhibited a zigzag pattern of serrated main struts (spikes) with an angle of $\alpha = 45°$ (figure 6.1, orange) and two non-flexible connecting struts along the longitudinal stent axis (figure 6.1, green). The stent struts had a quadratic cross section with a thickness of $t = 0.1$ mm. The stents have a length of $l = 16.94$ mm and a nominal outer diameter of $D_o = 3$ mm. After stent expansion, a nominal outer stent diameter of $D_o = 3.7$ mm is intended. The stent design and its basic dimensions are illustrated in figure 6.1. The stent design was chosen so that it can be manufactured without

support structures using L-PBF. It was not intended to provide a specially optimized stent design. Rather, the focus was on the identification of factors that influence the mechanical behavior of L-PBF stents and on the development of a numerical methodology that could be used for the analysis and optimization of L-PBF stents.

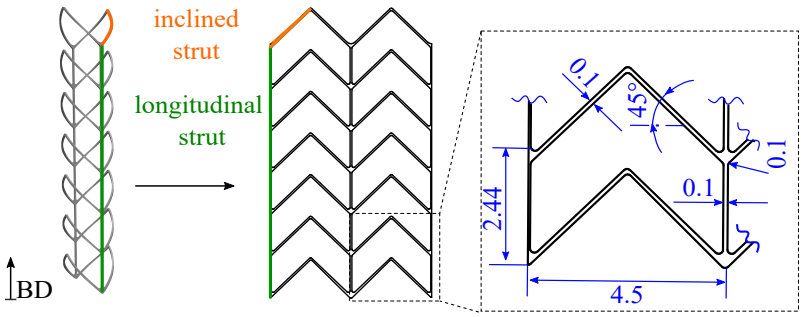

Figure 6.1: Intended stent design Stent CAD model and its flat projection highlighting the basic dimension of the intended stent within the magnified stent unit cell. The later built direction (BD) within the laser powder bed fusion process is indicated by the arrow, adopted from Wiesent et al. [139].

6.1.2 Experimental framework

Within the experimental framework, cardiovascular stents were produced from 316L using L-PBF. Subsequently, the stents were selectively subjected to post-processing, targeting three different stent conditions: i) as-built, ii) heat treated, and iii) electropolished and heat treated condition. One representative stent per stent condition is analyzed by X-ray CT for morphological and subsequent numerical analysis. The compression behavior of the L-PBF stents is then evaluated using a compression test between two plates according to DIN EN ISO 25539-2 [140]. To characterize the material behavior of L-PBF 316L, uniaxial tensile tests on flat specimens were performed, both in the as-built and heat treated condition. In the following, the respective experimental tests are described. A summary of the experimental tests is provided in Table 6.1.

Laser powder bed fusion process

The L-PBF stents and tensile specimens (DIN 50125 form E [124], thickness of t = 1.0 mm) were made from gas-atomized 316L powder with a particle diameter of D_{powder} = 15 - 45 μm[1]. An SLM® 250 machine[2] equipped with a 400 W Yb-fibre-laser was used with the following standard process parameters: laser power of P = 350 W, scanning velocity of v = 700 mm/s, focus position of 0, layer thickness of t = 30 μm, hatch distance of h = 80 μm, and rotation per layer of α = 83°. Furthermore, platform preheating with a temperature of T = 100 °C was

[1] 316L powder: LPW, Rundkorn, United Kingdom
[2] SLM® 250 machine: SLM Solutions Group AG, Lübeck, Germany

Table 6.1: Overview of the experimental framework.

Method	Test specimens	Aim
Mechanical testing		
Tensile test	2 L-PBF flat specimens (1 AB, 1 HT)	Determination of the mechanical properties/flow curves of L-PBF 316L
Uniaxial compression between two plates	12 L-PBF stents (4 each for AB, HT and EP-HT)	Determination of the macroscopic response of the L-PBF stents under compression
Characterization		
X-ray CT	3 L-PBF stents before and after compression (1 each for AB, HT and EP-HT)	Reconstruction of L-PBF stent models; Analysis of process-related geometrical irregularities
SEM	3 L-PBF stents (1 each for AB, HT and EP-HT)	Analysis of process-related geometrical irregularities
Metallographic analysis	2 L-PBF stents (1 each for AB and HT)	Determination of the impact of heat treatment on the microstructure of L-PBF 316L stents

AB: as-built condition; HT: heat treated condition; EP-HT: electropolished and heat treated condition

employed. At maximum power (P = 400 W) the laser had a spot diameter of D_{laser} = 150 μm. With the selected process parameters, a minimum strut diameter of about D_{strut} = 200 μm and a density of $\rho \geqq 99$ % can be achieved, which is in a comparable range to the L-PBF CoCr stents previously published in Finazzi et al. [31]. BD was parallel to the longitudinal stent axis (figure 6.1, blue arrow). The longitudinal struts at the bottom end of each stent were extended to serve as supports for the stents and to prevent the fusion of the stent spikes with the build platform. The stents were removed from the build platform by cutting these extensions. The tensile specimens were aligned in a standing position with the longitudinal (loading) axis of the specimen parallel to BD (specimen orientation angle of $\Theta = 0°$).

Post-build treatments

Three different stent conditions were considered: i) as-built, ii) heat treated, and iii) electropolished and heat treated condition. The stents in the as-built condition were only cut from the build platform and did not undergo any post-processing steps. The stents in the heat treated condition and the stents in the electropolished and heat treated condition were subjected to heat treatment at a temperature of T = 1050 °C for a duration of t_H = 1 h and subsequently cooled inside the furnace. This heat treatment was intended to homogenize the microstructure, to decrease the yield strength and increase ductility, thus increasing the deformability of the stents and enabling stent crimping and expansion. The stents in the electropolished and heat treated condition were additionally electropolished after heat treatment using the electrolyte Poligrat E 268 at a temperature of T = 85 °C with a voltage of V = 3.8 V and an electric current of I = 5.5 - 6 A for a duration of t = 4 minutes. Analogous to the stents, flat tensile specimens (DIN 50125 form E [124], thickness of t = 1 mm) were prepared in the as-built and heat treated

condition. The parameters of the heat treatment were analogous to the stents. To minimize the influence of surface roughness and thus to determine the bulk material properties, all tensile specimens are electropolished before testing (t_{EP} = 7 min, T = 85°C, V = 6 V, I = 5.5 - 6 A).

Geometrical analysis

The morphology and internal defects of the L-PBF stents were determined by X-ray CT[3] with a source voltage of V = 90 kV, an intensity of I = 390 μA, and a voxel size of 8.5 x 8.5 x 8.5 μm^3. X-ray CT was performed for each stent in the undeformed condition as well as after compression tests. The X-ray CT data was further used for the reconstruction of the L-PBF stent models within the numerical analysis and their validation. For a more detailed analysis of the strut surfaces and local deformation concentrations, SEM[4] imaging was performed for each stent after the compression with parallel plates. The stent mass was determined using a monolithic weighing system[5].

Metallographic analysis

For the metallographic analysis of the influence of heat treatment on the microstructure of L-PBF 316L stents, metallographic sections of a stent were analyzed for the as-built and heat treated conditions. To do so, the stents were cut lengthwise, embedded planarly in hot mounting resin, ground, mirror polished and etched in hot V2A etchant, and then analyzed with a light microscope following standard practice. The stents that were destructively characterized were manufactured together with the stents experimentally investigated here and subjected to the same heat treatment.

Mechanical Testing

To determine the material properties of L-PBF 316L, uniaxial tensile tests were performed on L-PBF 316L tensile specimens in the as-built and heat treated condition. The tensile tests were performed at room temperature using a universal testing machine[6] with a constant loading speed of v = 1 mm/min and a loading cell of 50 kN. Strain was measured using an extensometer with an initial gauge length of l_0 = 25 mm.

To assess the macroscopic mechanical behavior of the L-PBF stents under compression, room-temperature compression tests with parallel plates were performed (figure 6.2). This test is commonly used to determine the crush resistance of stents following the standard DIN EN ISO 25539-2 [140]. Therefore, a universal testing machine with a constant loading speed of v = 1 mm/min and a loading cell of 500 N was used. The stent was positioned between the

[3]X-ray CT: Phoenix v|tome|xs 240-180, GE Sensing Inspection Technologies, Hürth, Germany
[4]SEM: 1450 VP, LEO Elektronenmikroskopie GmbH, Oberkochen, Germany
[5]Monolithic weighing system: Sartorius LA310S, Sartorius,Göttingen, Germany
[6]Universal testing machine: Hegewald & Peschke Mess- und Prüftechnik GmbH, Nossen, Germany

two plates so that the longitudinal struts were aligned centrally and parallel to the plates. A total of twelve L-PBF stents were tested: i) four in the as-built condition, ii) four in the heat treated condition and iii) four in the electropolished and heat treated condition.

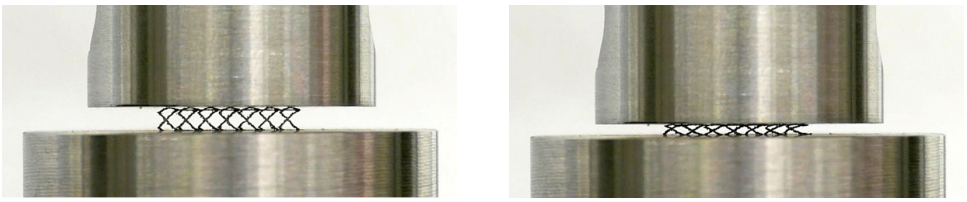

(a) *(b)*

Figure 6.2: Experimental set up of the stent compression tests with parallel plates, adopted from Wiesent et al. [139]. (a) Initial positioning of the stent between the two plates. (b) Stent after compression between the two plates.

6.1.3 Computational framework

Within the numerical framework, three representative stent models were reconstructed from the X-ray CT data: i) stent_{AB} in the as-built, ii) stent_{HT} in the heat treated, and iii) $\text{stent}_{\text{EP-HT}}$ in the electropolished and heat treated condition. Flow curves were then derived from the uniaxial tensile tests to describe the material behavior of L-PBF 316L in the as-built and heat treated condition. Thereupon, the three reconstructed stent models are analyzed using FEA. Two loading scenarios were simulated: i) compression between parallel plates and ii) stent crimping and free expansion. The numerical study was further extended to include the idealized CAD model $\text{stent}_{\text{CAD}}$ on which the L-PBF stents are based, which allows for the comparison between the actual and as-designed mechanical response of the stents. The numerical predictions are then validated against the experimental data before the influence of post-processing (heat treatment, surface treatment) on the development of the stress states within the stent are evaluated based on the numerical analyses.

Within the computational framework, the FE solver Abaqus/Explicit 2019 was used for the analysis of the L-PBF stents. Care has been taken to ensure that the ratio of kinetic to internal energy does not exceed a critical value of $E_{KE}/E_I < 5$ - 10 % during the major part of the process, so that the influence of inertial effects is negligible [47]. In addition, a mesh convergence study was carried out to select an adequate mesh density that would allow sufficient accuracy within a reasonable calculation time.

3D reconstruction of the L-PBF stents

Due to high numerical requirement, only one representative model for each investigated condition of the L-PBF stents was reconstructed from X-ray CT data and considered within this study:

i) $stent_{AB}$ representing the stents in the as-built condition, ii) $stent_{HT}$ representing the stents in the heat treated condition and iii) $stent_{EP\text{-}HT}$ representing the stent in the electropolished and heat treated condition. For the 3D reconstruction of the stents, the X-ray CT images were manually segmented based on their grayscale values using the threshold segmentation tool within the 3D segmentation software Simpleware ScanIP[7]. Pores were explicitly considered as voids within the struts (figure 6.3, magenta areas at bottom row). After the 3D reconstruction, the volume, surface area, porosity, and strut diameter were determined using the measurement tools within Simpleware ScanIP. The centerline of the stents was used to measure the strut diameter based on the best fit circle perpendicular to the centerline. Then, a FE mesh of each 3D reconstructed L-PBF stent was created in Simpleware ScanIP and subsequently imported into the FE solver Abaqus/Explicit 2019. Besides the reconstructed stent models, the idealized CAD model $stent_{CAD}$ on which the L-PBF stents are based, was further considered in this study which allows for the comparison between the actual and as-designed mechanical response of L-PBF stents. The basic morphology of the investigated L-PBF stents is given in figure 6.3.

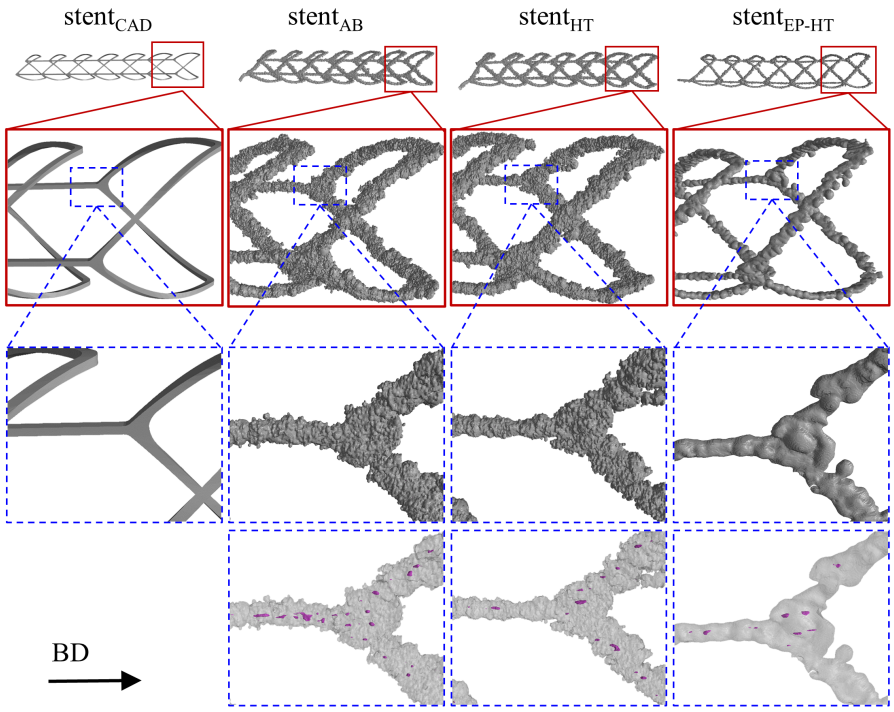

Figure 6.3: Investigated stent configurations. (from left to right): idealized CAD model, $stent_{AB}$ in the as-built, $stent_{HT}$ in the heat treated condition, and $stent_{EP-HT}$ in the electropolished and heat treated condition. The L-PBF stents are reconstructed based on X-ray CT data. Pores within the struts are illustrated in magenta (bottom row). The build direction (BD) is indicated by an arrow, adopted from Wiesent et al. [139].

Due to the high geometric complexity, the three L-PBF stents were modeled with linear tetrahedral elements with an element size of 0.02 mm (Abaqus element type C3D4). The as-

[7]Simpleware ScanIP: Synopsis®, Mountain View, California, USA

designed CAD model $\text{stent}_{\text{CAD}}$ of the L-PBF stents was meshed with eight node linear brick elements with reduced integration and hourglass control with an element size of 0.02 mm (Abaqus element type C3D8R). An overview of the investigated stent models and their discretization are given in table 6.2, and the investigated meshes are exemplary highlighted in figure 6.4.

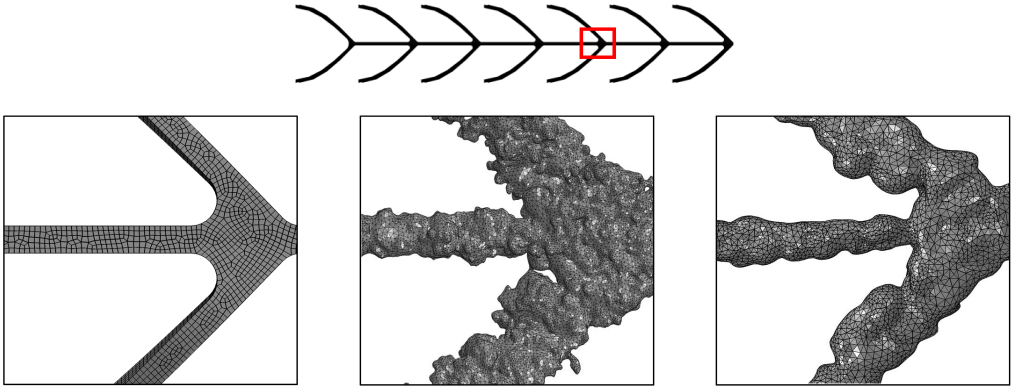

Figure 6.4: Illustration of the discretization of the stent models, adapted from Wiesent et al. [139]. Magnified view of mesh for (a) the idealized CAD model stent_{CAD}, (b) stent_{AB} in the as-built condition (also representing stent_{HT} due to similar morphology) and (c) stent_{EP-HT} in the electropolished and heat treated condition.

Table 6.2: Investigated stent models and their discretization, adopted from Wiesent et al. [139]

Model	Stent configuration description	Element type	Number of elements
$\text{stent}_{\text{CAD}}$	Intended stent design, CAD model	C3D8R	175 790
stent_{AB}	Reconstructed L-PBF stent, AB	C3D4	4 248 831
stent_{HT}	Reconstructed L-PBF stent, HT	C3D4	2 867 569
$\text{stent}_{\text{EP-HT}}$	Reconstructed L-PBF stent, EP-HT	C3D4	1 284 450

AB: as-built condition; HT: heat treated condition; EP-HT: electropolished and heat treated condition

Material description

The as-built and heat treated material behavior of the stents is described by a von Mises plasticity model with isotropic hardening behavior. The elastic properties were approximated by a Young's modulus of E = 193 GPa and a Poisson's ratio of μ = 0.3 [75]. The plastic material properties were determined from the uniaxial tensile test by transferring the experimentally determined engineering stress-strain curves into true values. The flow curves were extracted until uniform elongation. Thereupon, strain hardening was considered by Hollomon's power law (equation 2.27:$\sigma_{y,H} = K_H(\bar{\varepsilon}^{pl})^{n_H}$) (figure 6.5). Corresponding Hollomon power law parameters for the as-built condition are K_{AB}= 1157 MPa and n_{AB} = 0.35 and for the heat treated condition are K_{HT} = 1257 MPa and n_{HT} = 0.44. The flow curves were implemented in tabular form in Abaqus/Explicit and assigned to the respective stent models.

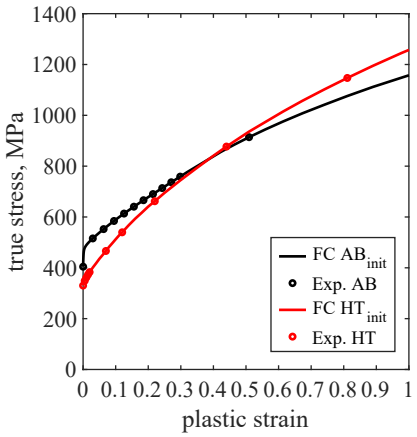

Figure 6.5: Flow curves derived from the results of the uniaxial tensile test for L-PBF flat specimens, adopted from Wiesent et al. [139]. The tensile specimens have a thickness of t = 1.0 mm. The flow curve representing the as-built (AB) condition is indicated by the black line and the flow curve representing the heat treated (HT) condition by the red line. The experimental data points are marked by spheres.

Stent compression simulation

The top and bottom plate of the compression test were implemented as analytical rigid surfaces. The reconstructed stents were positioned analogously to the experimental setup, with the longitudinal struts being aligned centrally and parallel to the plates. Stent compression was initiated by applying a linearly increasing displacement of u_{trans} = 2.0 mm in the negative vertical direction to the upper plate. The bottom plate was encastred by constraining all translational and rotational degrees of freedom ($u_{trans} = u_{rot} = 0$). Contact between the plates and the stent, as well as stent self-contact, were invoked using the general contact algorithm (friction-less: $\mu = 0$, penalty method) within Abaqus/Explicit. The simulation set-up is illustrated in figure 6.6.

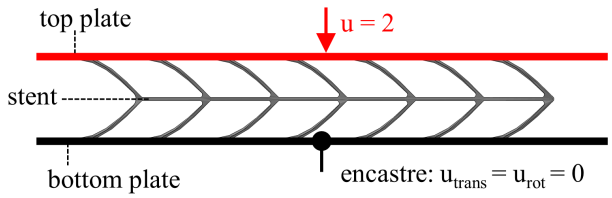

Figure 6.6: Illustration of the set-up of the stent compression simulation, adopted from Wiesent et al. [139].

An overview of the L-PBF stent compression simulations (virtual test matrix) is given in table 6.3. Each stent model was assigned the material properties that correspond to its respective material state (as-built, heat treated). For the $\text{stent}_{\text{CAD}}$, both material states were considered to provide a reference for comparing the intended and the actual L-PBF stent behavior.

Table 6.3: Overview of the models used in the stent simulations, adopted from Wiesent et al. [139].

Model	Stent configuration description	Material condition	Porosity
$stent_{CAD,AB}$	Idealized CAD stent	as-built	no
$stent_{CAD,HT}$	Idealized CAD stent	heat treated	no
$stent_{AB}$	Reconstructed L-PBF stent, as-built (AB)	as-built	yes
$stent_{HT}$	Reconstructed L-PBF, heat treated (HT)	heat treated	yes
$stent_{EP\text{-}HT}$	Reconstructed L-PBF, electropolished and heat treated (EP-HT)	heat treated	yes

AB: as-built condition; HT: heat treated condition; EP-HT: electropolished and heat treated condition

Stent crimping and expansion simulations

For the analysis of stent crimping and expansion, the previous validated FEA of conventionally manufactured stents (chapter 4, Wiesent et al. [10]). In addition to the actual analysis of the expansion behavior, the applicability of methods/models already established in the field of conventional laser-cut stents to L-PBF stents can be investigated. $Stent_{AB}$ and $stent_{HT}$ represent L-PBF stent morphologies without surface treatment and thus present a similar morphology and geometrically induced stiffness. $Stent_{EP\text{-}HT}$ represents the stent morphology after surface treatment (electropolishing), resulting in a smoothing of the strut surfaces, a reduction of the strut diameter and thus a reduction of the geometrically induced stiffness. It is, therefore, expected to have a different expansion behavior compared to the stents without surface treatment. Again, the expansion simulations of the CAD stent ($stent_{CAD}$) were performed for both material conditions (as-built, heat treated) to determine the differences between the actual and as-designed expansion behavior. Since the investigated stent models were identical to those used in the stent compression simulation, it is referred to table 6.3 (virtual test matrix) for an overview of the stent crimping and expansion simulation.

6.2 Results and Discussion

In this section the effects of L-PBF and post-processing steps on stent morphology and mechanical behavior of L-PBF 316L stents under compression are presented and discussed. Subsequently, the influence of the size effect on the mechanical behavior of L-PBF 316L is derived and discussed by comparing the numerically predicted compression behavior of the stents using bulk material properties (derived from the tensile specimens) with the experimentally determined data. Thereupon the results of the numerical analysis of stent compression and expansion of the reconstructed L-PBF stents are presented and compared to those of the intended CAD stent models. Finally, the limitations and further aspects of the work are discussed.

6.2.1 Morphological analysis

The basic morphology of the L-PBF stent configurations has already been shown in figure 6.3. The L-PBF stents show the typical process-related geometric irregularities similar to L-PBF lattice structures, e.g. surface roughness, deviation in the strut cross sectional shape and the strut diameter, strut waviness, tapers, and porosity [25, 34–37, 85, 88, 141]. These geometric irregularities are attributed to the layer-by-layer manufacturing, local energy input and melting of the powder, different heat dissipation properties of the powder and the solidified material, as well as L-PBF process parameters [28, 85–88, 142]. In the following, the individual irregularities are described in detail and their causes discussed.

Strut cross sectional shape

The L-PBF struts have a circular cross section instead of exhibiting the intended quadratic cross sectional shape of the stent CAD model (figure 6.7). This observation is in accordance to the findings of Finazzi et al. [31] on L-PBF CoCr stents. Due to the small structure size, the stent struts are only exposed in one hatch. The circular cross sectional shape can thus be attributed to the laser spot and the melt pool geometry. Due to the high surface roughness, the contour of the cross section of the stents without surface treatment ($stent_{AB}$, $stent_{HT}$) further appears non-uniform in contrast to the electropolished stent ($stent_{EP\text{-}HT}$).

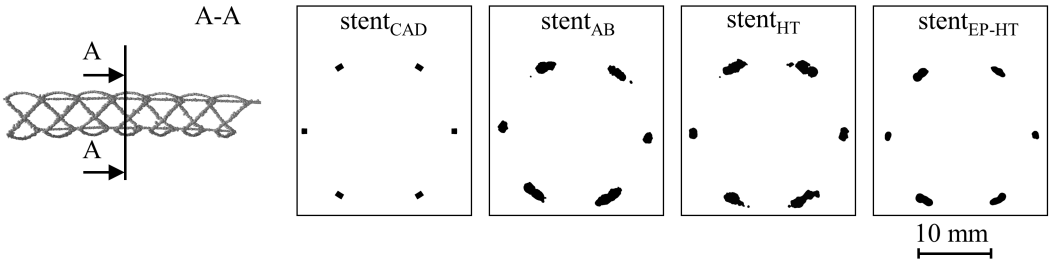

Figure 6.7: Deviation in strut shape between the as-designed and actual L-PBF stents, adopted from Wiesent et al. [139]. $Stent_{CAD}$ correspond to the morphology of the as-designed stent CAD model. $Stent_{AB}$, $stent_{HT}$, and $stent_{EP\text{-}HT}$ correspond to L-PBF stents in the as-built (AB), heat treated (HT), and electropolished and heat treated (EP-HT) conditions, respectively.

Surface roughness and strut waviness

L-PBF stents without surface treatment ($stent_{AB}$, $stent_{HT}$) have high surface roughness caused by partially melted and adhering powder particles on the strut surface, regardless of the material condition (as-built, heat treated) (figure 6.8: ①②). Surface roughness and strut waviness are mainly attributed to stacked solidified melt pools (sphere-pile-like defects) and adhering or partially melted powder particles [28, 85, 86]. These sphere-pile-like defects result from the layer-by-layer manufacturing process (staircase effect) and from discontinuous melting tracks

due to insufficient control of the exact position of the melt pool at such small strut diameters [88]. The adhesion of powder particles is attributed to thermal diffusion caused by the high temperature gradient between the powder material and the solidified struts [28]. At the strut edge, the powder is occasionally not completely melted, resulting in partially melted powder particles adhering to the strut surface [28, 86].

Material ablation during electropolishing results in the removal of these adherent powder particles and the compensation/rounding of local protrusions without extensively alternating the cross sectional shape. However, strut waviness and significant deviation in cross section cannot be fully compensated for via electropolishing (figure 6.7 and 6.8: ⑤⑥).

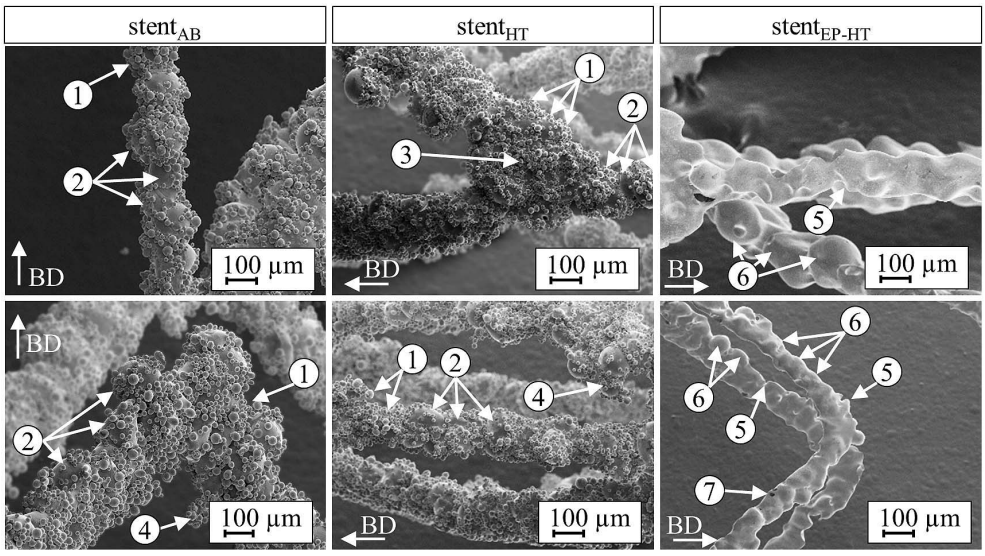

Figure 6.8: Scanning electron microscopy images highlighting the geometric irregularities related to the laser powder bed fusion process, adopted from Wiesent et al. [139]. Stent$_{AB}$, stent$_{HT}$ and stent$_{EP-HT}$ correspond to L-PBF stents in the as-built (AB), heat treated (HT), and electropolished and heat treated (EP-HT) conditions, respectively.

Strut thickness and dimensional error

The strut thickness of the L-PBF stents is overall increased and irregular over the strut length; although, local reduced diameters/tapers and notches occur (figure 6.3 and 6.8: ⑤). For the struts inclined relative to BD, even larger strut diameters and an increased number of adhering powder particles are observed (table 6.4, figure 6.8). In relation to the as-designed stent$_{CAD}$, the strut diameter is increased by about 2 and 2.6 times for the longitudinal struts and inclined struts, respectively, of the L-PBF stents without surface treatment (stent$_{AB}$, stent$_{HT}$) and by about 1.3 and 2 times for the longitudinal struts and inclined struts, respectively, of the electropolished

$stent_{EP\text{-}HT}$. Further, material accumulations occur at the nodes between inclined and longitudinal connecting struts (figure 6.8: ③).

The increased strut diameter can be attributed to the fact that the melt pool has a larger diameter than the original laser spot [88, 89]. For struts that are inclined relative to BD, this effect is exacerbated by the staircase effect and the overmelting of the downward facing strut side [85, 87]. The overmelting of the downward facing side is due to lower thermal conductivity of the powder compared to the bulk material. The heat is therefore preferably dissipated via the solidified strut. As inclined struts are partially built on powder, heat accumulation occurs on the downward facing side, which leads to overmelting, the formation of dross and spatter, and the adhesion of powder particles [85, 87] (figure 6.8).

All of these irregularities result in an overall increase of the L-PBF stent mass and surface area compared to the as-designed stents. The stents without surface treatment ($stent_{AB}$, $stent_{HT}$), thus, have about 4.3/4.4 times, and the electropolished $stent_{EP\text{-}HT}$ about 2.4 times, the mass of the as-designed $stent_{CAD}$ (table 6.4). The mass of the as-designed $stent_{CAD}$ was determined in Abaqus under the assumption that the stent has no internal porosity and a material density of $\rho = 9700$ kg/m^3.

Table 6.4: Analysis of the basic morphological parameters of the L-PBF stents, adapted from Wiesent et al. [139]

Model	D_{stent}, mm	$D_{strut,long}$, μm	$D_{strut,inc}$, μm	Mass, mg	Porosity, %
$stent_{CAD}$	3.00	quadratic 100 x 100		9.6	—
$stent_{AB}$	3.22	200 ± 25	250 ± 60	41.2	0.17
$stent_{HT}$	3.20	210 ± 35	260 ± 110	42.1	0.18
$stent_{EP\text{-}HT}$	3.20	130 ± 30	200 ± 70	22.3	0.20

AB: as-built condition; HT: heat treated condition; EP-HT: electropolished and heat treated condition

Porosity

The average internal porosity of the L-PBF 316L stents determined from X-ray CT data, is about 0.17 to 0.2 % thus implying high densification ($\rho \geqq 99$ %) (table 6.4). The average pore size was 31 μm with a minimum pore size of 8.5 μm. The minimum pore size corresponds to the minimum resolution of the CT (voxel size 8.5 μm) thus neglecting the presence of smaller pores, e.g. gas pores. Porosity is a well-known characteristic of AM commonly related to entrapped gas, lack of fusion, unmelted or partially melted particles and delamination between the layers [130, 131]. Although the determined porosity is low, pores must be considered critical due to their strength-reducing effect and their negative impact on fatigue strength, especially since the pore size is of the same order of magnitude as the stent struts [25, 143]. The occurrence of pores is almost unavoidable in L-PBF. To minimize porosity, further comprehensive studies are required that investigate the effect of machine-to-machine variability, powder characteristics, and process parameters.

Further considerations: Process parameters and stent design development
Experimental studies on L-PBF lattice structures have shown that the extent of the morphological irregularities depends strongly on the process parameters used, such as laser power and scanning speed [142]. Increased laser power, in combination with a reduced scanning speed, is related to larger melt pool diameters due to increased overmelting. This, in turn, leads to an increase in strut diameter and an intensification of sphere/plate-pile defects. A reduced laser power in combination with a reduced scanning speed, on the other hand, is related to turbulent melt pool behavior and thus increased strut irregularities and waviness. In summary, L-PBF causes morphological deviations between the as-designed and actual structure, which have a very strong impact on the mechanical properties, especially for small structures, including the L-PBF stents investigated in this work. A part design based exclusively on the CAD models without taking the morphological irregularities into account could, therefore, lead to unintended mechanical response of the final L-PBF part, which is further discussed below.

6.2.2 Mechanical behavior of L-PBF stents under compression

The macroscopic mechanical behavior of the experimentally tested L-PBF stents under compression (figure 6.9) corresponds to the characteristic deformation behavior of metal foams [144], with an initial linear-elastic region, followed by high plastic deformation characterized by a plateau with only a small gradient and subsequent densification characterized by a high gradient. The L-PBF stents in the as-built condition (figure 6.9: gray area) have the highest compressive strength, followed by the heat treated stents (figure 6.9: light red area) and the electropolished and heat treated stents $\text{stent}_{\text{EP-HT}}$ (figure 6.9: light blue area). Geometric irregularities have been found to cause an increase in the strut diameter D_{strut} and thus an increase in the section modulus S_{strut} of the struts[8] and the total stent mass. Because a detailed measurement of the strut diameters was only performed on the reconstructed stents, the average mass $\bar{m}$ of the respective stent configuration is provided in the legend of figure 6.9 and in table 6.5 for comparison purposes. The strut thickness is thus deduced based on the constant topology and the comparable mass of the respective stent configuration. The radial force at 50 % compression $F_{\text{rad.50 \%}}$ (i.e. a uniaxial displacement of u = 1.5 mm for an initial intended outer stent diameter of D_o = 3 mm) which is commonly used for the assessment of the radial strength of stents [140], is presented in table 6.5. With radial forces of $F_{\text{rad.50 \%}} = 2.39 \pm 0.23$ N, the electropolished and heat treated stents exhibit similar values as reported for conventional stents such as the PROMUS Element^{TM}[9] ($F_{\text{rad.50 \%}} = 2.89 \pm 0.28$ N) or the Xience Prime[10] ($F_{\text{rad.50 \%}} = 2.73 \pm 0.24$ N) [145].

[8] Section modulus of a strut with a circular diameter: $S_{strut} = \pi D_{strut}^3/32 \approx 0.1 D_{strut}^3$
[9] PROMUS Element, Boston Scientific Corporation, Marlborough, USA
[10] Xience Prime, Abbott Laboratories, Chicago, USA

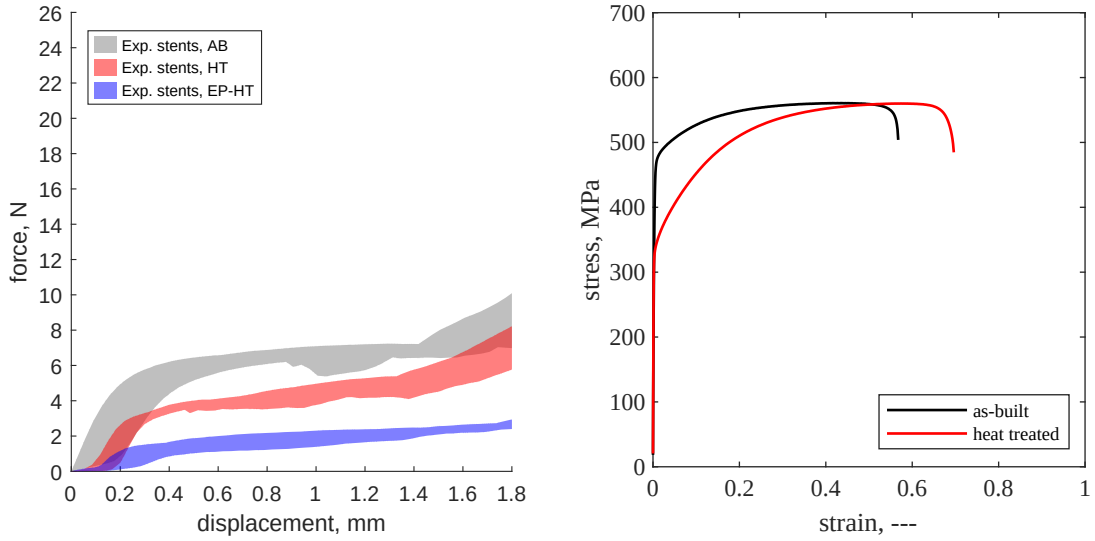

(a) *(b)*

Figure 6.9: Results of the L-PBF stent compression test and the uniaxial tensile tests on L-PBF tensile specimen, adopted from Wiesent et al. [139]. (a) Experimental determined mechanical response of L-PBF stents under compression. The shaded curve areas show the experimental results of the compression tests of the respective stent configuration (as-built stents (AB, gray area), heat treated stents (HT, light red area), electropolished and heat treated stents (EP-HT, light blue area). To indirectly consider the impact of the geometrically induced stiffness, the mean mass of the respective stent configuration is provided in the legend. (b) Stress-strain curves determined from uniaxial tensile tests on L-PBF 316L flat tensile specimen with a thickness of t = 1.0 mm in the as-built and heat treated condition.

As the investigated stents exhibit basically the same topology, the observed difference in radial strength are attributed to the different geometrically induced stiffness and the material condition of the respective L-PBF stent configuration.

The stents in the heat treated condition (figure 6.9: light red area) and the stents in the electropolished and heat treated state (figure 6.9: light blue area) feature the same material condition. The L-PBF stents are composed of solidified polycrystalline material. Therefore, material removal by electropolishing does not alter the material related stiffness of the stent, since the strength of the removed material is equal to that of the remaining stent material. The increased stiffness of the heat treated stents without surface treatment is therefore mainly due to their increased geometrically induced stiffness resulting from the increased strut diameter due to geometric irregularities discussed above. Electropolishing results in a smoothing of the strut surface by removing or reducing adhering and partially melted powder particles, as well as larger protruding surface features. Therefore, the strut diameter and thus the geometrically induced stiffness are reduced and the deformability of the stent is increased. During stent compression, deformation occurs predominantly in the inclined struts. With an average diameter of $D_{\text{strut,inc}}$ = 200 μm, the

Table 6.5: Experimentally determined radial force at 50 % compression $F_{rad.50\,\%}$ and the corresponding mass m of the respective stent configuration, adopted from Wiesent et al. [139]

Stent configuration	$F_{rad.50\,\%}$, N	m, mg
as-built	7.11±0.63	42.3±0.9
heat treated	5.87±0.49	42.1±0.5
electropolished and heat treated	2.39±0.23	24.5±1.5

inclined electropolished struts exhibit only 45 % of the section modulus $S_{\text{strut, EP-HT}}$ of the stent struts without surface treatment ($D_{\text{strut,inc}}$ = 260 μm) which causes the reduction of the radial force $F_{\text{rad.50 \%}}$ of the electropolished stents by approximately 41 % compared to the solely heat treated stents.

Due to their similar morphology, the stents in the as-built (stent_{AB}) and the stents in the heat treated condition (stent_{HT}) have similar strut diameters and thus similar geometric induced stiffness. The reduced radial strength of the heat treated stents (figure 6.9, light red area) is therefore attributable to alterations in material properties following heat treatment. The applied heat treatment was aimed at reducing the yield strength and increasing the ductility to enable stent crimping and expansion. In the as-built condition, material comprising the L-PBF 316L stent shows almost ideal elastic-plastic behavior. In the heat treated condition, reduced yield strength and increased hardening behavior are present (figure 6.9b). These observations are consistent with findings in the literature and are therefore only briefly discussed [38, 146].

The different mechanical properties between as-built and heat treated condition are attributed to differences in the microstructure and to the relief of residual stresses after heat treatment [8, 38, 82]. In the as-built condition, a microstructure typical for L-PBF is observed, consisting of overlapping melt pools, coarse elongated grains, and the presence of a substructure (figure 6.10a). The substructure is classified in literature as δ-ferrite, a strength-enhancing second phase [70]. Due to the high temperature gradients and densification rate, high dislocation densities and residual stresses occur in the as-built condition of L-PBF materials causing the material to undergo saturation with respect to strain hardening [76, 77, 80]. During heat treatment, the dislocation density is decreased, the residual stress are relieved and the dislocations act as nucleation points for recrystallization [38, 40, 80, 82]. The recrystallized microstructure is characterized by rather equiaxed coarse grains (figure 6.10b), causing the reduction in yield strength [38]. Besides recrystallization, the heat treatment of L-PBF 316L is associated with the reduction/dissolution of the δ-ferrite phase as a strength-enhancing second phase, which explains the reduced yield strength [38].

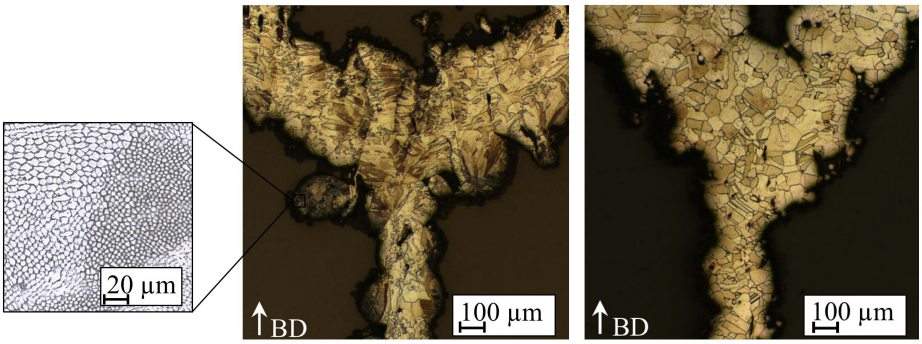

(a) *(b)*

Figure 6.10: Metallographic sections of a L-PBF stents, adopted from Wiesent et al. [139]. (a) L-PBF stent in the as-built condition highlighting the observed substructure and (b) L-PBF stent in the heat treated condition

6.2.3 Numerical analysis of the compressive behavior of L-PBF stents

Impact of size effect on the mechanical behavior of L-PBF stents

The numerical analysis of stent compression was initially investigated using the L-PBF 316L flow curves determined from flat specimens (figure 6.5 and 6.12a: L-PBF 316L AB_{init}, HT_{init}). The predicted force-displacement curves of the L-PBF stent compression simulations using theses flow curves showed large deviations from the experimentally determined curves (figure 6.11

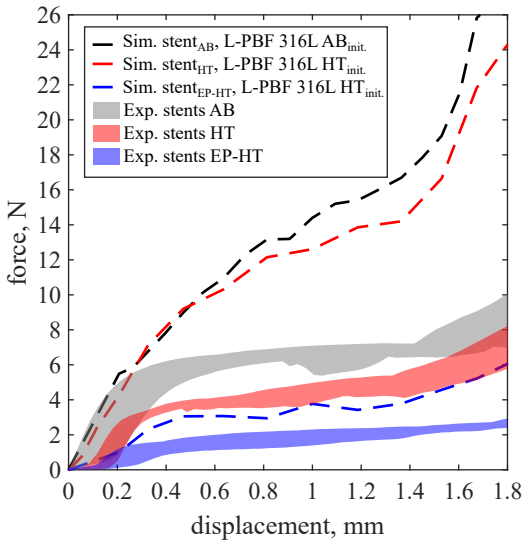

Figure 6.11: Mechanical response of L-PBF 316L stents using the initial flow curves determined from tensile tests, adopted from Wiesent et al. [139]. $Stent_{AB}$, $stent_{HT}$ and $stent_{EP-HT}$ correspond to the reconstructed stents in the as-built (AB), heat treated (HT), and electropolished and heat treated (EP-HT) conditions and, respectively. The experimental determined response of the selectively laser melted stents is illustrated by the shaded curve areas.

These deviations can be attributed to the size effect that has also been observed for L-PBF lattice structures [25, 33, 128]. The size effect is caused by the differences in microstructure due to different thermal histories of small and large L-PBF structures, as well as large surface-to-volume-ratio, the increasing defect density, and surface roughness of smaller structures [33, 128]. The determination of the exact origin of the strength-reducing mechanisms was not investigated in this study. However, it has been shown that the size effect has a strong influence on L-PBF 316L and has to be considered within the development of L-PBF stents.

Due to the size effect, the mechanical properties of L-PBF stents (strut thickness of t = 0.1 mm) cannot be approximated by the flow curves derived from tensile flat specimens (thickness of t = 1.0 mm). It is therefore necessary to adjust the properties of the L-PBF 316L stent material to meet the experimentally determined global stent response. In the literature, tensile test data are available for miniaturized L-PBF 316L specimens in the as-built condition with diameters comparable to the stent struts [119, 120, 147], but not for specimens after heat treatment. Thus, for reasons of consistency, the flow curves of the as-built and heat treated L-PBF 316L were adjusted within the FEA of stent compression until the numerically predicted and experimentally determined force-displacement curves for stent_{AB} and stent_{HT} match. To accomplish this, the yield strength was systematically reduced (figure 6.12a: L-PBF 316L AB_{mod}, HT_{mod}), assuming that the size effect has no influence on the hardening behavior of L-PBF 316L as been shown by Ravari et al. [25]. Yield strengths of σ_{yAB} = 271 MPa and of σ_{yHT} = 117 MP are determined to describe the L-PBF 316L stent material in the as-built and heat treated conditions, respectively. This corresponds to a reduction of yield strength σ_y by 41 % in the as-built and by 59 % in the heat treated condition compared to the initial material properties derived from the tensile tests.

To justify this modification, the determined L-PBF 316L flow curve in the as-built condition was compared with the flow curves obtained from experimental data of miniaturized L-PBF 316L tensile specimens from the literature [119, 120, 147] (figure 6.13 and table 6.6). The comparable strain hardening parameters of the flow curves justify the modification of the flow curve in the as-built condition. The observed strength reduction is further consistent with the findings of Ravari et al. [25] based on the mechanical behavior of single lattice struts with a diameter of D_{strut} = 200 μm in the as-built condition. They found a reduction in the yield strength σ_{yAB} of the single struts of about 25 % compared to the base material. The further decrease in strength observed in this study can be attributed to the large surface-to-volume ratio and the resulting high affinity for strength reducing effects due to surface irregularities.

Because no literature data on heat treated miniaturized L-PBF 316L tensile specimens were available, the flow curve of the L-PBF 316L stent material in the heat treated condition was verified by means of the compression simulation of the electropolished and heat treated stent. Therefore, after fitting material properties based on the mechanical response of stent_{HT} (heat treated condition), the same material properties are then applied in the simulation of $\text{stent}_{\text{EP-HT}}$

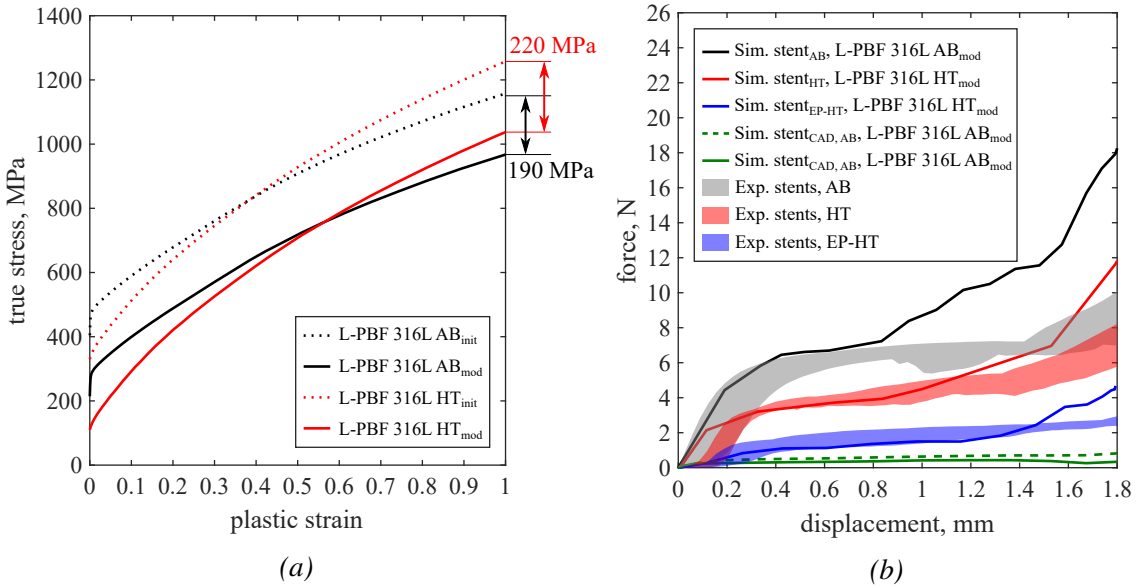

Figure 6.12: Mechanical response of L-PBF stents, adapted from Wiesent et al. [139]. (a) Modification of the initial flow curves which were derived from flat tensile test to allow for the description of the L-PBF 316L stent material in the as-built and heat treated condition. (b) Comparison of the experimental determined global mechanical response of the stents under compression (shaded curve areas) with the numerical predicted response of the respective reconstructed stent model configuration (solid lines) using the modified flow curves (L-PBF 316L AB$_{mod}$, HT$_{mod}$). Stent$_{AB}$, stent$_{HT}$ and stent$_{EP-HT}$ correspond to the reconstructed stents in the as-built (AB), heat treated (HT), and electropolished and heat treated (EP-HT) conditions and, respectively. Stent$_{CAD,AB}$ and stent$_{CAD,HT}$ correspond to the as-designed stent CAD models with the as-built and heat treated material properties, respectively.

(electropolished and heat treated condition) to provide a validation of the adjusted material properties of the heat treated L-PBF stents. A good agreement with the experimentally determined force-displacement curves is achieved, thus verifying the adjusted flow curve (figure 6.12). The subsequent simulations were all performed using the modified flow curves.

As shown above, after adjusting the material properties, the macroscopic mechanical behavior of L-PBF stents under compression can be predicted by FEA (figure 6.10b). Within the FEA of the L-PBF stents, large differences between the actual (reconstructed) and the as-designed stent model were observed. As apparent from figure 6.10b, the numerical prediction based on the stent$_{CAD}$ leads to a significant underestimation of the compression strength compared to the reconstructed stent models, i.e., by a factor of 11 for the stents without surface treatment (stent$_{AB}$, stent$_{HT}$) and 4 for the stent with surface treatment (stent$_{EP-HT}$). The increased stiffness of the actual L-PBF stents can be attributed to the increased geometrically induced stiffness of the stent struts resulting from the geometric irregularities and thus the increased strut diameter discussed above. It is further likely that the increased compression strength of the actual L-

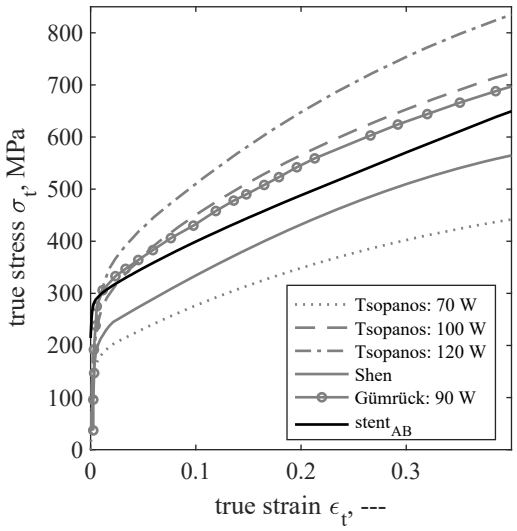

Figure 6.13: Comparison of the determined flow curve of the L-PBF 316L stent material with the flow curves from experimental data of miniaturized L-PBF 316L tensile specimens from the literature [119, 120, 147], adapted from Wiesent et al. [139].

Table 6.6: Comparison of the determined hardening parameter of the L-PBF 316L stent material in the as-built condition with hardening parameter obtained from experimental data of miniaturized L-PBF 316L tensile specimens from the literature [119, 120, 147], adapted from Wiesent et al. [139].

		$\sigma_t = K \cdot \varepsilon_t^{n_H}$	
		K_H, MPa	n_H
Tsopanos: 70 W	[147]	611	0.31
Tsopanos: 100 W	[147]	988	0.33
Tsopanos 120 W	[147]	1163	0.35
Shen	[119]	763	0.31
Gümrück: 90 W	[120]	973	0.35
stent_{AB}		1157	0.35

PBF stents depends not only on the overall global increase in mass, but also on the local mass distribution. In the L-PBF stent, material accumulations at the nodes (connecting points of the struts) are observed (figure 6.8). In these regions, the largest deformations generally occur during compression. Thus, the local increase in stiffness due to material accumulation at the nodes could contribute to the global increase in stiffness.

The absence of a force increase in the posterior part of the force-displacement curve also indicates that the $\text{stent}_{\text{CAD}}$, unlike the reconstructed stents, is not densified during the compression. With regard to the influence of the heat treatment, the compressive strength of the CAD stent model in the as-built condition ($\text{stent}_{\text{CAD,AB}}$, green dashed line) is increased when compared to the heat treated condition ($\text{stent}_{\text{CAD,HT}}$, green solid line). Again, given the relationship between the flow curves for the as-built and heat treated material condition (figure 6.10a), this trend is not

surprising.

Qualitative validation

For a further qualitative validation of the stent compression analysis, regions of the deformed stent models are compared to corresponding regions of the experimentally deformed stents images using both X-ray CT and SEM (figure 6.14). Based on the X-ray CT reconstructions (figure 6.14a), good agreement is observed between the numerically predicted and the experimentally compressed stent configurations. Minor deviations are attributed to deviations in the initial stent position between the plates or a slight side movement of the stent at the beginning of the compression. Furthermore, particularly deformed areas are identified using SEM and compared with the equivalent plastic strain $\bar{\varepsilon}^{pl}$ distribution determined in the simulation (figure 6.14b). Areas of large plastic deformation can be identified in SEM images by means of so-called flow lines indicated by a wavy surface near local crack formation, e.g. due to a pore close to the surface, or near nodes (connecting points of the struts). A good agreement between the predicted high local plastic deformation with a crack and with local flow lines is observed. Thus, the results of this qualitative validation suggest that the adjustment of the material properties (figure 6.12a) is appropriate.

Stress distribution within the L-PBF stent during compression

In terms of the von Mises equivalent stress distribution $\sigma_{e,vM}$, a significant reduction of $\sigma_{e,vM}$ is observed for the heat treated (figure 6.15b) compared to the as-built (figure 6.15a) stents. This trend is not surprising given the relation of the flow curves for the as-built and heat treated material condition (figure 6.12a). Due to the geometric irregularities, local stress peaks occur in the actual L-PBF stents with maximum stresses of $\sigma_{e,vM}$ = 883 MPa for stent_{AB}, $\sigma_{e,vM}$ = 813 MPa for stent_{HT} and $\sigma_{e,vM}$ = 341 MPa for $\text{stent}_{\text{EP-HT}}$. Although, due to the small structural size electropolishing cannot fully compensate for pre-existing strut waviness and tapers, it does serve to level out or round local protrusions. The smoothed surface therefore results in the observed reduced local stress concentrations that develop during stent deformation and thus can mitigate the formation of local damage/cracks. Studies on electropolished L-PBF 316L have also shown that smoothing the surface of L-PBF 316L increases fatigue life [148].

Although, electropolishing has been found to reduce stress concentration by reducing the impact of local process-related geometrical irregularities, it can cause local weakening of the stent or further reduce the local strut diameter in regions of pre-existing (process-related) reductions. In other words, although the electropolishing process is effective at removing large protruding features, it can also remove material from already reduced strut diameters, making this defect even more critical. In addition, near-surface defects such as pores can become exposed, which then act as surface notches during stent deformation (figure 6.14b). It is therefore essential

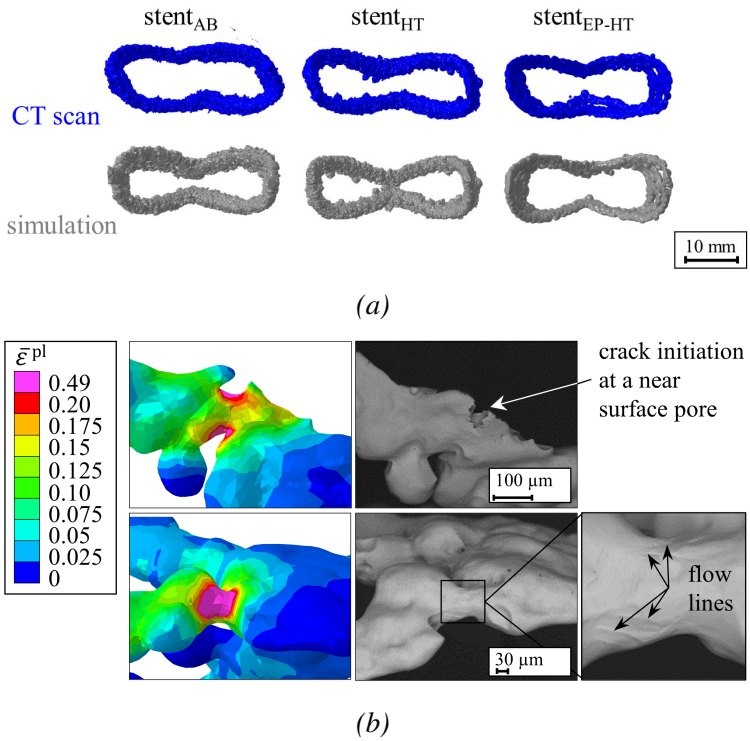

Figure 6.14: Qualitative validation of the uniaxial stent compression simulations, adapted from Wiesent et al. [139]. (a) Comparison of the numerically predicted deformed stent shape (gray) with the X-ray CT reconstructions of the corresponding experimentally compressed L-PBF stent (blue). (b) Comparison of scanning electron microscopy images with the equivalent plastic strain $\bar{\varepsilon}^{pl}$ in areas of large deformations for stent$_{EP\text{-}HT}$, near a surface crack (top row) and near strut nodes (bottom row). Stent$_{AB}$, stent$_{HT}$ and stent$_{EP\text{-}HT}$ correspond to the reconstructed L-PBF in the as-built (AB), heat treated (HT), and electropolished and heat treated (EP-HT) conditions, respectively.

to determine appropriate parameters for an effective electropolishing and to check the stents for exposed defects or drastically reduced strut cross sections after surface treatment. The electropolishing process should be adjusted to ensure surface treatment of all areas of the stent. In addition, the advantages and disadvantages of near-net-shape stent fabrication with subsequent low ablation by electropolishing should be compared to oversized stent fabrication with subsequent high ablation by electropolishing.

In terms of the von Mises equivalent stress distribution $\sigma_{e,vM}$, the L-PBF stents show a spatial variability of stress, while the CAD model (stent$_{CAD}$) has a smooth and more constant stress distribution (figure 6.15). At local geometric irregularities, such as notches and regions of reduced diameters, local stress peaks are observed in the L-PBF stents, in contrast to the CAD model. In the as-built material condition, stent$_{AB}$ has a maximum stress value of $\sigma_{e,vM}$ = 883 MPa; whereas, the CAD model stent$_{CAD,AB}$ has a maximum value of $\sigma_{e,vM}$ = 312 MPa. The maximum stresses for the heat treated L-PBF stent without (stent$_{HT}$) and with (stent$_{EP\text{-}HT}$) surface treatment

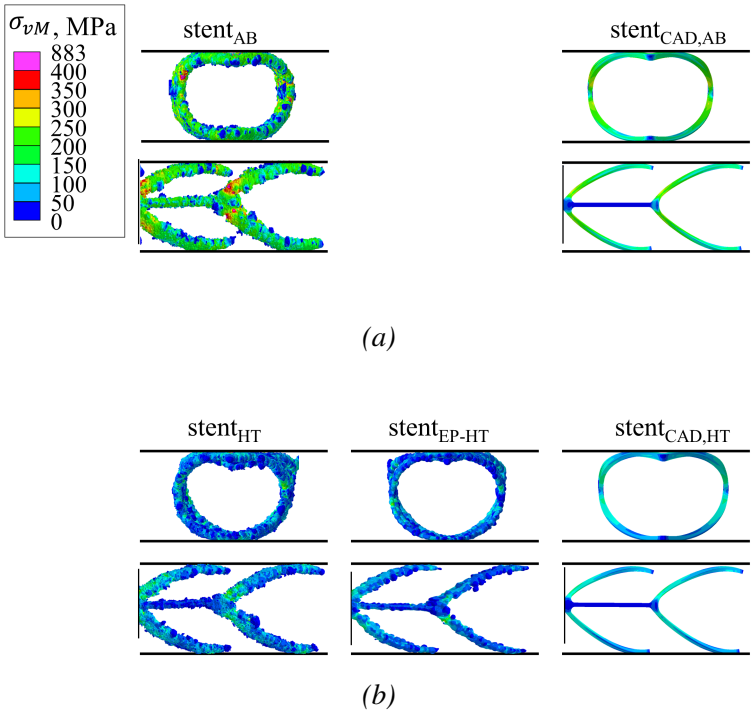

Figure 6.15: Contour plots of the von Mises stress $\sigma_{e,vM}$ on the outer surface of the L-PBF stents under a compression displacement of u = 0.8 mm, adapted from Wiesent et al. [139]. (a) Stents in the as-built and (b) in the heat treated material condition illustrated in the front (top row) and the side view (bottom row). Stent$_{AB}$, stent$_{HT}$ and stent$_{EP-HT}$ correspond to the reconstructed L-PBF stents in the as-built (AB), heat treated (HT), and electropolished and heat treated (EP-HT) conditions, respectively. Stent$_{CAD,AB}$ and stent$_{CAD,HT}$ correspond to the as-designed stent CAD models with the as-built and heat treated material properties, respectively.

are $\sigma_{e,vM}$ = 813 MPa and $\sigma_{e,vM}$ = 341 MPa, respectively; whereas, the CAD model stent$_{CAD,HT}$ has a maximum value of $\sigma_{e,vM}$ = 180 MPa.

6.2.4 Numerical analysis of the expansion behavior of L-PBF stents

Global deformation behavior of L-PBF stent during expansion

The expansion behavior of the L-PBF stents is shown in figure 6.16. Similar to stent compression, the geometrically induced stiffness of the L-PBF stents has a great influence on their expandability and, consequently, on safety during expansion.

The stents without surface treatment (stent$_{AB}$, stent$_{HT}$) have high stiffness and thus exhibit high resistance to balloon expansion. Despite very high pressure accumulation at the free balloon ends, the initial expansion of the stent ends is hardly present for the stents without surface conditioning (stent$_{AB}$, stent$_{HT}$). This pressure accumulation, in combination with the surface roughness of the L-PBF stents, which could potentially weaken the balloon during crimping due

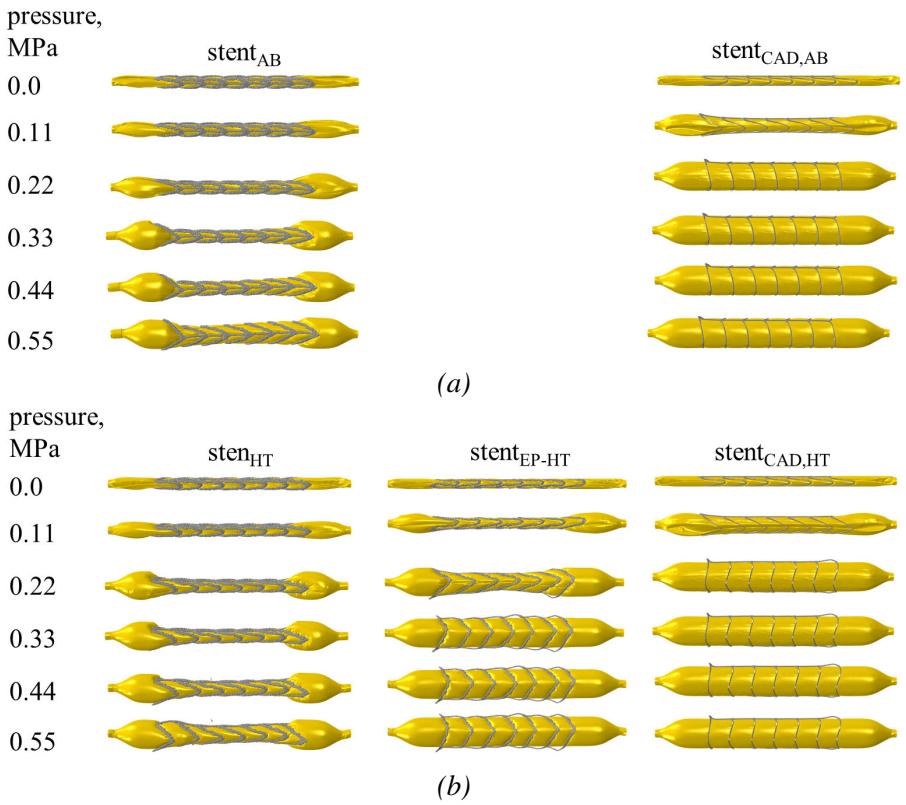

Figure 6.16: Predicted global deformation behavior of L-PBF stents during expansion, adopted from Wiesent et al. [139]. (a) Predicted expansion behavior of L-PBF stent in the as-built material condition. (b) Predicted expansion behavior ofL-PBF stent in the heat treated material conditions. Stent$_{AB}$, stent$_{HT}$ and stent$_{EP-HT}$ correspond to the reconstructed L-PBF stents in the as-built (AB), heat treated (HT), and electropolished and heat treated (EP-HT) conditions, respectively.

to protruding features, poses a potential risk for the balloon to burst. These effects can be largely mitigated by electropolishing, which is discussed below. A relatively homogeneous diameter increase over the entire stent length is observed for these stents starting at an expansion pressure of approximately $p \approx 0.55$ MPa.

The predicted expansion behavior of the electropolished and heat treated stent (stent$_{\text{EP-HT}}$), corresponds most closely to the inhomogeneous expansion behavior of conventional stents under the development of the so-called DB effect [10] (figure 6.17). Thereby, the crimped stent provides resistance to expansion, which causes the expansion pressure to accumulate at the free balloon ends. After exceeding a certain threshold value, the pressure is sufficient to expand the ends of the stent, making transient convex stent shape resemble a dogbone. The stent is then expanded towards its center as if by a wedge until the final cylindrical shape is reached. Besides reducing the accumulation of pressure at the balloon ends, electropolishing also reduces the risk of local balloon damage with the smoothing of the strut surface.

Similar to the compression analysis, significant differences between the expansion behavior of

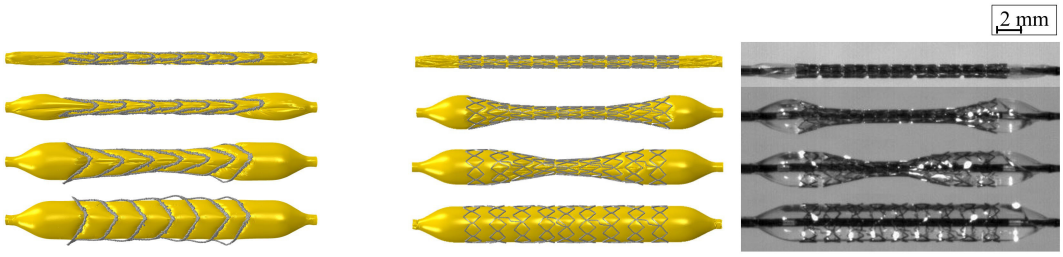

(a) *(b)*

Figure 6.17: Comparison of the expansion behavior of a L-PBF and a conventional laser-cut stent, adopted from Wiesent et al. [139]. (a) Predicted expansion behavior of stent$_{EP\text{-}HT}$ based on the the reconstruction of an electropolished and heat treated L-PBF stent from X-ray CT data. (b) Numerical predicted (left) and experimental determined expansion behavior of a conventional laser-cut stent based on Wiesent et al. [10].

the reconstructed L-PBF stents and as-designed CAD stents are observed. Due to its lower mass, the CAD stent has a lower radial stiffness and therefore offers less resistance to balloon expansion. Therefore, in contrast to L-PBF stents without surface treatment (stent$_{AB}$, stent$_{HT}$), no excessive pressure accumulation occurs at the free balloon ends during the expansion of the CAD stent. The CAD stent is also less stiff than stent$_{EP\text{-}HT}$, so the DB effect is less pronounced (figure 6.16). Further, full stent expansion occurs at half the expansion pressure as that for stent$_{EP\text{-}HT}$ and thus resulting in an underestimation of the necessary expansion pressure. Regarding the final expanded shape, stent$_{EP\text{-}HT}$ shows buckled stent struts, while the idealized stent has all struts properly conformed to the balloon contour.

Stress distribution within the L-PBF stents during expansion

The von Mises stress $\sigma_{e,vM}$ distribution shows the same trend as that discussed in the compression analysis (figure 6.15); thus, it is not explicitly visualized for each stent. Due to the geometric irregularities, the stresses are generally elevated and local stress peaks occur in the actual L-PBF stents compared to the CAD stent. Heat treatment again leads to a significant reduction of the stresses. The influence of geometric irregularities, e.g., notches, locally reduced diameters, and pores, on the development of local strain concentrations is exemplary demonstrated using the equivalent plastic strain $\bar{\varepsilon}_{eq}$ distribution within stent$_{EP\text{-}HT}$ (figure 6.18). In the expanded state, high strains occur preferably at locally reduced strut diameters/notches and at the stent spikes. The equivalent plastic strain locally exceeds a value of $\bar{\varepsilon}^{pl} > 0.3$, which corresponds to the uniform elongation of a conventional 316L and can therefore be associated with the onset of local damage. Pores within the struts lead to a local reduction of the effective strut cross section, which is critical in areas that are expected to undergo large plastic deformation (figure 6.18, sectional drawing A-A, B-B). Due to their strength-reducing effect, pores, and notches and in particular their superposition should be considered critical, as theses could lead to early local

failure. This is particularly critical in regions subjected to large deformations and especially for structures with a high surface-to-volume ratio. For stents, the transition area between the nodes and the struts, and the stent spikes, are particularly susceptible. The strength-reducing effect of these geometric irregularities can pose risks not only during the implantation process, but also during the long-term usage of the stent under the cyclic loading caused by changes in the blood pressure. A study on the influence of internal porosity and surface roughness on the fatigue behavior of L-PBF 316L round tensile specimens (diameter of $D = 4.5$ cm) has shown that at low load levels and a high number of load cycles to failure (high-cycle fatigue), damage initiates mainly at the surface; whereas, at high load levels and low number of cycles (low-cycle fatigue), damage is increasingly initiated by internal pores [143]. Transferred to L-PBF stent application, the impact of pores during the implantation process and the impact of surface roughness over the long-term application must, therefore, be regarded as critical. Further investigations are necessary to quantify the impact of these geometric irregularities on the damage and fatigue behavior of L-PBF stents.

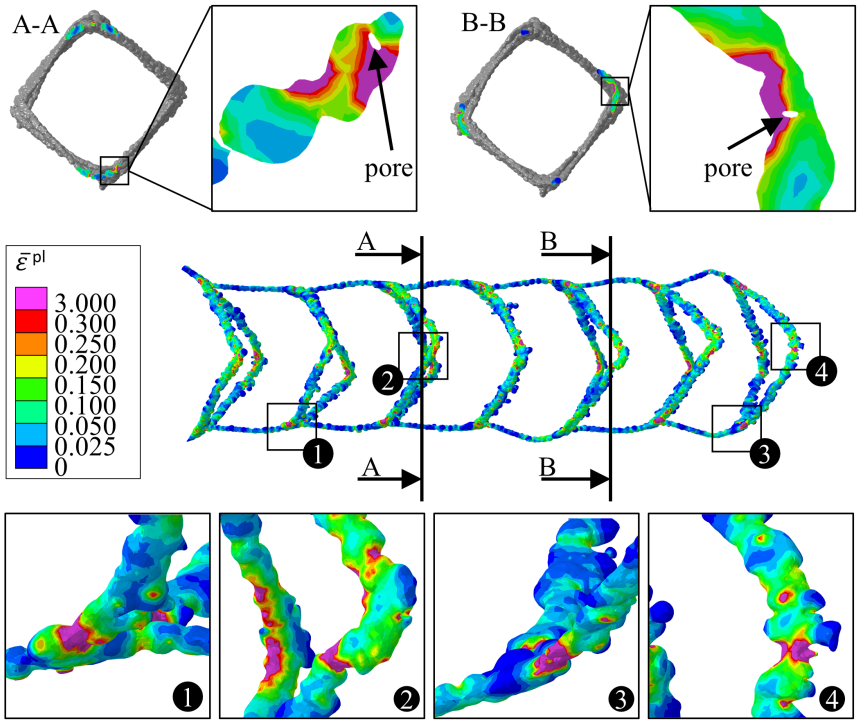

Figure 6.18: Influence of reduced strut diameters/notches and pores (section A-A, B-B) for the electropolished and heat treated stent ($stent_{EP-HT}$) in the area of large plastic deformation using the contour plot of equivalent plastic strain $\bar{\varepsilon}^{pl}$ distribution, adapted from Wiesent et al. [139].

Regarding the von Mises stress $\sigma_{e,vM}$ distribution, the comparison of the stress distribution within the CAD model ($stent_{CAD}$) with the actual L-PBF stents shows same trend as described in the compression analysis. Therefore, due to the geometric irregularities, the stresses are generally elevated and local stress peaks occur in the actual L-PBF stents compared to the CAD stent.

6.2.5 Limitations and scope for future research

Stent manufacturing via L-PBF presents a major challenge. In this study, L-PBF stents with a strut diameter of D = 200 μm could be realized using a conventional commercial L-PBF machine, however, with a variety of geometrical imperfections. In a follow-up study, the challenges identified here will be addressed by using a μ-L-PBF machine with a smaller laser spot size, a different recoating strategy, a smaller powder particle size and a related comprehensive process parameter study, as proposed by Nagarajan et al. [137].

Furthermore, the inverse determination of the material properties of the stent should be discussed. The determination of material properties on miniaturized tensile specimens has been omitted in this study due to significant challenges associated with specimen preparation (e.g, large aspect ratios between strut diameter and length), experimental testing (e.g., clamping, inaccuracy of strain measurement), and determination of specimen dimensions (e.g. determination of specimen cross section) [147]. In the literature, data are available for L-PBF 316L struts in the as-built state, but not in the heat treated condition [120, 147, 149]. Therefore, for consistency reasons, the flow curves were inversely determined from the experimentally determined global response of the stent under compression using FEA. The verification of the flow curves with literature data (as-built condition) and the implementation of the determined flow curve in the FEA of a further stent morphology ($\text{stent}_{\text{EP-HT}}$, heat treated condition) show that this approach is justified (figure 6.12b, figure 6.13). In a follow-up study, the material properties of the L-PBF stents should be determined by means of comprehensive experiments on miniaturized tensile specimens specimens, together with the optimization of the L-PBF process. This would improve the accuracy of the method for numerical analysis of the L-PBF stents presented here.

In this study, heat treatment was primarily used to increase the deformability of the stents to enable their crimping and expansion. Studies in literature have found that the corrosion resistance of L-PBF 316L is inferior to that of wrought 316L, but also that it improved by heat treatment [40]. Since the corrosion resistance is essential biocompatibility of the stents, further studies are necessary to improve the corrosion behavior of L-PBF 316L stents by adequate heat treatment.

There are several modeling assumptions made in this work that merit further discussion. In addition to assumptions made regarding the boundary conditions and the material model, the accuracy of the FEA results is mainly influenced by the fidelity of the morphological representation of the investigated structure. The L-PBF stent morphologies are based on reconstruction from X-ray CT data with a voxel size of 8.5 μm. In general, a minimum width of three voxels is required for structures to be reliably captured by CT [150]. Therefore, only pores and adherent powder particles with a diameter of more than $D_{pore} > 25.5$ μm are considered within this study. Adhering powder particles are either neglected based on the aforementioned size threshold or are

modeled as completely fused to the strut surface, making them load-bearing, in contrast to reality. The latter modeling assumption artificially increases the local strut thickness. Combined with the omission of very small pores, this can lead to a possible increase in global stent mass stiffness. Therefore, the inversely determined yield strength of the material comprising the L-PBF 316L stent might slightly underestimate the actual value to compensate for the artificially increased predicted compression strength.

The L-PBF process is also associated with an anisotropic material behavior. In this study, the material behavior of the stent was considered isotropic and homogeneous assuming that the geometric effects (e.g., stent design, process-related geometric irregularities) outweigh the influence of material anisotropy with respect to the macroscopic mechanical behavior [65]. Although this approach is well established for L-PBF lattice structures [25, 147, 151, 152], the direction-dependent properties of the stent should be further investigated (e.g. influence of the strut orientation to BD) and should be considered within the material description.

The aim of this study was not to determine the exact material properties of L-PBF 316L stents. However, this work has shown that the size effect has a significant influence on the mechanical properties of L-PBF 316L and therefore must be considered for the design of filigree L-PBF structures. Furthermore, a methodology is presented that enables the determination of the material properties of L-PBF stents and thus allows to investigate their mechanical behavior more accurately within FEAs. Besides the size effect, the mechanical properties of L-PBF metals are influenced by a variety of factors such as powder or L-PBF process parameters, which causes variations in the mechanical properties of the same part in different batches.

In this study, heat and surface treatment has been found to be critical factor for the feasibility of stents expansion. Therefore, further experimental studies are required to identify adequate heat and surface treatments. For L-PBF metals, heat treatment is further associated with an increase in fatigue properties [146]. However, as damage and fatigue properties are strongly influenced by surface roughness, internal defects, and structural size, further numerical and experimental studies are required to make more quantitative statements regarding the long-term performance of L-PBF stents. In this context, the biocompatibility of L-PBF 316L should also be investigated more closely.

It has also been shown that the numerical analysis of L-PBF stents based on the as-designed CAD model is not suitable in its current form. Since numerical stent analysis based on reconstructed CT data is very complex and computationally intensive, a method for the creation of synthetic stents based on statistical methods, e.g., as described by Ravari et al. [25] for L-PBF lattice structures, should be developed.

6.3 Conclusions

In this chapter, the impact of L-PBF process-related geometrical irregularities, the size effect, heat treatment, and surface treatment on the mechanical response of L-PBF stents was investigated using a combined experimental and computational framework based on the reconstruction of actual L-PBF stents. The following conclusions are drawn:

- Considering the extent of process-related geometric irregularities (e.g., strut waviness, pores, notches, deviations in strut diameter,) is essential for the development and evaluation of L-PBF stents. Such irregularities can lead to significant deviations in the morphology and thus the mechanical properties of L-PBF stents compared to as-designed (idealized) stents.
- L-PBF process-related geometric irregularities lead to a significant increase in the strut diameter and thus in the geometric resistance of the actual L-PBF stents, which can be partially reduced by surface treatment such as electropolishing.
- Surface treatment (viz., electropolishing) of L-PBF stents is essential to achieve a radial compression strength and thus a stent expansion behavior comparable to that of conventional stents. Proper electropolishing serves to smooth the strut surface, reduce excessive material volume caused by the L-PBF process, reduce stent stiffness, and increase global deformability, thus reducing the risk of balloon damage/bursting during expansion.
- Adequate heat treatment of the L-PBF stent is essential to improve the ductility of the stent, to reduce global stress and, in combination with surface treatment, to reduce local stress concentrations, which could help to mitigate the risk of stent damage during implantation and cyclic loading.
- The size effect has a significant influence on the material properties of L-PBF 316L, manifested by a reduction in the yield strength of material comprising filigree L-PBF 316L structures by 41 % in the as-built and by 59 % in the heat treated condition compared to bulk material. This size effect should be considered for accurate prediction of L-PBF stent behavior.
- For a numerical analysis of L-PBF stents a reconstruction or statistical consideration of process-related irregularities is essential. Otherwise, the radial stiffness of the stents is underestimated, and possible local stress concentrations are neglected.
- To further improve stent morphology and mechanical behavior, further studies with dedicated μ-L-PBF machines and comprehensive process parameter studies are required.

7 Comprehensive discussion

This work aimed to develop a method for numerical analysis of coronary L-PBF stents. With the current state of the art of L-PBF, significant deviations between the morphology of the actual L-PBF stent geometry and the intended stent geometry (CAD model) occur. Common approaches for numerical analysis of conventionally manufactured coronary stents, particularly with respect to stent model generation as well as the characterization and modeling of the stent material, are therefore not suitable for the analysis of L-PBF stents. Based on the methodology proposed in this doctoral thesis, the numerical analysis of L-PBF stents was possible for the first time. In this way, the impact of individual geometric effects and loading conditions can be studied in more detail and necessary modifications in stent design, L-PBF process, and post-processing can be identified, thus extending the knowledge gained from experimental studies. The main contents of this work are summarized in figure 7.1.

Research in the field of L-PBF stents is still very nascent, and there are currently no comparable studies in the field of numerical analysis of L-PBF stents. The method presented here for numerical analysis of L-PBF is very computationally intensive and is based on several assumptions that merit further discussion. This concerns not only the actual stent modeling, but also the determination and modeling of the material behavior of the L-PBF stents, the investigated stent design, the L-PBF process itself, as well as the post-processing of the stents. To establish L-PBF as an alternative approach for stent manufacturing, the fatigue strength of L-PBF stents as well as their biocompatibility and interaction with the surrounding tissues have to be analyzed. Thus, following the comprehensive discussion of the content of this doctoral thesis, these additional aspects will be addressed to provide motivation for future research.

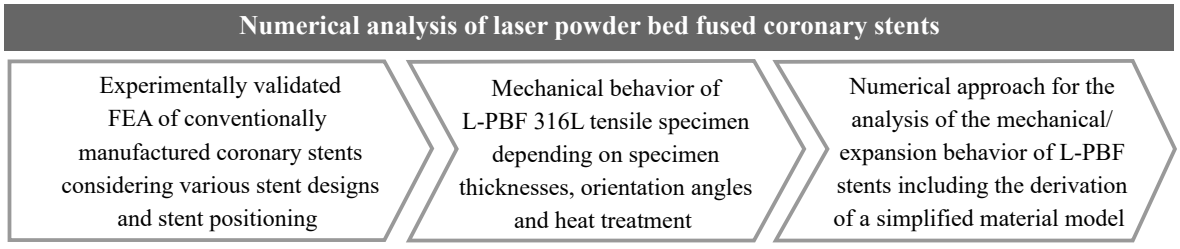

Figure 7.1: Main contents for the development of a method for numerical analysis of L-PBF stents within this doctoral thesis.

7.1 L-PBF process and post-processing for coronary stents

The L-PBF process fundamentally affects the morphology and mechanical properties of the L-PBF stents and thus the determines the requirements of the numerical stent model. Therefore, due to the pronounced process-related irregularities the stent models had to be reconstructed from CT data, rather than simply using the intended stent CAD model. In this work, a commercial industrial L-PBF machine including a fixed set of process parameters was used to generate the L-PBF stents. Since the laser spot had a comparable diameter to that of the intended stent struts (D_{laser} =100 - 150 μm, D_{strut} =100 μm), the L-PBF stents were affected by distinct process-related geometric irregularities, mainly related to sphere-pile like defects of the melt pools. Currently, there are only a few studies on L-PBF stents in the literature, that were mainly conducted by two research groups [26, 27, 31, 32]. To generate the L-PBF stents, these studies also used commercial industrial L-PBF machine with comparable laser spot size and powder particle sizes as in the present work (table 7.1). Based on the findings of this work and the available experimental L-PBF stents studies in the literature [26, 31, 32], it can thus be concluded that coronary L-PBF stents can in principle be manufactured with industrial L-PBF machines. However, due to the limited accuracy of these L-PBF machines, the resulting L-PBF stents will be affected by significant process-related irregularities which affect both the morphology of the stents and their mechanical behavior. Due to high surface roughness and process-related defects, such as pores or notches, these irregularities not only negatively affect the structural integrity and thus the strength and damage behavior of the stents during expansion, but may also reduce fatigue strength, compromise corrosion resistance, or injure the surrounding tissue during/after stent implantation.

Table 7.1: Comparison of the L-PBF process parameter used for manufacturing L-PBF coronary stents and L-PBF process parameters of μ-L-PBF.

L-PBF stent study	L-PBF machine	Laser diameter, μm	Material	Powder sizes, μm	Layer thickness, μm
present study	SLM 250	100 - 150	316L	10 - 45	30
Finazzi [31]	Renishaw AM250	75	CoCr	20 - 53	30
Hufenbach [32]	SLM 250	100 - 150	FeMnCS	10 - 45	30
μ-L-PBF [137]		$\leq$ 20 - 55		$\leq$ 10	$\leq$ 1 - 50

Improvement opportunities for L-PBF stents by optimized L-PBF process parameters

To establish L-PBF as a reliable alternative to conventional stent manufacturing, the process-related irregularities must be minimized to improve the structural integrity of L-PBF stents. Thus, it is necessary to optimize the L-PBF process specifically for filigree structures/coronary stents. This includes the optimization of process parameters, but also the use/development of specific μ-L-PBF machines. The focus of this work was not on the development of the L-PBF process or the optimization of the applied process parameters. Nevertheless, a brief overview of the process

parameters of L-PBF that are crucial for the quality of the filigree L-PBF structures is given below to illustrate the potential for improvement of L-PBF stents. This overview is based on the review article by Nagarajan et al. [137], which is referred to for further description.

L-PBF process parameters which affect the later quality of the L-PBF part can generally be divided into three categories: i) powder-related, ii) laser-related and iii) powder bed-related process parameters. Powder-related process parameters are mainly invariant during the manufacturing process and include e.g., the chemical composition, particle size/form, particle size distribution, surface morphology, internal porosity, flowability and apparent density of the powder. Powder bed-related process parameter include, for example, the separation strategy, the powder bed density, the building chamber atmosphere and the layer thickness, the latter being a decisive factor for the quality of the (filigree) L-PBF part. Laser-related process parameter include the laser system parameters, e.g., laser type, laser power and spot size, as well as scanning parameter (e.g., scanning speed, scanning strategy and hatch spacing). Of all these factors, it has been found that the laser-material interaction and thus the melt pool behavior are mainly influenced by the layer thickness, the particle size, and the laser parameters. When producing filigree structures consisting of only one or a few melt pools across the cross section, these parameters must be precisely adjusted to achieve the desired geometric and mechanical properties of the L-PBF part. [137]

In the following, distinct factors that are essential for improving the quality of filigree L-PBF structures/stents are discussed in more detail. Among other, Demir et al. [26] found that the scanning strategy, laser peak power and pulse duration have a strong impact on geometric fidelity and surface roughness of L-PBF CoCr stents. Thus, increased laser peak power and pulse duration were found to enlarge the strut diameter and to decrease surface roughness. In addition to laser parameters such as scan speed, laser power and scanning strategy, which are also relevant for the quality of macro-L-PBF parts, a small laser spot diameter (i.e. $D_{laser} \leq 20$ - 55 μm), a small powder particle size (i.e. $D_{powder} \leq 10$ μm) and an associated low layer thickness ($t_{layer} \leq 1$ - 50 μm) are decisive factors for a fine resolution and high quality of filigree L-PBF structures [137]. A fine powder particle size combined with a low layer thickness is thus associated with reduced surface roughness and increased density due to complete melting of the powder, as well as a reduction in the staircase effect [71, 153]. Combined, with an accurate positioning of the laser spot with respect to the previous layer, this might compensate the observed strut waviness and the sphere/plate-pile effect. However, one must emphasize that finer powder is also associated with an increased risk of powder contamination [154]. Additionally, the use of finer powder increases the undercooling rate during L-PBF, which on the one hand increases solidification and thus leads to a finer microstructure, but at the same time may also favor metastable phases and higher residual stresses [154]. For a comprehensive review of the influence of the powder, it is referred to Ref. [154].

Finally, one must note that in addition to the L-PBF process parameters described above, quality of the L-PBF is also dependent on their distinct topology (viz., feature size, shape). Due to the layered structure and the staircase effect, process-related irregularities occur more frequently in inclined structures (staircase effect) and at the nodes of the L-PBF lattice structures (material accumulation). To counteract these effects, a critical strut inclination must be defined for the respective L-PBF process and individual geometric part parameters, such as the position of nodes, should be specified as a function of the layer thickness [27, 31]. Moreover, geometric features, such as strut thickness and inclination, have a significant influence on the local thermal history and thus also on the microstructure, mechanical properties, and the occurrence of geometric irregularities of the L-PBF part [71]. Thus, in summary, there are various parameters effecting the quality of L-PBF parts including e.g., process parameter, raw material powder, shape of the intended part. The definition of universal process parameters for filigree L-PBF parts is therefore hardly possible. Research in the field of μ-L-PBF is still very limited, with hardly any extensive parametric analyses regarding the mechanical properties or microstructure of filigree L-PBF parts [137]. However, such studies are essential to improve the quality of filigree L-PBF structures/stents and therefore represent an attractive research area.

Improvement opportunities for L-PBF stents by optimization of post-processing steps
Besides the optimization of the L-PBF process, the surface quality, and mechanical properties of the L-PBF stents can further be modified/improved by adequate post-processing. According to the current state of the art, L-PBF parts built on common industrial L-PBF machines and μ-L-PBF machines exhibit a surface roughness of $R_a > 10$ μm and $R_a > 1$ μm, respectively [137]. However, for biomedical applications, surface roughness of $R_a < 0.5$ μm is required [31]. Therefore, adequate surface treatment is essential to smooth the surface without damaging the filigree structure or significantly affecting the topology of the structure.

Potential surface finishing techniques for filigree L-PBF parts include computer numerically controlled (CNC) machining, chemical etching/electrochemical polishing, laser polishing, abrasive blasting, and abrasive flow machining [137]. The effectiveness and applicability of any surface treatment method depends on a variety of factors, including initial surface roughness, part size, geometry, minimum feature size and desired surface roughness [137]. For a detailed review on the various finishing techniques, it is referred to Ref. [137]. Surface treatment of L-PBF stents is challenging due to their complex geometry (e.g., filigree struts, high aspect ratios, oblique and curved struts) and the need for surface treatment on both the inner and outer strut surfaces. In this work but also in previous studies in the literature [31], electropolishing was used for the surface treatment of L-PBF stents/lattice structures. Finazzi et al. [31] thus reduced the average surface roughness of L-PBF CoCr stents from $R_a = 8.4$ μm to $R_a = 2.2$ μm. Pyka et al. [155] even achieved surface roughness of $R_a \approx 0.5$ μm by electropolishing L-PBF Ti-6Al-4V lattice structures. However, due to the erosive nature of electropolishing and the locally increased

material removal that occurs depending on the part geometry and the local orientation of the electric field lines, there is a risk of reducing the geometric accuracy of the L-PBF structures (e.g. reduction of the strut cross section) [31, 137]. The increased material removal should therefore already be considered within the stent design development so that the desired strut thicknesses are still available after surface treatment. Abrasive blasting is another promising surface finishing method for L-PBF stents. This surface treatment method is very simple and flexible, with surface roughness of $R_a < 1$ μm achievable [156]. However, the main disadvantage of this method is the lack of repeatability [137]. Moreover, in case of L-PBF 316L stents, additional electropolishing would be mandatory to passivate the stents and thus to ensure their biocompatibiliy [64, 138].

Thus, in summary, the further development and optimization of μ-L-PBF machines and their process parameters, as well as the improvement of surface finishing techniques, could reduce the currently observed process-related geometric irregularities of L-PBF stents. Improvement in these fields is crucial for the establishment of L-PBF as a reliable manufacturing method for coronary stents. Such improvements could minimize process-related geometric irregularities, allowing L-PBF stent morphologies to closely approximate the intended CAD model. Consequently, it would even be conceivable that numerical L-PBF stent models could be generated based on their CAD models. At the current state of the art, however, consideration of process-related irregularities within the stent models is essential for reliable numerical analyses. Given the high potential for improvement and development of L-PBF stents, the numerical analyses performed in this work should be considered as an extreme or worst-case scenario. However, the principle numerical methodology presented in this work is also applicable to the further optimized L-PBF stents. Any improvement in the field of L-PBF stents and thus a reduction of irregularities would even reduce the complexity of the stent model and thus increase the computational efficiency.

7.2 L-PBF stent model

In this work, L-PBF process-related geometric irregularities were found to distinctly affect both the stent morphology and their macroscopic mechanical behavior. Thus, significant deviations between the morphology and macroscopic behavior of the intended stent CAD model and the actual L-PBF stents were observed. For numerical analysis of L-PBF stents, the consideration of geometric irregularities within the stent model was therefore found to be essential to achieve reliable predictions about the structure-property relationship. In this work, the stent models were reconstructed from CT scans of actual L-PBF stents, allowing both surface irregularities and larger subsurface defects, such as pores, to be explicitly depicted. However, this approach requires the stents to be built via L-PBF and scanned via high-resolution μ-CT prior to numerical stent modeling. Although numerical simulation can then be used to identify critical areas within

the stent, the general benefits of numerical simulation, such as reducing the number of stent prototypes to be built or increasing the efficiency of design development through virtual stent analysis, can only be exploited to a limited extent due to the dependence of the numerical models on the actual L-PBF stent geometry.

To improve the efficiency of numerical L-PBF stent analysis, further approaches considering process-related irregularities in the FE stent model should be considered in subsequent studies. The geometric irregularities observed in this work mainly involved strut waviness, local strut thickness variations, and global increased strut diameter. For L-PBF lattice structures, some approaches to consider geometric irregularities within CAD and FE models of L-PBF lattice structures have already been established and are likely to be transferable to L-PBF stents. On overview of some established approaches is provided in table 7.2.

Table 7.2: Approaches for considering process-related geometric imperfections within FE models of L-PBF struts/lattice structures.

Schematic illustration	Description	Studies using this approach
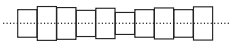	Single struts are composed of beam elements with various diameter along the strut.	[34, 36]
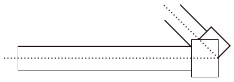	Single struts are composed of beam elements with an homogeneous diameter. At the junction points the diameter of a single beam element is increased to account for material accumulation at the node.	[152, 157]
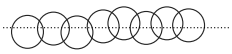	Single struts are composed of intersecting spheres with varying diameter and offset from the strut centerline.	[25, 158]
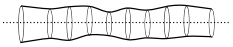	Single struts are obtained using the loft technique on a series of statistically representative elliptical cross sections.	[159]

Using these approaches for considering process-related geometric imperfections, numerically efficient analyses of L-PBF stents could be performed, which are no longer based on a direct reconstruction of an actual L-PBF stent. Thus, new stent designs could be tested or numerically optimized before the actual fabrication of L-PBF stents. These simplified L-PBF stent models could also be used for more comprehensive parametric studies to determine thresholds for critical geometric irregularities, e.g., with respect to strut waviness, or local diameter variations. However, the accuracy and limitations of these approaches for numerical analysis of L-PBF stents need to be fully investigated first, as these approaches are currently only used for L-PBF lattice structures, which have a much higher structural density.

7.3 Material model for L-PBF 316L stents

Determining and modeling the material behavior of L-PBF stents is challenging in many respects. The mechanical properties of L-PBF 316L tensile specimens have been found to be dependent on both specimen thickness and orientation angle. Therefore, to accurately determine the mechanical properties of individual stent struts, it would be necessary to analyze miniaturized tensile specimens with comparable dimensions, orientations angles as well as comparable thermal histories to those of the individual stent struts. Tensile tests on individual L-PBF strands have been performed in some pioneer studies in literature, e.g. in Refs. [119, 120, 147, 149]. However, in this context inaccuracies arise with respect to the determination of the strut cross section, the influence of irregularities, but also in the actual test methodology (specimen clamping, strain measurement). In this work, the material behavior of the L-PBF 316L stents was therefore inversely determined using experimental data and FEAs of L-PBF stent compression. This methodology has been used previously in studies of L-PBF lattice structures [147, 157]. Thus, it was possible for the first time to model the macroscopic mechanical behavior of L-PBF 316L stents both in the as-built condition and after heat treatment. Nevertheless, the method for determining the mechanical behavior of L-PBF 316L as well as the subsequent derivation of the material model is based on some assumptions and simplifications that merit further discussion.

Limitation and potential extension of the L-PBF 316L stent material model

In this work, the mechanical behavior of L-PBF 316L stents was described using a von Mises plasticity model with isotropic strain hardening. In the following, a critical analysis of the choice of an isotropic yield criterion as well as of the chosen hardening law is presented. By determining the material behavior based on the macroscopic response of the stents, the material behavior is assumed to be isotropic, thus neglecting the anisotropy inherent for L-PBF materials. During uniaxial stent compression, deformation occurs almost exclusively at the inclined struts in a bending-dominated manner. Thus, the mechanical properties determined in this work are likely to be primarily representative of the bending of struts with an orientation angle of $\Theta = 45°$. In a study by Shen et al. [119], it was found that single L-PBF 316L strands with diameters of $D = 200\ \mu$m and specimen orientation angles of $\Theta = 0°$, 15°, 30°, and 45° exhibit approximately isotropic tensile properties in contrast to L-PBF 316L bulk material. Thus, the approximation of the L-PBF 316L stent material as isotropic may be justified. However, the findings of Shen et al. [119] are results from a single study and, to the author's knowledge, no further studies are known to investigate the direction-dependent mechanical properties of filigree L-PBF structures. Therefore, further investigations are necessary to statistically substantiate or refute the findings of Shen et al. [119]. Thereupon, if necessary, the von Mises yield criterion used in this work might be replaced, for example, by the Hill yield criterion to account for anisotropic plastic deformation. Moreover, in this work, the isotropic hardening behavior was approximated by the Hollomon's

power law. However, other empirical equations exist for the mathematical description of the hardening behavior, such as the hardening law according to Ludwik [51], Voce [53, 54] or Swift [52] (chapter 2.1.4). Depending on the hardening law, however, different uniform strains and thus a different hardening behaviors are usually obtained for the same experimental data set [160]. Therefore, it is necessary to further investigate the influence of hardening laws on the prediction accuracy of the mechanical behavior of filigree L-PBF 316L structures.

The inverse determination of the mechanical behavior of L-PBF 316L stents based on compression tests also merits further discussion. Chen et al. [80] observed a tension-compression asymmetry in the mechanical behavior of as-built L-PBF 316L tensile specimens with a quadratic cross section of A = 1.4 x 1.4 mm^2 and a gauge length of l = 6.5 mm. During stent compression, some regions of the stent struts are loaded in tension and others in compression. Thus, due to potential homogenization effects, the tension-compression asymmetry might only have a negligible influence on the macroscopic behavior of L-PBF stents. One has further to note, that Chen et al. [80] found that the tension-compression asymmetry of as-built L-PBF 316L was no longer evident after heat treatment. Due to the low ductility and high inhomogeneity of the microstructure of as-built 316L, heat treatment of the L-PBF stents is most likely mandatory, making the influence of the tension-compression asymmetry of as-built L-PBF 316L negligible for the later stent application.

Crystal plasticity and multi-scale approaches for the analysis of the impact of microstructure on the mechanical behavior of L-PBF stents

In general, macroscopic mechanical behavior of stents is mainly determined by their geometry (viz., the shape of the stent unit cell and the strut cross section) rather than by local variations in microstructure. Thus, in this work, the inverse determination of L-PBF 316L stent material behavior as well as its description by a continuum mechanics/macroscale model of plasticity has been found to be suitable for the analysis of macroscopic behavior of L-PBF stents (e.g., stent compression, expansion). However, due to the high material inhomogeneity of L-PBF 316L stent material (e.g., grains, pores, melt pool boundaries), the reliability of such a macroscale plasticity model for predicting local stress states, damage, or fatigue of L-PBF stents has to be critically questioned. Thus, for such analysis multi-scale approaches for describing the mechanical behavior of L-PBF 316L should be considered. Therefore, potential research opportunities in multi-scale evaluations and CP modeling of L-PBF 316L stents are addressed below.

Based on CP models, the influence of microstructure on the continuum behavior of L-PBF 316L stents, e.g., in terms of inhomogeneous deformation, the influence of pores, or the interaction of individual grains with different orientation, could be evaluated in more detail. A possible starting point for such numerical analyses is the work of Zhao et al. [161]. In a high-fidelity

framework, they integrated grain boundary strengthening and free-surface softening into a CP-FEM framework for the evaluation of open-cell aluminum foams. By applying this framework to L-PBF 316L stents, the Hall-Petch effect (i.e., intrinsic size effect) as well as the unconstrained movement of dislocations across the free surfaces (i.e., surface constraint size effect) of the stent struts could be considered. Thus, the exact cause and influencing factors of the size effect could be investigated in more detail instead of considering the size effect only by a correction factor as in the present doctoral thesis. The approach of Zhao et al. [161] is further capable of analyzing the influence of oxide layers and thus the constraint of dislocations at the previously free strut surfaces on the yield strength of open-cell aluminum foams. With respect to L-PBF 316L stents, this numerical approach is particularly interesting to assess the influence of the passive layer formed on the surface of the stent during electropolishing. In addition, CP-FEM can also be used to perform further parametric studies and to optimize the microstructure according to the requirements of the loading conditions inherent to the stent application. Among other things, a variety of synthetic microstructures with, for example, variations in grain size, shape and orientation as well as variations in the loads (tension, compression, bending) could be carried out and then, based on the knowledge gained, the L-PBF process and post-treatment could be explicitly adapted to the microstructural requirements of L-PBF 316L.

Sweeney et al. [162] further showed that conventional continuum mechanical fatigue life prediction methods are not suitable for predicting cyclic deformation of conventionally manufactured 316L stents. This was attributed to material inhomogeneities and the small number of grains across the strut thickness and the resulting localized/grained plastic deformation. Conventionally manufactured 316L is characterized by austenitic grains with equiaxed grain shape and heterogeneous grain orientation, while L-PBF 316L has elongated grains with a preferred crystal orientation. Due to the increased process-related material inhomogeneity of L-PBF 316L stents, alternatives to a mere continuum mechanical fatigue assessment of L-PBF 316L stents need to be considered in future work. One possible approach is the methodology proposed by Sweeney et al. [162]. Their method involved a multi-scale approach consisting of i) a macroscopic continuum mechanical stent-artery model to determine the fatigue boundary conditions of the stent submodel, ii) a local micromechanical stent submodel consisting of a unit cell with explicit modeling of the inhomogeneous microstructure, and iii) a combined kinematic-isotropic strain hardening-CP material model.

In summary, this work has provided a method for the determination and modeling of the macroscopic material behavior of L-PBF 316L stents and thus allowed for the numerical analysis of the macroscopic response of L-PBF stents under deformation for the first time. However, mere continuum mechanics/macroscale models of plasticity might not be sufficient for more depth analysis such as analysis of the distinct influence of microstructure on the macroscopic stent response, the analysis of local stress states or the damage and fatigue behavior of the L-PBF 316L

stents. For such comprehensive analysis, the approach presented in this doctoral thesis should be extended to consider multiscale modeling approaches or CP models to better account for the material inhomogeneity inherent for L-PBF 316L materials.

7.4 Investigated L-PBF stent design

Another critical aspect of this work is the investigated L-PBF stent design. One must note that in coronary stents, the full range of design freedoms of macroscopic L-PBF parts cannot be applied for filigree L-PBF parts due to the missing ability to use support structures. Thus, further specific design rules must be considered for L-PBF stents that are summarized in Ref. [27]. These design rules enable the creation of stent designs that can be manufactured without support structures. Thus, among other things, restrictions arise around strut inclination angle ($\alpha < 45°$), strut overhang regions ($l < 1.0$ mm) and strut spacing ($d > 0.3$ mm) [27]. Furthermore, these design guidelines further recommended to define the position of the vertices of the stent geometry depending on the layer thickness to reduce the staircase effect [27].

The stent design studied in this work was initially designed to be generated without support structures via L-PBF. In this work, the focus was not on the development of the stent design. Rather, it was adopted from previous internal experimental feasibility studies. However, for the sake of completeness, the development process of this stent design will be briefly addressed. The original stent design also composed a regular fish bone pattern, but with six unit cells in the circumferential direction. Since this design had a very high radial stiffness and was therefore not expandable via balloon catheter, the number of unit cells in the circumferential direction was successively reduced. Finally, with only two unit cells in the circumferential direction, a radial stiffness comparable to conventionally manufactured stents could be achieved. Since no further optimization of this design was performed, this stent design should rather be considered as a first demonstrator for initial feasibility study. Besides the actual manufacturability, coronary stents must further fulfill additional requirement. These concern the stent high flexibility and thus curve mobility, low recoil, low foreshortening, and sufficient area coverage. Considering these requirements, the investigated L-PBF stent design in this work has some limitations, which are briefly discussed below.

Following, stent expansion the cross section of the investigated L-PBF reached a rather angular shape (figure 6.18) as it is composed of only two unit cells across the circumferential direction. Therefore, the blood vessel would be unevenly dilated during the actual stent application, which could lead to high local arterial tension and disruption of natural hemodynamics, which in turn could promote restenosis. The investigated L-PBF further provide a low area coverage, i.e., the ratio between the outer stent area and the equivalent cylindrical sheath area enclosed by the

stent. With a stent surface area of A_{stent} = 12.5 mm^2 and an equivalent enclosed cylindrical area $A_{eq.zyl}$[1] = 319.3 mm^2, the investigated stent has an area coverage of 7.8%. In contrast, conventional stent designs have an area coverage of about 12 - 15 % [163]. Thus, the investigated L-PBF might not adequately support the blood vessel which in return might cause tissue to prolapse through the free areas within the stent unit cells. Due to the closed cell design, i.e., the lack of flexible connectors, the flexibility of the investigated L-PBF is a further critical concern.

In summary, the L-PBF stent design investigated in this work should only be considered as a first demonstrator and further studies regarding the improvement and optimization of the proposed stent design or the development of further L-PBF designs are mandatory. In addition, there is a possibility that improvements in the μ-L-PBF process will allow for even finer structures and thus support structures, which could further expand the design freedom of L-PBF stents.

7.5 Further critical considerations for the establishment of L-PBF 316L stents

To establish L-PBF for a reliable alternative to conventional stent manufacturing, the fatigue behavior of the L-PBF stents, their biocompatibility as well as their interaction with the vessel wall must be evaluated.

Challenges regarding the fatigue behavior of L-PBF 316L stents

According to DIN EN ISO 25539 [140], coronary stents must have an intended service life of at least 10 years, which corresponds to a pulsating load of at least 380 million heart cycles. Like conventionally processed metals, fatigue of L-PBF parts was found to be significantly affected by impurities, residual stresses, surface finish, and grain/phase structure [164–166]. Inherent to L-PBF is the dependency of the microstructure and emerging defects on the applied L-PBF process parameters and the geometry of the part to be built. These, in turn, affect the mechanical properties of L-PBF structures and especially the high cycle fatigue properties. In a literature review, Li et al. [165] found a significant variance of the S-N curve depending on the process parameters, heat and surface treatment. Furthermore, L-PBF parts in the as-built condition are associated with lower fatigue performance, which is attributed to increased surface crack initiation due to high surface roughness and local defects/notches [167]. After surface treatment, fatigue is mainly associated with internal defects (pores, lack of fusion defects) [165, 168]. Yadollahi et al. [166] found that near-surface are particularly critical for fatigue. Moreover, identified the spacing between defects as very critical. This distance determines a potential coalescence of cracks originating from the respective defects, which in turn leads to an abrupt

[1] $A_{eq.zyl} = 2 \cdot D_{o,stent}/2 \cdot \pi \cdot l_{stent}$ =2 · 3.0/2 mm·π· 16.94 mm = 159.65 mm^2

reduction of the remaining strength of the L-PBF part. Furthermore, they found a dependence of the fatigue properties on the specimen orientation, which is mainly attributed to the orientation of the layers and thus potential layer defects to the loading direction. In summary, the fatigue properties of L-PBF parts depend on a variety of parameters and is part of ongoing research in literature.

For L-PBF stents, the observed high surface roughness, different strut inclination angles, as well as porosity should be considered as particularly critical with respect to their fatigue behavior. One should note that due to the small structure size, almost all pores within the stent struts should be considered as near-surface pores and thus as particularly critical. Due to the small number of grains across the cross section, it is also important to investigate the influence of microstructure, such as grain boundaries, on the fatigue properties of the L-PBF stents. Therefore, after improving the L-PBF process parameters and stent design, it is imperative to investigate the fatigue properties of L-PBF stents.

Challenges regarding the biocompatibility of L-PBF 316L stents

Recent studies indicated that L-PBF 316L exhibits even higher corrosion resistance and better biocompatibility than conventionally manufactured 316L [40, 169–172]. Kong et al. [169] further indicated that the corrosion resistance and biocompatibility on the L-PBF 316L is dependent on the applied L-PBF process parameters. Thus, for L-PBF 316L fabricated with a laser power of P = 195/220 W, increased passive film growth, lower corrosion rate, and higher biocompatibility than quenched 316L were observed, while for L-PBF 316L fabricated with a laser power of P = 120 W, a reduced corrosion resistance and even a toxic effect on cells were observed. However, a follow-up study by Kong et al. [40] found inferior corrosion properties for L-PBF 316L produced with a laser power of P = 220 W compared to wrought 316L, thus contradicting directly their first study [169]. They attributed the later observed inferior corrosion properties to an unfavorably distribution of process-related defects, e.g., melt pool boundaries, non-equilibrium phases and pores. One should note that the exact influence of porosity on the corrosion resistance of L-PBF materials has not yet been clarified in the literature [40, 171, 172]. In summary, the corrosion resistance and biocompatibility of L-PBF 316L depends on L-PBF process parameters and process-related defects. Due to the high surface-to-volume ratio of L-PBF stents, additional effects are to be expected which might cause deviation the impacting the corrosion behavior and biocompatibility of L-PBF bulk and stent material. Therefore, further studies are needed to investigate the corrosion behavior and biocompatibility of L-PBF stents.

Challenges regarding L-PBF 316L stent-artery interaction

Finally, the influence of L-PBF process-related irregularities on stent-artery interaction needs to be investigated in more detail. During/after stent implantation, these could cause damage

to the arterial wall and thus promote ISR. Therefore, the extent of arterial stress caused by the irregularities needs to be determined. Subsequently, the positive effects of a patient-specific stent design must be weighed against the potential negative effects of geometric irregularities, and further necessary modifications of the L-PBF stent design or its manufacturing process must be identified.

8 Conclusion and Outlook

This doctoral thesis was concerned with the development of a numerical method for the analysis of L-PBF 316L stents, considering the influence of process-related irregularities and post-treatment steps. The individual work packages included i) the development and validation of a FEA of crimping and expansion of a conventionally manufactured 316L stent, ii) the experimental determination of the influence of specimen thickness, specimen orientation angle and homogenization heat treatment on the mechanical behavior of L-PBF 316L flat tensile specimens, and iii) the consolidation of the findings from the stent FEAs and experimental investigations to develop a methodology to determine the mechanical properties of L-PBF 316L stents and their subsequent numerical analysis, considering both process-related irregularities and different post-processing conditions.

The developed numerical models for the analysis of conventional stents included an extension of the existing approaches by a detailed modeling of the balloon folding, as well as a comparison of the balloon-stent expansion approach with a displacement-controlled expansion approach. While numerical approaches for stent expansion analysis are well established in the literature, this work is the first comprehensive validation of these numerical approaches considering different stent designs and stent positions on the balloon catheter. It was found that the simplified displacement-controlled expansion approach can reliably predict the final expanded stent shape as well as the occurring stress states. However, it was found that transient stent expansion can only be predicted using the balloon stent expansion approach, which is more computationally intensive and involves explicit modeling of a folded balloon catheter and its pressurization. Extensive validation of the numerical models suggests that the methods for numerical analysis of stents presented in this work is applicable to a wide variety of stent designs and thus also to novel L-PBF stent designs.

This work further provided the first comprehensive investigation of the influence of specimen thickness, specimen orientation angle and homogenization heat treatment, on the mechanical behavior of L-PBF 316L tensile specimens. It was found that the specimen strength increased with increasing specimen thickness up to a specimen thickness of 1.5 mm and then reached an approximately constant strength value regardless of the specimen thickness. Anisotropic mechanical behavior typical of L-PBF metals was also observed in this work. An emerging finding

was that the extent of anisotropic mechanical properties is dependent on specimen thickness and increases with decreasing specimen thickness. It was found that homogenization heat treatment homogenizes the microstructure and reduces the yield strength, while the mechanical properties remain dependent on specimen thickness and orientation angles. These results indicate that a meaningful comparison of the mechanical properties of various L-PBF specimens is reliable only if specimen thicknesses, orientation angles and post-processing conditions are similar. For the determination of the mechanical properties of L-PBF 316L stents, these requirements represent a major challenge, e.g. due to the filigree test specimen geometries required and the associated difficulties in specimen preparation and testing, which are highly susceptible to error.

To overcome these challenges, an approach for the inverse determination of mechanical properties of L-PBF 316L based on experimental data and FEAs of L-PBF stent compression was presented in this doctoral thesis. Since this approach is based on reconstruction of actual L-PBF stents, as well as their experimental and numerical analysis, it is very resource expensive. Nevertheless, this effort is justified as it not only determined the mechanical behavior of L-PBF 316L stents but also enabled the first numerical analysis of L-PBF stents. In this context, the limitations of this approach, especially with respect to material modeling, are briefly reviewed. It assumes the mechanical behavior of L-PBF 316L being isotropic and does not explicitly consider inherent characteristics of L-PBF materials, such as the distinct influence of the microstructure and the associated anisotropy or the size effect. For more comprehensive analyses of the mechanical behavior of L-PBF 316L, both multiscale and CP material models should be considered. This is expected to reveal the exact causes of the size effect observed in this work and serves as a first step towards future investigation of the damage and fatigue behavior of L-PBF 316L.

The determination of the mechanical properties of the stents was followed by the numerical analysis of the L-PBF 316L stents, focusing on the analysis of the influence of the process-related geometric irregularities and the post-processing steps on the mechanical behavior of the stents. Morphological analysis of the L-PBF 316L stent models revealed significant deviations between the actual L-PBF stents and the intended stent (CAD model). These were mainly characterized by high surface roughness, strut waviness, increased and inhomogeneous strut diameters, local notches, and internal defects. FEA of L-PBF stent expansion analysis showed that L-PBF stents can achieve expansion behavior comparable to conventionally manufactured stents only after surface treatment and heat treatment. This is attributed to a reduction in the strut cross section and thus a reduction in the moment of inertia of the stent struts after surface treatment and to the reduction in yield strength and increase in ductility of the L-PBF 316 stent material after homogenization heat treatment. However, in areas with highly pronounced geometric irregularities, local critical stress/strain are also observed in the surface-treated L-PBF stent, which means that the structural integrity of the L-PBF 316L stents studied here cannot be guaranteed at present.

To establish L-PBF as a reliable alternative to conventional stent production, process-related geometric and metallurgical irregularities must be minimized. This can be achieved by optimizing the L-PBF process itself, but also by improving the post-treatment steps, e.g. heat and surface treatment, and by optimizing the stent design. Numerical models may be efficiently used for stent development. Instead of reconstruction from real L-PBF stents, alternative methods, e.g., generation of synthetic structures based on statistical data, should be investigated to account for process-related geometric irregularities within the stent models. This is expected to improve the efficiency of numerical L-PBF stent models and subsequently promote the development/optimization of L-PBF stent designs. Besides the improvement possibilities of L-PBF stents, further research is needed to analyze the fatigue and fracture behavior, biocompatibility, and interaction of the L-PBF stent with the blood vessel.

The development of L-PBF stents is a very complex interdisciplinary task involving manufacturing technology, material science, design development and numerical simulation. To establish L-PBF as a reliable alternative to conventional stent fabrication, continued research in this area is essential. The method to determine the mechanical properties of L-PBF stents and their numerical analysis contained in this doctoral thesis is expected to serve as a sound basis for future development of L-PBF 316L stents.

Bibliography

[1] Statistisches Bundesamt. Verteilung der häufigsten Todesursachen in Deutschland im Jahr 2018; 2020. Available from: https://de.statista.com/statistik/daten/studie/215791/umfrage/todesfaelle-in-deutschland-nach-todesursachen-und-geschlecht/.

[2] Van Buuren F. Bericht über die Leistungszahlen der Herzkatheterlabore in der Bundesrepublik Deutschland. Eine Datenerhebung mit Unterstützung der Kommission für Klinische Kardiologie und der Arbeitsgruppen Interventionelle Kardiologie und Angiologie der Deutschen Gesel. Kardiologe. 2010;4(6):502–508.

[3] Kim MS, Dean LS. In-Stent Restenosis. Cardiovascular Therapeutics. 2011;29(3):190–198.

[4] Geith MA, Nothdurfter L, Heiml M, Agrafiotis E, Gruber M, Sommer G, et al. Quantifying stent-induced damage in coronary arteries by investigating mechanical and structural alterations. Acta Biomaterialia. 2020 oct;116(xxxx):285–301.

[5] Stone PH, Coskun AU, Kinlay S, Clark ME, Sonka M, Wahle A, et al. Effect of endothelial shear stress on the progression of coronary artery disease, vascular remodeling, and in-stent restenosis in humans: In vivo 6-month follow-up study. Circulation. 2003;108(4):438–444.

[6] Timmins LH, Meyer CA, Moreno MR, Moore JE. Mechanical modeling of stents deployed in tapered arteries. Annals of Biomedical Engineering. 2008;36(12):2042–2050.

[7] Gyöngyösi M, Yang P, Khorsand A, Glogar D, Gyo M, Gyöngyösi M, et al. Longitudinal straightening effect of stents is an additional predictor for major adverse cardiac events. Journal of the American College of Cardiology. 2000;35(6):1580–1589.

[8] Chen HY, Hermiller J, Sinha AK, Sturek M, Zhu L, Kassab GS. Effects of stent sizing on endothelial and vessel wall stress: potential mechanisms for in-stent restenosis. Journal of Applied Physiology. 2009;106(5):1686–1691.

[9] Morlacchi S, Colleoni SG, Cárdenes R, Chiastra C, Diez JL, Larrabide I, et al. Patient-specific simulations of stenting procedures in coronary bifurcations: Two clinical cases. Medical Engineering and Physics. 2013;35(9):1272–1281.

[10] Wiesent L, Schultheiß U, Schmid C, Schratzenstaller T, Nonn A. Experimentally validated simulation of coronary stents considering different dogboning ratios and asymmetric stent positioning. PLoS ONE. 2019;14(10):1–25.

[11] Hoffmann R, Mintz GS. Coronary in-stent restenosis - Predictors, treatment and prevention. European Heart Journal. 2000;21(21):1739–1749.

[12] Timmins LH, Miller MW, Clubb FJ, Moore JE. Increased artery wall stress post-stenting leads to greater intimal thickening. Laboratory Investigation. 2011;91(6):955–967.

[13] Wu W, Qi M, Liu XP, Yang DZ, Wang WQ. Delivery and release of nitinol stent in carotid artery and their interactions: A finite element analysis. Journal of Biomechanics. 2007;40(13):3034–3040.

[14] Djukic T, Saveljic I, Pelosi G, Parodi O, Filipovic N. Numerical simulation of stent deployment within patient-specific artery and its validation against clinical data. Computer Methods and Programs in Biomedicine. 2019;175:121–127.

[15] Lemos PA, Serruys PW, van Domburg RT, Saia F, Arampatzis CA, Hoye A, et al. Unrestricted Utilization of Sirolimus-Eluting Stents Compared With Conventional Bare Stent Implantation in the "Real World". Circulation. 2004 jan;109(2):190–195.

[16] Moses JW, Leon MB, Popma JJ, Fitzgerald PJ, Holmes DR, O'Shaughnessy C, et al. Sirolimus-Eluting Stents versus Standard Stents in Patients with Stenosis in a Native Coronary Artery. New England Journal of Medicine. 2003 oct;349(14):1315–1323.

[17] Kaiser C, Galatius S, Erne P, Eberli F, Alber H, Rickli H, et al. Drug-eluting versus bare-metal stents in large coronary arteries. New England Journal of Medicine. 2010;363(24):2310–2319.

[18] Bønaa KH, Mannsverk J, Wiseth R, Aaberge L, Myreng Y, Nygård O, et al. Drug-Eluting or Bare-Metal Stents for Coronary Artery Disease. New England Journal of Medicine. 2016 sep;375(13):1242–1252.

[19] Kaiser C, Brunner-La Rocca HP, Buser PT, Bonetti PO, Osswald S, Linka A, et al. Incremental cost-effectiveness of drug-eluting stents compared with a third-generation bare-metal stent in a real-world setting: randomised Basel Stent Kosten Effektivitäts Trial (BASKET). The Lancet. 2005;366(9489):921–929.

[20] De Beule M, Mortier P, Carlier SG, Verhegghe B, Van Impe R, Verdonck P. Realistic finite element-based stent design: The impact of balloon folding. Journal of Biomechanics. 2008;41(2):383–389.

[21] Lepor NE, Madyoon H, Kereiakes DJ. Effective and efficient strategies for coronary revascularization in the drug-eluting stent era. Reviews in cardiovascular medicine. 2002;3 Suppl 5(SUPPL. 5):S38–50.

[22] Stoeckel D, Bonsignore C, Duda S. A survey of stent designs. Minimally Invasive Therapy and Allied Technologies. 2002;11(4):137–147.

[23] Mani G, Feldman MD, Patel D, Agrawal CM. Coronary stents: A materials perspective. Biomaterials. 2007;28(9):1689–1710.

[24] Kaya AC, Fleck C. Deformation behavior of open-cell stainless steel foams. Materials Science and Engineering: A. 2014 oct;615:447–456.

[25] Ravari KMR, Kadkhodaei M. A Computationally Efficient Modeling Approach for Predicting Mechanical Behavior of Cellular Lattice Structures. Journal of Materials Engineering and Performance. 2015 jan;24(1):245–252.

[26] Demir AG, Previtali B. Additive manufacturing of cardiovascular CoCr stents by selective laser melting. Materials & Design. 2017;119:338–350.

[27] Finazzi V, Demir AG, Biffi CA, Chiastra C, Migliavacca F, Petrini L, et al. Design rules for producing cardiovascular stents by selective laser melting: Geometrical constraints and opportunities. Procedia Structural Integrity. 2019;15:16–23.

[28] Yan C, Hao L, Hussein A, Young P, Raymont D. Advanced lightweight 316L stainless steel cellular lattice structures fabricated via selective laser melting. Materials & Design. 2014 mar;55:533–541.

[29] Mahmoud D, Elbestawi M. Lattice Structures and Functionally Graded Materials Applications in Additive Manufacturing of Orthopedic Implants: A Review. Journal of Manufacturing and Materials Processing. 2017 oct;1(2):13.

[30] Zitelli, Folgarait, Di Schino. Laser Powder Bed Fusion of Stainless Steel Grades: A Review. Metals. 2019 jun;9(7):731.

[31] Finazzi V, Demir AG, Biffi CA, Migliavacca F, Petrini L, Previtali B. Design and functional testing of a novel balloon-expandable cardiovascular stent in CoCr alloy produced by selective laser melting. Journal of Manufacturing Processes. 2020;55(February):161–173.

[32] Hufenbach J, Sander J, Kochta F, Pilz S, Voss A, Kühn U, et al. Effect of Selective Laser Melting on Microstructure, Mechanical, and Corrosion Properties of Biodegradable FeMnCS for Implant Applications. Advanced Engineering Materials. 2020 oct;2000182(10):1–8.

[33] Dong Z, Zhang X, Shi W, Zhou H, Lei H, Liang J. Study of size effect on microstructure and mechanical properties of AlSi10Mg samples made by selective laser melting. Materials. 2018;11(12).

[34] Lei H, Li C, Meng J, Zhou H, Liu Y, Zhang X, et al. Evaluation of compressive properties of SLM-fabricated multi-layer lattice structures by experimental test and μ-CT-based finite element analysis. Materials & Design. 2019 may;169:107685.

[35] Liu L, Kamm P, García-Moreno F, Banhart J, Pasini D. Elastic and failure response of imperfect three-dimensional metallic lattices: the role of geometric defects induced by Selective Laser Melting. Journal of the Mechanics and Physics of Solids. 2017;107:160–184.

[36] Campoli G, Borleffs MSS, Amin Yavari S, Wauthle R, Weinans H, Zadpoor AAA. Mechanical properties of open-cell metallic biomaterials manufactured using additive manufacturing. Materials and Design. 2013 aug;49:957–965.

[37] Gonzalez FJQ, Nuno N. Finite element modeling of manufacturing irregularities of porous materials. Biomaterials and Biomechanics in Bioengineering. 2016 mar;3(1):1–14.

[38] Yadollahi A, Shamsaei N, Thompson SM, Seely DW. Effects of process time interval and heat treatment on the mechanical and microstructural properties of direct laser deposited 316L stainless steel. Materials Science and Engineering A. 2015;644:171–183.

[39] Hengsbach F, Koppa P, Duschik K, Holzweissig MJ, Burns M, Nellesen J, et al. Duplex stainless steel fabricated by selective laser melting - Microstructural and mechanical properties. Materials & Design. 2017 nov;133:136–142.

[40] Kong D, Dong C, Ni X, Zhang L, Yao J, Man C, et al. Mechanical properties and corrosion behavior of selective laser melted 316L stainless steel after different heat treatment processes. Journal of Materials Science and Technology. 2019;35(7):1499–1507.

[41] Bukala J, Kwiatkowski P, Malachowski J. Numerical analysis of crimping and inflation process of balloon-expandable coronary stent using implicit solution. International Journal for Numerical Methods in Biomedical Engineering. 2017;33(12):1–11.

[42] Chiastra C, Wu W, Dickerhoff B, Aleiou A, Dubini G, Otake H, et al. Computational replication of the patient-specific stenting procedure for coronary artery bifurcations: From OCT and CT imaging to structural and hemodynamics analyses. Journal of Biomechanics. 2016;49(11):2102–2111.

[43] Pant S, Limbert G, Curzen NP, Bressloff NW. Multiobjective design optimisation of coronary stents. Biomaterials. 2011;32(31):7755–7773.

[44] Li H, Liu T, Wang M, Zhao D, Qiao A, Wang X, et al. Design optimization of stent and its dilatation balloon using kriging surrogate model. BioMedical Engineering Online. 2017;16(1):1–17.

[45] Parthasarathy J, Starly B, Raman S. A design for the additive manufacture of functionally graded porous structures with tailored mechanical properties for biomedical applications. Journal of Manufacturing Processes. 2011 aug;13(2):160–170.

[46] Rösler J, Harders H, Bäker M. Mechanisches Verhalten der Werkstoffe. Wiesbaden: Springer Fachmedien Wiesbaden; 2019.

[47] Abaqus. ABAQUS Documentation. Daussault Systèmes, Providence, RI, USA. 2020.

[48] Stoughton TB. A non-associated flow rule for sheet metal forming. International Journal of Plasticity. 2002;18(5-6):687–714.

[49] Stoughton TB, Yoon JW. Anisotropic hardening and non-associated flow in proportional loading of sheet metals. International Journal of Plasticity. 2009;25(9):1777–1817. Available from: `http://dx.doi.org/10.1016/j.ijplas.2009.02.003`.

[50] Hollomon JH. Tensile Deformation. Transactions of the Metallurgical Society of AIME. 1945;162:268–290.

[51] Ludwik P. Elemente der Technologischen Mechanik. vol. 53. Berlin, Heidelberg: Springer Berlin Heidelberg; 1909.

[52] Swift HW. Plastic instability under plane stress. Journal of the Mechanics and Physics of Solids. 1952 oct;1(1):1–18.

[53] Voce E. The relationship between stress and strain forhomogeneous deformations. Journal of the Institute of Metals. 1948;74:537–562.

[54] Voce E. A practical strain hardening function. Metallurgia. 1955;51:219–226.

[55] Geers MGD, Brekelmans WAM, Janssen PJM. Size effects in miniaturized polycrystalline FCC samples: Strengthening versus weakening. International Journal of Solids and Structures. 2006;43(24):7304–7321.

[56] Roters F, Eisenlohr P, Hantcherli L, Tjahjanto DD, Bieler TR, Raabe D. Overview of constitutive laws, kinematics, homogenization and multiscale methods in crystal plasticity finite-element modeling: Theory, experiments, applications. Acta Materialia. 2010;58(4):1152–1211.

[57] Sweeney C. Micromechanics of fatigue with application to stents [PhD Thesis]. National University of Ireland; 2014.

[58] Murphy BP, Savage P, McHugh PE, Quinn DF. The Stress–Strain Behavior of Coronary Stent Struts is Size Dependent. Annals of Biomedical Engineering. 2003;31(6):686–691.

[59] Bajaj P, Hariharan A, Kini A, Kürnsteiner P, Raabe D, Jägle EA. Steels in additive manufacturing: A review of their microstructure and properties. Materials Science and Engineering: A. 2020 jan;772(October 2019):138633.

[60] Gorsse S, Hutchinson C, Gouné M, Banerjee R. Additive manufacturing of metals: a brief review of the characteristic microstructures and properties of steels, Ti-6Al-4V and high-entropy alloys. Science and Technology of Advanced Materials. 2017;18(1):584–610.

[61] Shamsujjoha M, Agnew SR, Fitz-Gerald JM, Moore WR, Newman TA. High Strength and Ductility of Additively Manufactured 316L Stainless Steel Explained. Metallurgical and Materials Transactions A: Physical Metallurgy and Materials Science. 2018;49(7):3011–3027.

[62] Ghouse S, Babu S, Van Arkel RJ, Nai K, Hooper PA, Jeffers JRT. The influence of laser parameters and scanning strategies on the mechanical properties of a stochastic porous material. Materials & Design. 2017 oct;131(June):498–508.

[63] Calignano F. Design optimization of supports for overhanging structures in aluminum and titanium alloys by selective laser melting. Materials and Design. 2014;64:203–213.

[64] Hocheng H, Kao PS, Chen YF. Electropolishing of 316L stainless steel for anticorrosion passivation. Journal of Materials Engineering and Performance. 2001;10(4):414–418.

[65] Waqar S, Liu J, Sun Q, Guo K, Sun J. Effect of post-heat treatment cooling on microstructure and mechanical properties of selective laser melting manufactured austenitic 316L stainless steel. Rapid Prototyping Journal. 2020 sep;ahead-of-p(ahead-of-print).

[66] Cui L, Jiang S, Xu J, Peng RL, Mousavian RT, Moverare J. Revealing relationships between microstructure and hardening nature of additively manufactured 316L stainless steel. Materials and Design. 2021;198(December):109385.

[67] Yasa E, Kruth JP. Microstructural investigation of Selective Laser Melting 316L stainless steel parts exposed to laser re-melting. Procedia Engineering. 2011;19:389–395.

[68] Suryawanshi J, Prashanth KG, Ramamurty U. Mechanical behavior of selective laser melted 316L stainless steel. Materials Science and Engineering: A. 2017 jun;696:113–121.

[69] Zhong Y, Liu L, Wikman S, Cui D, Shen Z. Intragranular cellular segregation network structure strengthening 316L stainless steel prepared by selective laser melting. Journal of Nuclear Materials. 2016 mar;470:170–178.

[70] Kurzynowski T, Gruber K, Stopyra W, Kuźnicka B, Chlebus E. Correlation between process parameters, microstructure and properties of 316 L stainless steel processed by selective laser melting. Materials Science and Engineering A. 2018 mar;718(January):64–73.

[71] DebRoy T, Wei HL, Zuback JS, Mukherjee T, Elmer JW, Milewski JO, et al. Additive manufacturing of metallic components – Process, structure and properties. Progress in Materials Science. 2018;92:112–224.

[72] Sames WJ, List FA, Pannala S, Dehoff RR, Babu SS. The metallurgy and processing science of metal additive manufacturing. International Materials Reviews. 2016;61(5):315–360.

[73] Hitzler L, Hirsch J, Heine B, Merkel M, Hall W, Öchsner A. On the anisotropic mechanical properties of selective laser-melted stainless steel. Materials. 2017;10(10).

[74] Tolosa I, Garciandía F, Zubiri F, Zapirain F, Esnaola A. Study of mechanical properties of AISI 316 stainless steel processed by "selective laser melting", following different manufacturing strategies. The International Journal of Advanced Manufacturing Technology. 2010 nov;51(5-8):639–647.

[75] Nandishwarsteel. ASME SA 240 Stainless Steel 316/ 316L sheets and plates; 2010. Available from: `https://www.nandishwarsteel.com/stainless-steel-316-316l-sheets-plates.html`.

[76] Wang YM, Voisin T, McKeown JT, Ye J, Calta NP, Li Z, et al. Additively manufactured hierarchical stainless steels with high strength and ductility. Nature Materials. 2018 jan;17(1):63–71.

[77] Simson T, Emmel A, Dwars A, Böhm J. Residual stress measurements on AISI 316L samples manufactured by selective laser melting. Additive Manufacturing. 2017;17:183–189.

[78] Casati R, Lemke J, Vedani M. Microstructure and Fracture Behavior of 316L Austenitic Stainless Steel Produced by Selective Laser Melting. Journal of Materials Science & Technology. 2016 aug;32(8):738–744.

[79] Riemer A, Leuders S, Thöne M, Richard HA, Tröster T, Niendorf T. On the fatigue crack growth behavior in 316L stainless steel manufactured by selective laser melting. Engineering Fracture Mechanics. 2014 apr;120:15–25.

[80] Chen W, Voisin T, Zhang Y, Florien JB, Spadaccini CM, McDowell DL, et al. Microscale residual stresses in additively manufactured stainless steel. Nature Communications. 2019 dec;10(1):4338.

[81] Salman OO, Gammer C, Chaubey AK, Eckert J, Scudino S. Effect of heat treatment on microstructure and mechanical properties of 316L steel synthesized by selective laser melting. Materials Science and Engineering: A. 2019 mar;748(October 2018):205–212.

[82] Shiomi M, Osakada K, Nakamura K, Yamashita T, Abe F. Residual Stress within Metallic Model Made by Selective Laser Melting Process. CIRP Annals. 2004;53(1):195–198.

[83] Ronneberg T, Davies CM, Hooper PA. Revealing relationships between porosity, microstructure and mechanical properties of laser powder bed fusion 316L stainless steel through heat treatment. Materials and Design. 2020;189:108481.

[84] Moura LS, Vittoria GD, Gabriel AHG, Fonseca EB, Gabriel LP, Webster TJ, et al. A highly accurate methodology for the prediction and correlation of mechanical properties based on the slimness ratio of additively manufactured tensile test specimens. Journal of Materials Science. 2020;55(22):9578–9596.

[85] Suard M, Martin G, Lhuissier P, Dendievel R, Vignat F, Blandin JJ, et al. Mechanical equivalent diameter of single struts for the stiffness prediction of lattice structures produced by Electron Beam Melting. Additive Manufacturing. 2015 oct;8:124–131.

[86] Strano G, Hao L, Everson RM, Evans KE. Surface roughness analysis, modelling and prediction in selective laser melting. Journal of Materials Processing Technology. 2013 apr;213(4):589–597.

[87] Charles A, Elkaseer A, Thijs L, Hagenmeyer V, Scholz S. Effect of process parameters on the generated surface roughness of down-facing surfaces in selective laser melting. Applied Sciences (Switzerland). 2019;9(6):1–13.

[88] Suard M, Barrière L, Lhuissier P, Perusin S, Filloux B, Dendievel R. Influence of manufacturing orientations on the morphology of alloy 718 single struts manufactured by selective laser melting. Material Design & Processing Communications. 2020 jan;(January):mdp2.140.

[89] Van Bael S, Kerckhofs G, Moesen M, Pyka G, Schrooten J, Kruth JP. Micro-CT-based improvement of geometrical and mechanical controllability of selective laser melted Ti6Al4V porous structures. Materials Science and Engineering: A. 2011 sep;528(24):7423–7431.

[90] Wei L, Leo HL, Chen Q, Li Z. Structural and Hemodynamic Analyses of Different Stent Structures in Curved and Stenotic Coronary Artery. Frontiers in Bioengineering and Biotechnology. 2019;7(December):1–13.

[91] Dumoulin C, Cochelin B. Mechanical behaviour modelling of balloon-expandable stents. Journal of Biomechanics. 2000;33(11):1461–1470.

[92] Morlacchi S, Keller B, Arcangeli P, Balzan M, Migliavacca F, Dubini G, et al. Hemodynamics and In-stent restenosis: Micro-CT images, histology, and computer simulations. Annals of Biomedical Engineering. 2011;39(10):2615–2626.

[93] Balossino R, Gervaso F, Migliavacca F, Dubini G. Effects of different stent designs on local hemodynamics in stented arteries. Journal of Biomechanics. 2008;41(5):1053–1061.

[94] Lee W, Cho SW, Allahwala UK, Bhindi R. Numerical study to identify the effect of fluid presence on the mechanical behavior of the stents during coronary stent expansion. Computer Methods in Biomechanics and Biomedical Engineering. 2020;23(11):744–754.

[95] Chiastra C, Migliavacca F, Martínez MÁ, Malvè M. On the necessity of modelling fluid-structure interaction for stented coronary arteries. Journal of the Mechanical Behavior of Biomedical Materials. 2014;34:217–230.

[96] Morlacchi S, Chiastra C, Gastaldi D, Pennati G, Dubini G, Migliavacca F. Sequential structural and fluid dynamic numerical simulations of a stented bifurcated coronary artery. Journal of biomechanical engineering. 2011;133(12):121010.

[97] Grogan JA, Leen SB, McHugh PE. Comparing coronary stent material performance on a common geometric platform through simulated bench testing. Journal of the mechanical behavior of biomedical materials. 2012;12:129–138.

[98] Petrini L, Migliavacca F, Auricchio F, Dubini G. Numerical investigation of the intravascular coronary stent flexibility. Journal of Biomechanics. 2004;37(4):495–501.

[99] Azaouzi M, Makradi A, Belouettar S. Numerical investigations of the structural behavior of a balloon expandable stent design using finite element method. Computational Materials Science. 2013 may;72:54–61.

[100] Cabrera MS, Oomens CWJJ, Baaijens FPTT. Understanding the requirements of self-expandable stents for heart valve replacement: Radial force, hoop force and equilibrium. Journal of the mechanical behavior of biomedical materials. 2017;68(October 2016):252–264.

[101] Liu Y, Zhang P. Characterization of compression behaviors of fully covered biodegradable polydioxanone biliary stent for human body: A numerical approach by finite element model. Journal of the mechanical behavior of biomedical materials. 2016;62(2999):128–138.

[102] Gervaso F, Capelli C, Petrini L, Lattanzio S, Di Virgilio L, Migliavacca F. On the effects of different strategies in modelling balloon-expandable stenting by means of finite element method. Journal of Biomechanics. 2008;41(6):1206–1212.

[103] Lally C, Dolan F, Prendergast PJ. Cardiovascular stent design and vessel stresses: A finite element analysis. Journal of Biomechanics. 2005;38(8):1574–1581.

[104] Gijsen FJH, Migliavacca F, Schievano S, Socci L, Petrini L, Thury A, et al. Simulation of stent deployment in a realistic human coronary artery. BioMedical Engineering Online. 2008;7:1–11.

[105] Chen C, Xiong Y, Jiang W, Wang Y, Wang Z, Chen Y. Experimental and Numerical Simulation of Biodegradable Stents with Different Strut Geometries. Cardiovascular Engineering and Technology. 2020;11(1):36–46.

[106] Blair RW, Dunne NJ, Lennon AB, Menary GH. Multi-objective optimisation of material properties and strut geometry for poly(L-lactic acid) coronary stents using response surface methodology. PLoS ONE. 2019;14(8):1–21.

[107] Geith MA, Swidergal K, Hochholdinger B, Schratzenstaller TG, Wagner M, Holzapfel GA. On the importance of modeling balloon folding, pleating, and stent crimping: An FE study comparing experimental inflation tests. International Journal for Numerical Methods in Biomedical Engineering. 2019;35(11):1–19.

[108] McGarry JP, O'Donnell BP, McHugh PE, McGarry JG. Analysis of the mechanical performance of a cardiovascular stent design based on micromechanical modelling. Computational Materials Science. 2004;31(3-4):421–438.

[109] Grogan JA, Leen SB, McHugh PE. Influence of statistical size effects on the plastic deformation of coronary stents. Journal of the Mechanical Behavior of Biomedical Materials. 2013;20:61–76.

[110] Auricchio F, Di Loretto M, Sacco E. Finite-element Analysis of a Stenotic Artery Revascularization Through a Stent Insertion. Computer methods in biomechanics and biomedical engineering. 2001;4(3):249–263.

[111] Debusschere N, Segers P, Dubruel P, Verhegghe B, De Beule M. A finite element strategy to investigate the free expansion behaviour of a biodegradable polymeric stent. Journal of Biomechanics. 2015;48(10):2012–2018.

[112] Kiousis DE, Wulff AR, Holzapfel GA. Experimental studies and numerical analysis of the inflation and interaction of vascular balloon catheter-stent systems. Annals of Biomedical Engineering. 2009;37(2):315–330.

[113] Chua SND, MacDonald BJ, Hashmi MSJ. Finite element simulation of slotted tube (stent) with the presence of plaque and artery by balloon expansion. Journal of Materials Processing Technology. 2004;155-156(1-3):1772–1779.

[114] Wang WQ, Liang DK, Yang DZ, Qi M. Analysis of the transient expansion behavior and design optimization of coronary stents by finite element method. Journal of Biomechanics. 2006;39(1):21–32.

[115] Prendergast PJ, Lally C, Daly S, Reid AJ, Lee TC, Quinn D, et al. Analysis of Prolapse in Cardiovascular Stents: A Constitutive Equation for Vascular Tissue and Finite-Element Modelling. Journal of Biomechanical Engineering. 2003;125(5):692–699.

[116] Zahedmanesh H, Lally C. Determination of the influence of stent strut thickness using the finite element method: Implications for vascular injury and in-stent restenosis. Medical & biological engineering & computing. 2009;47(4):385–393.

[117] Holzapfel GA, Sommer G, Gasser CT, Regitnig P. Determination of layer-specific mechanical properties of human coronary arteries with nonatherosclerotic intimal thickening and related constitutive modeling. American Journal of Physiology - Heart and Circulatory Physiology. 2005;289(5 58-5):2048–2058.

[118] Langdon GS, Schleyer GK. Unusual strain rate sensitive behaviour of AISI 316L austenitic stainless steel. The Journal of Strain Analysis for Engineering Design. 2004;39(1):71–86.

[119] Shen Y, Mckown S, Tsopanos S, Sutcliffe CJ, Mines RAW, Cantwell WJ. The Mechanical Properties of Sandwich Structures Based on Metal Lattice Architectures. Journal of Sandwich Structures & Materials. 2010 mar;12(2):159–180.

[120] Gümrük R, Mines RAW. Compressive behaviour of stainless steel micro-lattice structures. International Journal of Mechanical Sciences. 2013 mar;68:125–139.

[121] Leicht A, Klement U, Hryha E. Effect of build geometry on the microstructural development of 316L parts produced by additive manufacturing. Materials Characterization. 2018 sep;143(2017):137–143.

[122] Redwood B, Petrak M, Alan R, Ryan O, Jared K. How to design parts for metal 3D printing; 2021. Available from: `https://www.3dhubs.com/knowledge-base/how-design-parts-metal-3d-printing/`.

[123] Wiesent L, Schultheiß U, Lulla P, Nonn A, Noster U, Noster U, et al. Mechanical properties of small structures built by selective laser melting 316L stainless steel– a phenomenological approach to improve component design. Materialwissenschaft und Werkstofftechnik. 2020;51(12):1615–1629.

[124] Deutsches Intitute für Normung e V . DIN 50125:2016-12 , Prüfung metallischer Werkstoffe - Zugproben. Beuth Verlag; 2016.

[125] Ocylok S, Alexeev E, Mann S, Weisheit A, Wissenbach K, Kelbassa I. Correlations of melt pool geometry and process parameters during laser metal deposition by coaxial process monitoring. Physics Procedia. 2014;56(C):228–238.

[126] Rosenthal D. The Theory of Moving Source of Heat and its Application to Metal Transfer. vol. 43. ASME; 1946.

[127] Tang M, Pistorius PC, Beuth JL. Prediction of lack-of-fusion porosity for powder bed fusion. Additive Manufacturing. 2017;14:39–48.

[128] Barba D, Alabort C, Tang YT, Viscasillas MJ, Reed RC, Alabort E. On the size and orientation effect in additive manufactured Ti-6Al-4V. Materials & Design. 2020;186:108235.

[129] Leicht A, Rashidi M, Klement U, Hryha E. Effect of process parameters on the microstructure, tensile strength and productivity of 316L parts produced by laser powder bed fusion. Materials Characterization. 2021;159(February):100037.

[130] Khairallah SA, Anderson AT, Rubenchik A, King WE. Laser powder-bed fusion additive manufacturing: Physics of complex melt flow and formation mechanisms of pores, spatter, and denudation zones. Acta Materialia. 2016 apr;108:36–45.

[131] Frazier WE. Metal Additive Manufacturing: A Review. Journal of Materials Engineering and Performance. 2014 jun;23(6):1917–1928.

[132] Koutiri I, Pessard E, Peyre P, Amlou O, De Terris T. Influence of SLM process parameters on the surface finish, porosity rate and fatigue behavior of as-built Inconel 625 parts. Journal of Materials Processing Technology. 2018 may;255:536–546.

[133] Kamath C, El-dasher B, Gallegos GF, King WE, Sisto A. Density of additively-manufactured, 316L SS parts using laser powder-bed fusion at powers up to 400 W. The International Journal of Advanced Manufacturing Technology. 2014 sep;74(1-4):65–78.

[134] Reinhart G, Teufelhart S, Riss F. Examination of the Geometry-dependent Anisotropic Material Behavior in Additive Layer Manufacturing for the Calculation of Mesoscopic Lightweight Structures. In: Fraunhofer Direct Digital Manufacturing Conference DDMC. Berlin: Fraunhofer Additive Manufacturing Alliance; 2012. .

[135] Starzyński G, Gambin W. Natural surface layer of metals. Acta Physica Polonica A. 1996;89(3):377–381.

[136] Niendorf T, Leuders S, Riemer A, Richard HA, Tröster T, Schwarze D. Highly Anisotropic Steel Processed by Selective Laser Melting. Metallurgical and Materials Transactions B. 2013 aug;44(4):794–796.

[137] Nagarajan B, Hu Z, Song X, Zhai W, Wei J. Development of Micro Selective Laser Melting: The State of the Art and Future Perspectives. Engineering. 2019;5(4):702–720.

[138] Zhao H, van Humbeeck J, Sohier J, de Scheerder I, Humbeeck JV, Sohier J, et al. Electrochemical polishing of 316L stainless steel slotted tube coronary stents. Journal of Materials Science: Materials in Medicine. 2002;13(10):911–916.

[139] Wiesent L, Schultheiß U, Lulla P, Noster U, Schratzenstaller T, Schmid C, et al. Computational analysis of the effects of geometric irregularities and post-processing steps on the mechanical behavior of additively manufactured 316L stainless steel stents. PLOS ONE. 2020 dec;15(12):e0244463.

[140] Deutsches Intitute für Normung e V . DIN EN ISO 25539-2:2013-05,Kardiovaskuläre Implantate - Endovaskuläre Implantate - Teil 2: Gefäßstents (ISO 25539-2:2012); Deutsche Fassung EN ISO 25539-2:2012. Beuth Verlag; 2013.

[141] Matheson KE, Cross KK, Nowell MM, Spear AD. A multiscale comparison of stochastic open-cell aluminum foam produced via conventional and additive-manufacturing routes. Materials Science and Engineering A. 2017;707:181–192.

[142] Qiu C, Yue S, Adkins NJE, Ward M, Hassanin H, Lee PD, et al. Influence of processing conditions on strut structure and compressive properties of cellular lattice structures fabricated by selective laser melting. Materials Science and Engineering: A. 2015 mar;628:188–197.

[143] Solberg K, Guan S, Razavi SMJ, Welo T, Chan KC, Berto F. Fatigue of additively manufactured 316L stainless steel: The influence of porosity and surface roughness. Fatigue and Fracture of Engineering Materials and Structures. 2019;42(9):2043–2052.

[144] Banhart J, Baumeister J, Bahart J, Baumester J. Deformation characteristics of metal foams. Journal of Materials Science. 1998;33(6):1431–1440.

[145] Bae IHH, Lim KSS, Park JCJKKJCJK, Park DSS, Lee SYY, Jang EJJ, et al. Mechanical behavior and in vivo properties of newly designed bare metal stent for enhanced flexibility. Journal of Industrial and Engineering Chemistry. 2015 jan;21:1295–1300.

[146] Polishetty A, Littlefair G. Heat Treatment Effect on the Fatigue Characteristics of Additive Manufactured Stainless Steel 316L. International Journal of Materials, Mechanics and Manufacturing. 2019 apr;7(2):114–118.

[147] Tsopanos S, Mines RAW, McKown S, Shen Y, Cantwell WJ, Brooks W, et al. The influence of processing parameters on the mechanical properties of selectively laser melted stainless steel microlattice structures. Journal of Manufacturing Science and Engineering, Transactions of the ASME. 2010;132(4):0410111–04101112.

[148] Sarkar S, Kumar CS, Nath AK. Effects of different surface modifications on the fatigue life of selective laser melted 15–5 PH stainless steel. Materials Science and Engineering: A. 2019 aug;762(June):138109.

[149] Gümrük R, Mines RAWW, Karadeniz S. Determination of Strain Rate Sensitivity of Micro-struts Manufactured Using the Selective Laser Melting Method. Journal of Materials Engineering and Performance. 2018 mar;27(3):1016–1032.

[150] du Plessis A, Yadroitsev I, Yadroitsava I, Le Roux SG. X-Ray Microcomputed Tomography in Additive Manufacturing: A Review of the Current Technology and Applications. 3D Printing and Additive Manufacturing. 2018 sep;5(3):227–247.

[151] Ushijima K, Cantwell W, Mines R, Tsopanos S, Smith M. An investigation into the compressive properties of stainless steel micro-lattice structures. Journal of Sandwich Structures & Materials. 2011 may;13(3):303–329.

[152] Smith M, Guan Z, Cantwell WJ. Finite element modelling of the compressive response of lattice structures manufactured using the selective laser melting technique. International Journal of Mechanical Sciences. 2013;67:28–41.

[153] Spierings AB, Herres N, Levy G. Influence of the particle size distribution on surface quality and mechanical properties in AM steel parts. Rapid Prototyping Journal. 2011;17(3):195–202.

[154] Tan JH, Wong WLE, Dalgarno KW. An overview of powder granulometry on feedstock and part performance in the selective laser melting process. Additive Manufacturing. 2017;18:228–255.

[155] Pyka G, Burakowski A, Kerckhofs G, Moesen M, Van Bael S, Schrooten J, et al. Surface modification of Ti6Al4V open porous structures produced by additive manufacturing. Advanced Engineering Materials. 2012;14(6):363–370.

[156] De Wild M, Schumacher R, Mayer K, Schkommodau E, Thoma D, Bredell M, et al. Bone regeneration by the osteoconductivity of porous titanium implants manufactured by selective laser melting: A histological and micro computed tomography study in the rabbit. Tissue Engineering - Part A. 2013;19(23-24):2645–2654.

[157] Guo H, Takezawa A, Honda M, Kawamura C, Kitamura M. Finite element simulation of the compressive response of additively manufactured lattice structures with large diameters. Computational Materials Science. 2020;175(December 2019):109610.

[158] Ravari MRK, Esfahani SN, Andani MT, Kadkhodaei M, Ghaei A, Karaca H, et al. On the effects of geometry, defects, and material asymmetry on the mechanical response of shape memory alloy cellular lattice structures. Smart Materials and Structures. 2016 feb;25(2):025008.

[159] Lozanovski B, Leary M, Tran P, Shidid D, Qian M, Choong P, et al. Computational modelling of strut defects in SLM manufactured lattice structures. Materials and Design. 2019;171:107671.

[160] Kleemola HJ, Nieminen MA. On the strain-hardening parameters of metals. Metallurgical Transactions. 1974 aug;5(8):1863–1866.

[161] Zhao D, Matheson KE, Phung BR, Petruzza S, Czabaj MW, Spear AD. Investigating the effect of grain structure on compressive response of open-cell metal foam using high-fidelity crystal-plasticity modeling. Materials Science and Engineering: A. 2021 apr;812:140847.

[162] Sweeney CA, McHugh PE, McGarry JP, Leen SB. Micromechanical methodology for fatigue in cardiovascular stents. International Journal of Fatigue. 2012;44:202–216.

[163] Lapp H. Das Herzkatheterbuch. Stuttgart: Georg Thieme Verlag; 2019.

[164] Alomar Z, Concli F. A Review of the Selective Laser Melting Lattice Structures and Their Numerical Models. Advanced Engineering Materials. 2020 dec;22(12):2000611.

[165] Li P, Warner DH, Fatemi A, Phan N. Critical assessment of the fatigue performance of additively manufactured Ti-6Al-4V and perspective for future research. International Journal of Fatigue. 2016;85:130–143.

[166] Yadollahi A, Shamsaei N, Thompson SM, Elwany A, Bian L. Effects of building orientation and heat treatment on fatigue behavior of selective laser melted 17-4 PH stainless steel. International Journal of Fatigue. 2017;94:218–235.

[167] Wycisk E, Solbach A, Siddique S, Herzog D, Walther F, Emmelmann C. Effects of defects in laser additive manufactured Ti-6Al-4V on fatigue properties. Physics Procedia. 2014;56(C):371–378.

[168] Yadollahi A, Shamsaei N. Additive manufacturing of fatigue resistant materials: Challenges and opportunities. International Journal of Fatigue. 2017;98:14–31.

[169] Kong D, Ni X, Dong C, Lei X, Zhang L, Man C, et al. Bio-functional and anti-corrosive 3D printing 316L stainless steel fabricated by selective laser melting. Materials and Design. 2018;152(2017):88–101.

[170] Al-Mamun NS, Mairaj Deen K, Haider W, Asselin E, Shabib I. Corrosion behavior and biocompatibility of additively manufactured 316L stainless steel in a physiological environment: the effect of citrate ions. Additive Manufacturing. 2020;34(April):101237.

[171] Sander G, Thomas S, Cruz V, Jurg M, Birbilis N, Gao X, et al. On The Corrosion and Metastable Pitting Characteristics of 316L Stainless Steel Produced by Selective Laser Melting. Journal of The Electrochemical Society. 2017;164(6):C250–C257.

[172] Chao Q, Cruz V, Thomas S, Birbilis N, Collins P, Taylor A, et al. On the enhanced corrosion resistance of a selective laser melted austenitic stainless steel. Scripta Materialia. 2017;141:94–98.

Acknowledgement

At this point, I would like to express my sincere thanks to all those who accompanied me during my doctoral studies, supported me and thus made the completion of this doctorate possible.

Many thanks to my supervisor, Prof. Dr.-Ing. Aida Nonn, for providing me with my PhD topic, for her professional guidance and for her always motivating words during my work as a member of the CMMLab. Thank you for always supporting and encouraging me to pursue my goals and for opening new opportunities for me, such as a research stay at the University of Utah.

My further thanks go to my first mentor Prof. Dr. med. Schmid for the opportunity to conduct my doctoral studies at the University of Regensburg. Thank you very much for the friendly way of communication and the patient explanations of medical knowledge. To Prof. Dr. rer. nat. Karla Lehle I want to express my sincere thanks for accepting the second mentorship, as well as your constructive professional advice during my colloquia, and the insights into experimental cardiothoracic surgery.

I would like to express my sincere thanks to Prof. Dr.-Ing. Thomas Schratzenstaller for encouraging me to do this PhD and for making its initial phase possible. Many thanks for providing the expertise on coronary stents and for providing the experimental data basis for the validation of the simulations of conventionally manufactured stents. Another thanks goes to Prof. Dr.-Ing. Ulf Noster for the opportunity to participate in the New-GenStent research project, the constructive cooperation and the opportunity to gain practical experimental experience in his lab.

A special thanks also goes to Prof. Dr. Ashley Spear for inviting me to a research visit at the University of Utah, which had a great impact on me both professionally and personally. Thank you for encouraging me to think outside the box, for sharing your enthusiasm for research, and for actively supporting me in the publication process. In this context, I would also like to thank the German-American Fulbright Commission, which made the research stay in America possible by providing a scholarship.

Many thanks to the Landeskonferenz der Frauen- und Gleichstellungsbeauftragten an bayerischen Hochschulen (LaKoF Bayern) for providing me with a doctoral scholarship and the numerous

networking meetings, which always gave me new motivation for my doctorate. As a representative of this, I would like to especially thank Prof. Dr. Christine Süß-Gebhard and Sabine Hoffmann for their support and friendly advice.

Many thanks also to the BayWISS-Verbundkolleg "Gesundheit" for the financial and non-material support of my PhD project, which enabled part of my research, the participation in training/conferences and the publication of research results.

A special thanks goes to the people who influenced my daily work the most and who contributed in one way or another to the success of this dissertation. Many thanks to Ulrich Schultheiß, Philipp Marx, Philipp Lulla, Moritz Burger, Vincent Keim and Marius Grad. You guys really created a great working atmosphere for me and always actively supported me. Many thanks for that!

I would also like to thank my family and friends who have motivated me to overcome all hurdles and supported me over the past years. I would especially like to thank my parents and my siblings Stefan and Carina for their family support, valuable advice, for believing in me and taking me as I am. Finally, I would like to thank Sebastian Gärtner for accompanying me through all the ups and downs of this PhD and always standing by my side.

Lisa Wiesent
Regensburg,October 19, 2022